CORA Cork Open Research Archive
Cartlann Taighde Oscailte Chorcaí

Title	Block copolymer self-assembly: ordered film formation and defect analysis
Authors	Collins, Timothy W.
Publication date	2017
Original Citation	Collins, T. W. 2017. Block copolymer self-assembly: ordered film formation and defect analysis. PhD Thesis, University College Cork.
Type of publication	Doctoral thesis
Rights	© 2017, Timothy William Collins. - http://creativecommons.org/licenses/by-nc-nd/3.0/
Download date	2026-11-16 07:48:38
Item downloaded from	https://hdl.handle.net/10468/5564



UCC
University College Cork, Ireland
Coláiste na hOllscoile Corcaigh

Block Copolymer Self-assembly: Ordered Film Formation and Defect Analysis

Timothy William Collins, BSc. (Hons)

School of Chemistry,
University College Cork,
Ireland.



ucc
Coláiste na hOllscoile Corcaigh, Éire
University College Cork, Ireland

Presented for the PhD. Degree to the National University of Ireland

Supervisor: Prof. Michael A. Morris

Head of Department: Prof. Justin D. Holmes

Declaration

I, Timothy William Collins, certify that this thesis is my own research and I have not obtained a degree in University College Cork or elsewhere on the basis of this PhD Thesis.

_____

Timothy William Collins

Abstract

The self-assembly of block copolymers (BCPs) is a promising strategy for the creation of nanoscale structures for use in a wide range of applications. In particular, as conventional photolithographic methods of fabricating nanoelectronics approach their physical limitations, BCPs offer a route to continue scaling down feature size. This thesis investigated the ability of BCPs in thin film to form well-ordered patterns in the nanometre range using a series of polystyrene-*block*-poly(ethylene oxide) (PS-*b*-PEO), polystyrene-*block*-poly(methyl methacrylate) (PS-*b*-PMMA) and polystyrene-*block*-poly(2-vinylpyridine) (PS-*b*-P2VP) for lithographic applications. A novel application for the analysis of BCP patterns is detailed, as a tool for the further optimisation of microphase separation techniques.

Chapter 1 introduces the driving motivation for the research carried out in this PhD. The nanoelectronics industry is facing a significant challenge in future development, and outlined are the properties which have led to BCPs emerging as a major competitor to next-generation lithography. The fundamental characteristics of block copolymer self-assembly are explained and techniques for improving long range order are discussed.

Chapter 2 focuses on the microphase separation within PS-*b*-PEO. The kinetics of the pattern evolution are investigated, and details a cyclical-flipping phenomenon observed in the pattern orientation. Using solvent annealing, patterns exhibiting excellent long-range order are achieved using directing effects imposed through the confinement of the film within topographical channels. Variation of anneal time and solvent atmosphere provides a means to control the cylinder orientation.

The microphase separation of lamellar PS-*b*-PEO is discussed in Chapter 3. Perpendicular orientation was obtained through a combined thermal-solvent annealing process, without the requirement of a neutral brush layer or additional surface modification. Wet (acid) and dry (plasma) etch methods were explored and pattern transfer into the underlying silicon substrate with the creation of sub-20 nm nanowires was observed.

An application developed for the analysis of BCP patterns imaged via scanning electron microscope (SEM) and atomic force microscope (AFM) is described in Chapter 4. It is shown that it can determine key metrics for BCP pattern optimisation including the degree of non-uniformity, the order, the defect density and the line roughness, including an estimate of line edge roughness (LER). PS-b-PMMA patterns are used as a demonstration of the analysis tool.

Chapter 5 details the use of a large molecular weight BCP, PS-b-P2VP in the creation of well-ordered silicon nanopillars (SiNPs) in the 100 nm range for use in optical applications. Detailed metrology and 3D visualisation was performed on the perforated lamellar structure of the BCP. Reflectivity of the functionalised surfaces is discussed.

Chapter 6 provides a general overview of the conclusion of each chapter and an outlook to the future of the field.

Acknowledgements

First off, I would like to thank my supervisor Prof. Michael A. Morris for giving me the opportunity to undertake this PhD research in his laboratory and I appreciate all the help and advice he has given me throughout. I would also like to thank Prof. Justin Holmes for his help and support. I am also thankful to Science Foundation Ireland for giving me the funding for this opportunity.

I would also like to thank the postdoctoral researchers Parvaneh, Tandra, Sibu, Atul, Cian, Sankar, Dipu, Colm, Barbara and Ben for their insight and tireless encouragement. Their assistance and guidance was invaluable. I also thank Colm Coughlan, whose insight into Matlab was indispensable. I sincerely thank my student colleagues, John, Shelly, David, Elsa, Niall and Raj for making my time in 343 a time I will always cherish.

I also express my gratitude to all the staff of the School of Chemistry for their assistance.

Finally, I would like to thank my family especially my parents, Tadhg and Margaret, and my sister, who have been incredibly supportive of all my decisions throughout my time in UCC. They were always interested in what I was doing and how I was getting on. I cannot thank them enough for everything.

Published Articles

[1] P. Mokarian-Tabari, T. W. Collins, J. D. Holmes, and M. A. Morris, "Cyclical 'Flipping' of Morphology in Block Copolymer Thin Films," *ACS Nano*, vol. 5, no. 6, pp. 4617–4623, Jun. 2011.

[2] P. Mokarian-Tabari, T. W. Collins, J. D. Holmes, and M. A. Morris, "Brushless and controlled microphase separation of lamellar polystyrene-b-polyethylene oxide thin films for block copolymer nanolithography," *J. Polym. Sci. Part B Polym. Phys.*, vol. 50, no. 13, pp. 904–909, Jul. 2012.

[3] P. Mokarian-Tabari, R. Senthamaraikannan, C. Glynn, T. W. Collins, C. Cummins, D. Nugent, C. O'Dwyer, and M. A. Morris, "Large Block Copolymer Self-Assembly for Fabrication of Subwavelength Nanostructures for Applications in Optics," *Nano Lett.*, vol. 17, no. 5, pp. 2973–2978, May 2017.

[4] H. Erothu, J. Kolomanska, P. Johnston, S. Schumann, D. Deribew, D. T. W. Toolan, A. Gregori, C. Dagron-Lartigau, G. Portale, W. Bras, T. Arnold, A. Distler, R. C. Hiorns, P. Mokarian-Tabari, T. W. Collins, J. R. Howse, and P. D. Topham, "Synthesis, Thermal Processing, and Thin Film Morphology of Poly(3-hexylthiophene)–Poly(styrenesulfonate) Block Copolymers," *Macromolecules*, vol. 48, no. 7, pp. 2107–2117, Apr. 2015.

[5] C. Glynn, D. Creedon, H. Geaney, E. Armstrong, T. Collins, M. a Morris, and C. O. Dwyer, "Linking Precursor Alterations to Nanoscale Structure and Optical Transparency in Polymer Assisted Fast-Rate Dip-Coating of Vanadium Oxide Thin Films," *Sci. Rep.*, vol. 5, no. April, p. 11574, Jun. 2015.

[6] M. Conroy, H. Li, V. Z. Zubialevich, G. Kusch, M. Schmidt, T. Collins, C. Glynn, R. W. Martin, C. O'Dwyer, M. D. Morris, J. D. Holmes, and P. J. Parbrook, "Self-Healing Thermal Annealing: Surface Morphological Restructuring Control of GaN Nanorods," *Cryst. Growth Des.*, vol. 16, no. 12, pp. 6769–6775, Dec. 2016.

[7] C. Cummins, T. W. Collins, R. A. Kelly, E. K. McCarthy, and M. A. Morris, "In-depth TEM characterization of block copolymer pattern transfer at germanium surfaces," *Nanotechnology*, vol. 27, no. 48, p. 484003, Dec. 2016.

Submitted Articles

[1] D. Sullivan, M. Cruz-Romero, **T. Collins**, E. Cummins, J. Kerry, and M. Morris, "Development of size controlled chitosan nanoparticles and their activity for potential use in antimicrobial food packaging applications,"

[2] R. Banta, **T. Collins**, P. Young, J. Holmes, and E. Flynn, "Nanopatterned Protein-Polysaccharide Thin Films by Humidity Regulated Phase Separation,"

Articles in preparation

[1] **T. Collins**, C. Coughlan, J. Holmes, and M. Morris, "Dimensional and Defectivity Data Analysis for Block Copolymer Thin Film Metrology,"

Conferences

[1] **T. Collins**, B. Kosmala, C. Keating, R. Senthamaraikannan, J. D. Holmes, and M. A. Morris, "Modelling Block Copolymer 3D Structures via Multiple Characterization Methods," Poster presentation at the *2nd DSA Symposium*, Grenoble, France, October 11-13, 2016

[2] B. Kosmala, **T. Collins**, C. Keating, R. Senthamaraikannan, R. Tiron, C. Navarro, I. Cayrefourcq, and M. A. Morris, "Influence of polymer properties on pattern characteristics of PS-*b*-PMMA films," Poster presentation at the *2nd DSA Symposium*, Grenoble, France, October 11-13, 2016

[3] P. Mokarian-Tabari, R. Senthamaraikannan, **T. W. Collins**, C. Glynn, C. O'Dwyer, and M. Morris, "Nanopatterning by large block copolymers for application in photonic devices," Oral presentation at the *Society of Photographic Instrumentation Engineers Conf., Photonic Crystal Materials and Devices XII*, Brussels, Belgium, April 4-7, 2016

[4] P. Mokarian-Tabari, **T. W. Collins**, and M. A. Morris, "The kinetics of swelling in block copolymer thin films during "solvo-microwave" and solvo-thermal annealing: The effect of vapour pressure rate," Poster presentation at the *Institute of Physics, Physical Aspects of Polymer Science Conf.*, Manchester, UK, September 8-10, 2015

[5] P. Mokarian-Tabari, **T. Collins**, C. Cummins, C. Simão, C. Sotomayor Torres, and M. A. Morris, "The kinetics of swelling in block copolymer thin films during "solvo-microwave" and solvo-thermal annealing: The effect of vapour pressure," Oral presentation at the *European Materials Research Society Spring Meeting*, Lille, France, May 11-15, 2015

[6] P. Mokarian-Tabari, **T. Collins**, C. Cummins, C. D. Simão, C. Sotomayor Torres, and M. A. Morris, "The kinetics of swelling in block copolymer thin films during "solvo-microwave" and solvo-thermal annealing: The effect of vapour pressure," Oral and Poster presentation at the *American Physical Society March Meeting*, San Antonio, TX, March 2-6, 2015

[7] P. Mokarian-Tabari, C. Cummins, **T. Collins**, S. Rasappa, and M. A. Morris, "An In-Situ Study of Kinetics of Rapid Self- Assembly in Block Copolymer Thin Films During "Solve-Microwave" Annealing," Oral presentation at the *40th Micro and Nano Engineering Conf.*, Lausanne, Switzerland, September 22-26, 2014

[8] **T. W. Collins**, P. Mokarian-Tabari, C. Cummins, J. D. Holmes, and M. A. Morris, "Highly Ordered and Aligned Block Copolymer Templates via Graphoepitaxy," Poster presentation at the *Tyndall Internal Conf.*, Cork, Ireland, April 25, 2013

[9] P. Mokarian-Tabari, **T. W. Collins**, R. Senthamaraikannan, J. D. Holmes, and M. A. Morris, "Rapid Self- Assembly and Perpendicular Alignment in lamellar PS-b-PEO System for Fabrication of Sub 20 nm Nanolithography Templates," Oral and Poster presentation at the *American Physical Society March Meeting*, Boston, MA, February 27 - March 2, 2012

[10] P. Mokarian-Tabari, **T. W. Collins**, J. D. Holmes, and M. A. Morris, "A novel approach to achieve perpendicular long range order alignment in lamella PS-b-PEO system," Oral and Poster presentation at the *American Physical Society March Meeting*, Dallas, TX, March 21-25, 2011

[11] P. Mokarian-Tabari, **T. W. Collins**, and M. A. Morris, "An in-situ study of structure evolution in block copolymer thin films of PS-PEO during solvent vapor annealing," Oral and Poster presentation at the *American Physical Society March Meeting*, Portland, OR, March 15-19, 2010

Table of Contents

Declaration ii
Abstract iii
Acknowledgements v
Published Articles vi
Submitted Articles vii
Articles in preparation vii
Conferences vii

Chapter 1. Introduction 1

1.1 Microelectronics and Miniaturisation 2
1.2 Self-Assembly 6
1.3 Block Copolymers 7
1.3.1 Microphase Separation 8
1.3.2 Phase Behaviour 10
1.3.3 Thin Films 13
1.3.3.1 Interfacial Constraints 14
1.3.3.2 Film Thickness 15
1.4 Directed self-assembly 17
1.4.1 Graphoepitaxy 17
1.4.2 Chemoepitaxy 18
1.5 Applications of Block Copolymer Nanostructures 19
1.6 Thesis Overview 21
1.7 References 23

Chapter 2. Cyclical "Flipping" of Orientation in Hexagonal Forming Polystyrene-*b*-Poly(ethylene Oxide) 30

2.1 Abstract 31
2.2 Introduction 31
2.3 Experimental 33
2.3.1 Materials 33
2.3.2 Characterization 33
2.4 Results 34
2.4.1 Cyclic Transition 34
2.4.2 Thickness effect 37
2.4.3 In-situ time resolved light scattering 38
2.4.4 Graphoepitaxy 41
2.5 Conclusions 43
2.6 References 44
2.7 Appendix 48

Chapter 3. Brushless Microphase Separation of Lamellar Polystyrene-*b*-Poly(ethylene Oxide) Thin Films 51

3.1 Abstract 52
3.2 Introduction 52
3.3 Experimental 54
3.3.1 Polymers 54
3.3.2 Stepwise thermo/ solvent Annealing 54
3.3.3 Film characterisation 55
3.3.4 Etch and pattern transfer 56
3.4 Results and Discussion 57
3.4.1 Stepwise Annealing 57
3.4.2 Influence of Molecular Weight 61
3.4.3 Pattern transfer 62
3.5 Conclusions 63
3.6 References 64
3.7 Appendix 69

Chapter 4. Dimensional and Defectivity Data Collection for Block Copolymer Thin Film Metrology 71

4.1 Abstract 72
4.2 Introduction 72
4.3 Experimental Method 74
4.3.1 Materials 74
4.3.2 Process 75
4.3.3 Characterization 76
4.3.4 Image Analysis 76
4.4 Results 76
4.4.1 Dots Pattern Analysis 78
4.4.2 Application of Dot Analysis 84
4.4.3 Line Pattern Analysis 87
4.4.4 Application of Line Analysis 95
4.5 Conclusions 97
4.6 References 97

Chapter 5. Large Block Copolymer Self-Assembly for Fabrication of Subwavelength Nanostructures for Applications in Optics 104

5.1 Abstract 105
5.2 Introduction 105
5.3 Experimental 107
5.3.1 Film preparation 107
5.3.2 Pattern transfer 108
5.3.3 Optical analysis 108
5.3.4 Dimensional analysis 109
5.3.5 3D model. 109
5.3.6 Microscopy 109
5.3.7 Simulation 110
5.4 Results and Discussion 110
5.4.1 Nanopattern Formation and BCP Characterization 110
5.4.2 Optical Characterization 112
5.4.3 Omnidirectional broadband antireflective SiNPs. 115
5.4.4 Simulation. 119
5.5 Conclusions 120
5.6 References 120
5.7 Appendix 124

Chapter 6. Conclusions and Future Work 129

6.1 Abstract 130
6.2 References 132

Common Abbreviations and Acronyms:

AFM: Atomic Force Microscope

AOI: Angle of Incidence

BCP: Block Copolymer

CD: Critical Dimension

DSA: Directed Self-Assembly

EBL: Electron Beam Lithography

EDAX: Energy Dispersive X-Ray Analysis

EUV: Extreme Ultraviolet

***f*:** Block volume fraction

FER: Fingerprint Edge Roughness

FIB: Focused Ion Beam

FTIR: Fourier Transform Infra-Red

GaN: Gallium Nitride

HSQ: Hydrogen Silsesquioxane

ITRS: International Technology Roadmap for Semiconductor

L_0: Period

LER: Line Edge Roughness

LWR: Line Width Roughness

M_n: Molecular weight

***N*:** Degree of polymerization

NIL: Nanoimprint Lithography

P2VP: Poly(2-vinylpyridine)

P4VP: Poly(4-vinylpyridine)

PB: Poly(butadiene)

PDMS: Poly(dimethylsiloxane)

PEO: Poly(ethylene oxide)

PEO: Poly(ethylene oxide)

PHEMA: Poly(hydroxyethyl methacrylate)

PI: Poly(isoprene)

PMMA: Poly(methyl methacrylate)

POSS: Polyhedral Oligomeric Silsequioxane

PS: Poly(styrene)

PV: Photovoltaic

SCFM: Self-Consistent Mean Field

SEM: Scanning Electron Microscopy

Si: Silicon

SiNP: Silicon Nanopillar

SOA: State-of-the-Art

STEM: Scanning Transmission Electron Microscopy

XPS: X-ray Photoelectron Spectroscopy

χ: Flory-Huggins Interaction Parameter (Chi)

Chapter 1

Introduction

1.1 Microelectronics and Miniaturisation

The history of integrated circuit technology can be traced back all the way to Bell Labs in 1940. Russell Ohl, while investigating high-frequency amplifiers for use in radar, produced a crystal photocell, whose conductance varied far more than anything seen previously. With the aid of Joseph Becker and Walter Brattain, it was shown that there was a crack in the crystal, and that either side had a slightly different chemical composition. What they had discovered was a solid state diode, and the crack was a junction. This led to the concept on semiconductors [1]. Later, William Shockley began research on a "triode"-like semiconductor device with Walter Brattain and John Bardeen. On the 23rd of December, 1947, often deemed the birthplace of the transistor, using a piece of gold foil glued to a plastic wedge and pressed down onto the surface of a germanium crystal, they demonstrated the first transistor, known as the "PNP Point-Contact Germanium Transistor", for which they won the Nobel Prize in Physics in 1956. These discoveries eventually led to the development of the field-effect transistor, the foundation of all modern-day computing and the semiconductor industry [2].

This was achieved through the development of integrated circuits in 1958, credited to Robert Noyce and Jack Kirby, for which Kirby won a Noble Prize in 2000. These consisted of large numbers of devices, transistors and other key components, interconnected on a single substrate. The possible applications of integrated circuits sparked a huge increase in research and development [3]. Since then a competition to perpetually improve performance has existed in the industry, primarily through reducing device size and increasing density. This "race to the bottom" was epitomized by Intel co-founder Gordon Moore's paper in 1965, where he predicted that the number of transisters on an integrated circuit would double about every 18 months [4].

This prediction has become known as “Moore’s Law” and a self-fulfilling prophecy for the microelectronics industry for over 50 years [5], as depicted in Figure 1.1.

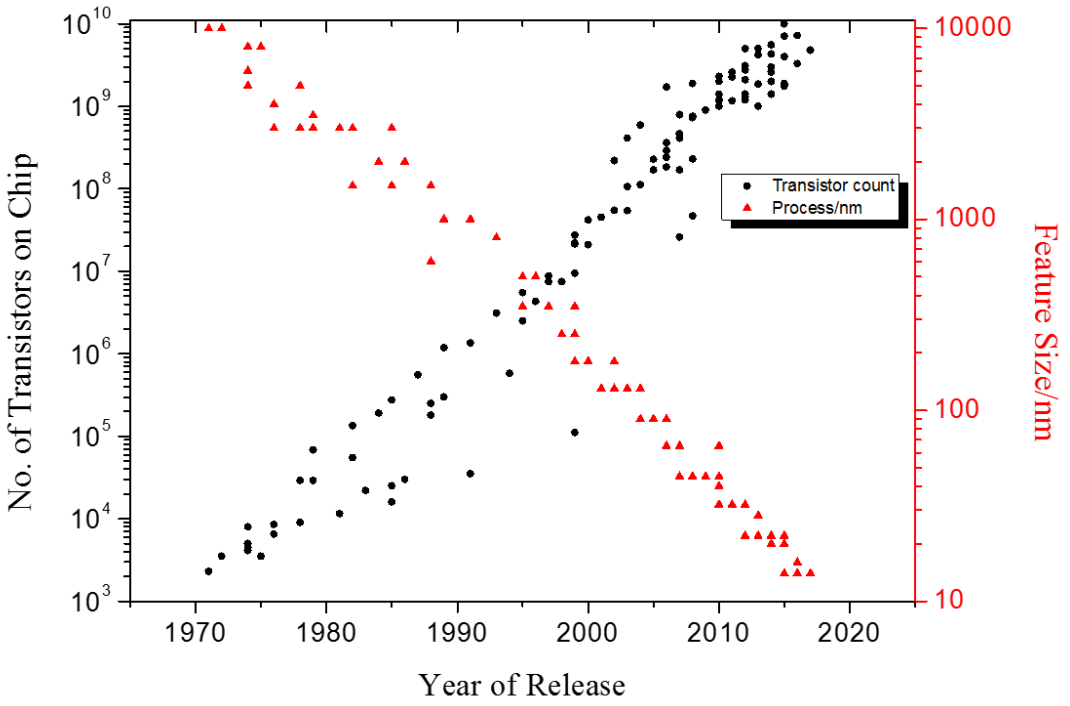


Figure 1.1: Graphical representation of Moore’s Law, showing the exponential increase in the number of transistors per microchip and the decrease in feature size. Adapted from data collected [6].

The impressive advances in miniaturization have been heavily dependent on continuous developments in photolithography [7]. In this process, a photosensitive polymer film, or photoresist, is applied to a silicon surface. It is then exposed to ultraviolet (UV) light, projected through a photomask. This produces a chemical change in the photoresist, affecting the solubility of the material in a pattern emulating the photomask. This pattern is then exposed by immersing the film in developer, removing the soluble material and leaving a “mask” of insoluble polymer, Figure 1.2. This mask can then be etched, transferring the pattern into the underlying substrate. Through repeated material deposition steps, the complex architecture required for integrated circuits can be produced [8]. This method has allowed the progress from

the Intel 4004 microchip in 1971, with 2300 transistors and a feature size of 10 µm, to Samsung and Intel preparing for production of microchips with 10 nm features [9].

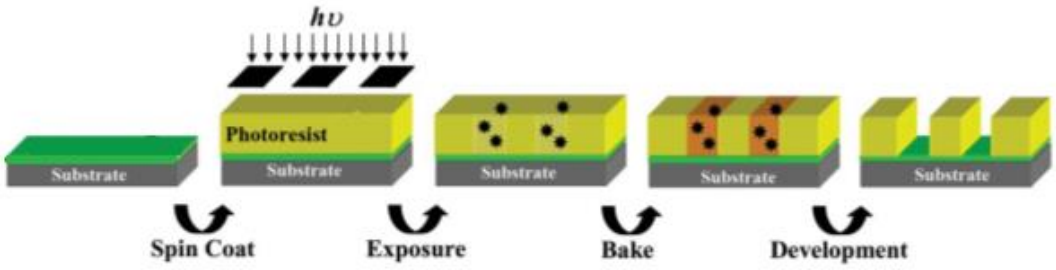


Figure 1.2: Schematic representation of photolithography process. Light is used to transfer the pattern from a mask to a photoresist. This pattern is then etched into the substrate and the resist stripped (reprint Nealey *et al* [10]).

Photolithography's ability to produce many chips on a single silicon wafer simultaneously makes it an efficient and cost effective process. However, in order to compete in the market and keep consistent with Moore's law, the semiconductor industry has had to focus huge resources on improving their lithography processes. Initially, improvements were achieved by adjusting light sources, starting at 436 nm and now utilising 193 nm sources. Techniques such as immersion lithography and multi-patterning have been employed to push the limits of current processing methods to the 22 nm and 16/14 nm feature size [11]–[13]. However, it is fast approaching the resolution limitations that can be achieved, with the technical challenges involved in lowering the light source wavelength, 157 nm, proving prohibitive [7], [14]. In addition, as size decreases, resolution, throughput and line edge roughness (LER) become major roadblocks, as their effect on device performance increases along with costs [15]–[17].

To continue development of integrated circuits and achieve <10 nm feature size, a new generation of lithographic techniques are being investigated. Among those under consideration are top-down methods including extreme ultraviolet lithography, electron-beam lithography, and nanoimprint lithography [18].

Extreme ultraviolet (EUV) lithography has received significant industry interest as it follows the progression in photolithography. By using 13.5 nm light, it is capable of extending optical lithography to the sub-10 nm range [19]. However, continuing issues with source output, pattern roughness and the high cost of integration have thus far prevented its introduction [20], [21].

Electron-beam lithography offers an alternative to optical lithography. By using a focused beam of charged energetic particles, it achieves a resolution down to 1-2 nm without the need for a photomask. Its primary drawback is the requirement to write the pattern, focusing the beam on individual features in a serial process. This greatly increases production time compared to the exposure process for optical lithography [22], [23].

Nanoimprint lithography creates patterns by mechanically deforming a resist layer using a master mask. This is a low-cost, high-output method, able to reach the sub-20 nm range. However, it is prone to defects from particulates, which can damage the mask and impede output, requiring extensive control procedures [24], [25].

Going forward, it is generally accepted that alternatives to purely "top-down" fabrication methods must be employed. The microelectronics industry has already invested heavily in "bottom-up" techniques. It is predicted that these methods can overcome the limitations of traditional photolithography while keeping integration

costs to a minimum. One potential technique that has shown great promise is self-assembly of block copolymers [26], [27].

1.2 Self-Assembly

Self-assembly describes the spontaneous organisation of a system of pre-existing, nanoscale units into stable, well-defined structures [28]. This process has been the focus of a considerable amount of research in recent years, as it describes many biological systems, such as the folding of tRNAs and the formation of DNA. Self-assembly is one of the few practical strategies for the formation of ordered nanostructures. It is also hoped to bridge the gap between photolithography and further reductions in feature size [12].

Whitesides *et al* have identified two types of self-assembly. Static self-assembly describes systems that, at equilibrium, do not release energy, and for the formation of an ordered structure may require energy input. Dynamic self-assembly occurs where structures or patterns only occur as the system is in flux and dissipating energy [29].

Molecular self-assembly does not involve any chemical reactions, but instead uses weak, non-covalent, intermolecular forces to arrange the components, i.e. van der Waals, electrostatic, hydrophobic interactions, hydrogen and coordination bonds. The process is driven by the system attempting to attain its minimum free energy through minimising repulsive forces and maximising attractive forces that are experienced. The thermodynamics of self-assembly are expressed in the Gibbs free energy equation (Equation 1.1):

$$\Delta G_{sa} = \Delta H_{sa} - T\Delta S_{sa} \qquad (1.1)$$

In order for the process to be spontaneous, the change in free energy must be negative. ΔH_{sa} is representative of the intermolecular forces between the assembling units. ΔS_{sa} represents the degree of disorder in the system, and decreases as it becomes more ordered. As the entropy is predominately negative as order increases, the process must be enthalpy driven. In addition to this, it can be seen that the process is temperature dependent, and above a specific temperature, self-assembly does not occur. This is known as the order-disorder temperature [28]–[30]

Directed, or template, self-assembly (DSA) is an extension of the self-assembly process. It describes a system where external factors such as physical templates affect the self-assembly in a desirable manner. This can include chemical or topographical templates, as well as electrical, thermal and surface fields. Directed self-assembled materials are being considered for integration into nanoelectronic patterning applications, as a potential replacement for conventional photoresists in order to achieve molecular-level control on feature size and reduce line edge roughness [10], [31]. Such materials include nanowires and nanotubes, graphene and functionalized biomaterials. The most likely candidates are block copolymers [16], [32].

1.3 Block Copolymers

Block copolymers (BCP) consist of two or more chemically incompatible and dissimilar polymeric chains known as blocks, which are covalently bonded to one another. Block copolymers can exist as diblock, triblock and multiblock systems, and can be incorporated into complex architectures, as illustrated in Figure 1.3.

Interest in the unusual properties of block copolymers began shortly after they were first reported in 1952. In the subsequent years, a great deal of work has been done in attempting to understand their behaviour and morphologies [16].

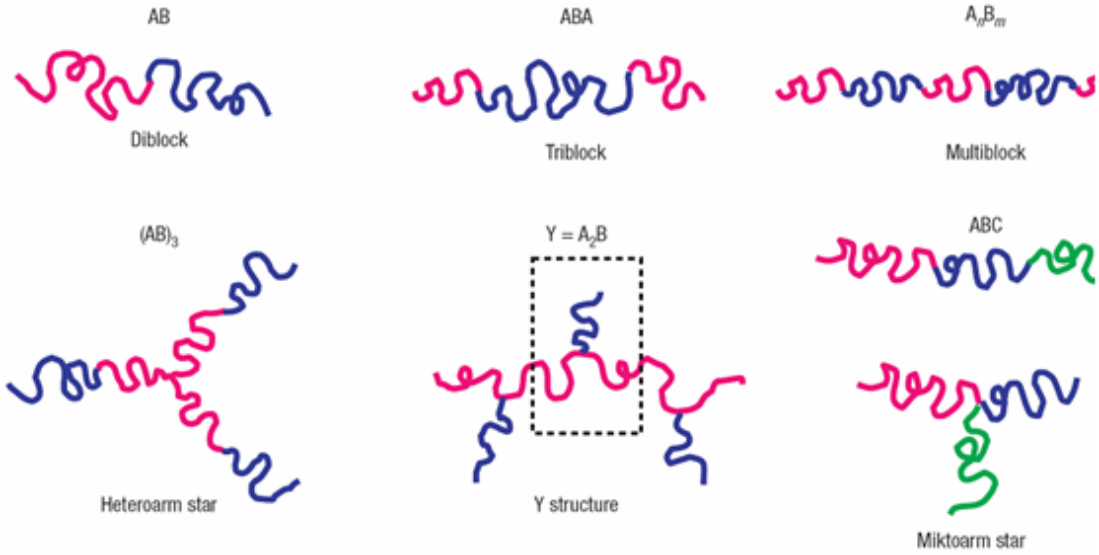


Figure 1.3: Examples of block copolymer architectures including linear di-, tri- and multiblock copolymers, heteroarm stars, Y structures as well as linear and miktoarm star terpolymers (reprint Ruzette and Leibler [33]).

There are many proposed applications for block copolymers, primarily as nano-lithographical masks, but also as templates for forming fuel cells, batteries, and optoelectronic devices, owing to their ability to form regular repeating structures over large areas and tuneable feature size in the 5-50 nm range. The tailoring of individual block chemistry also adds to their versatility. However, one of the main challenges in employing block copolymers is lack of long range order, or imperfections in the orientation. Overcoming these difficulties has been the focus of much research [11], [26], [34].

1.3.1 Microphase Separation

In polymer blends, consisting of a binary homopolymer mixture, repulsion between the immiscible A and B blocks will lead to macrophase separation at equilibrium. This is due to thermodynamic incompatibility between the two blocks, which separate in order to minimise the contact area between them. However, in the case of block copolymers, there exists a covalent bond holding A and B together, preventing

macrophase separation. This constraint leads to the formation of microscopic heterogeneities in the composition on the length scale of the individual polymer molecules, and generates an interface between the A and B blocks. It is this micro separation that makes block copolymers so appealing as they can form well-ordered repeating domains, as can be seen in Figure 1.4 [11], [35], [36].

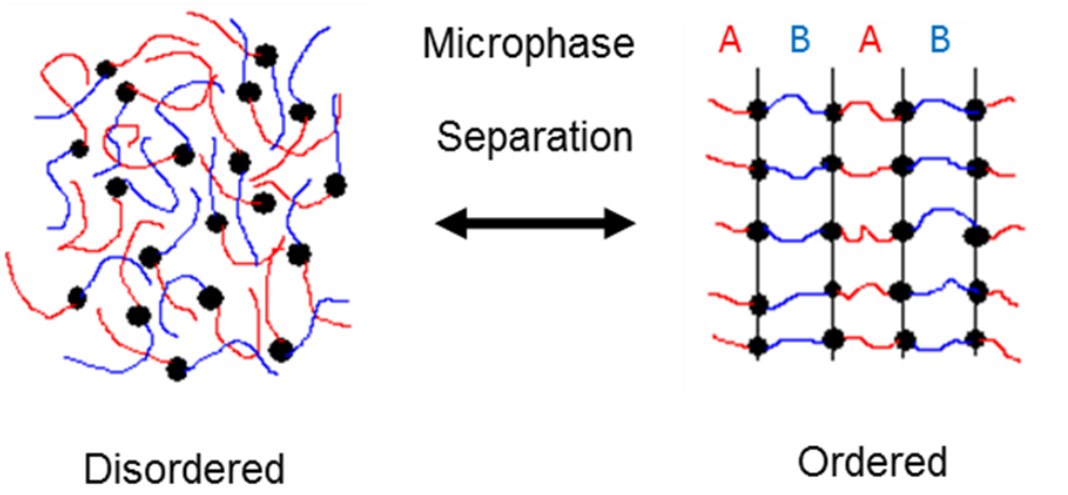


Figure 1.4: Illustration of microphase separation of a diblock copolymer system following casting from solution to form a thin film on a substrate.

Within thin films, the structures that form in the block copolymer melt are a result of two competing factors: interfacial energy between the two blocks, which is an enthalpic energy, and polymer chain stretching, which is entropic in nature [37]. In segregation, the equilibrium nanodomain structure acts to minimize unfavourable mixing without overstretching the blocks, i.e. balance the enthalpic and entropic energies. In order to phase separate, sufficient mobility must be given to the polymer chains to allow mass transfer. This is typically achieved by thermally annealing the system to above the glass transition temperature. Heating to above the order-disorder temperature causes the system to become disordered, as the entrophy forces are temperature dependant [38]. Alternatively, solvent annealing has been explored as a

method in achieving phase separation, where the system is placed in a solvent atmosphere below the glass transition temperature. This has been attributed to solvent swelling of the polymer film, thereby lowering the glass transition temperature [39]–[41] as well as preferential interaction between the solvent and one of the blocks [42].

1.3.2 Phase Behaviour

The phase behaviour of bulk block copolymers is controlled via three parameters: the block volume fraction (f), the degree of polymerization (N), and the A-B Flory-Huggins interaction parameter (χ). These dictate the morphologies that are formed, which for block copolymers are typically cubic, cylindrical, lamellar or bicontinuous gyroid. The Flory-Huggins equation (Equation 1.2) describes the free energy of mixing two polymers [28], [34], [35], [43]:

$$\Delta G_{mix}/k_bT = (1/N_A)\ln(f_A) + (1/N_B)\ln(f_B) + f_A f_B \chi \quad (1.2)$$

The degree of polymerization is a measure of the total number of monomer units in the polymer chain and is proportional to the configurational entropy, as well as determining the size of the microdomains [44].

$$N = N_A + N_B \quad (1.3)$$

The composition of the block copolymer is described by the volume fraction (f), such that the fraction of each block is described by:

$$f_A = N_A / N \quad (1.4)$$

$$f_B = N_B / N \quad (1.5)$$

χ is related to the unfavourable A-B monomer interactions and is a function of both the chemistry of the monomers and temperature, such that:

$$\chi = a/T + b \tag{1.6}$$

where a and b are constants determined experimentally for a specific polymer blend. Experimentally, χ can be controlled via temperature [34], [35]. Equation 1.2 can rewritten in terms of Hildebrand solubility parameters (δ), which measure the tendency for one material to dissolve in another via intermolecular forces, specifically dispersion, hydrogen bonding and polar forces [28], [45], [46].

$$\chi_{AB} = (V_r/RT)(\delta_A - \delta_B)^2 \tag{1.7}$$

V_r is an arbitrary reference volume, normally taken as the molar free volume [47]. Therefore, as χ_{AB} describes the segregation between individual monomers, the total strength of segregation experienced by the two blocks is proportional to $\chi_{AB}N$. A combination of f and $\chi_{AB}N$ determines the morphology that the block copolymer melt forms. The minority block will adopt different domain structures in order to minimise the free energy of the system. For example in a PS-*b*-PI system, $f_{PS} < 0.17$ generates a cubic structure, while $0.17 < f_{PS} < 0.28$ shifts to hexagonal. A bicontinuous gyroid structure exists from $0.28 < f_{PS} < 0.34$. And lamellar is present from $f_{PS} = 0.34$ to 0.62. Further increases produce inverted phases, i.e. PI is the minor block [35]. These phase transition changes with block copolymer ratio can be expressed as a phase diagram, as shown in Figure 1.5.

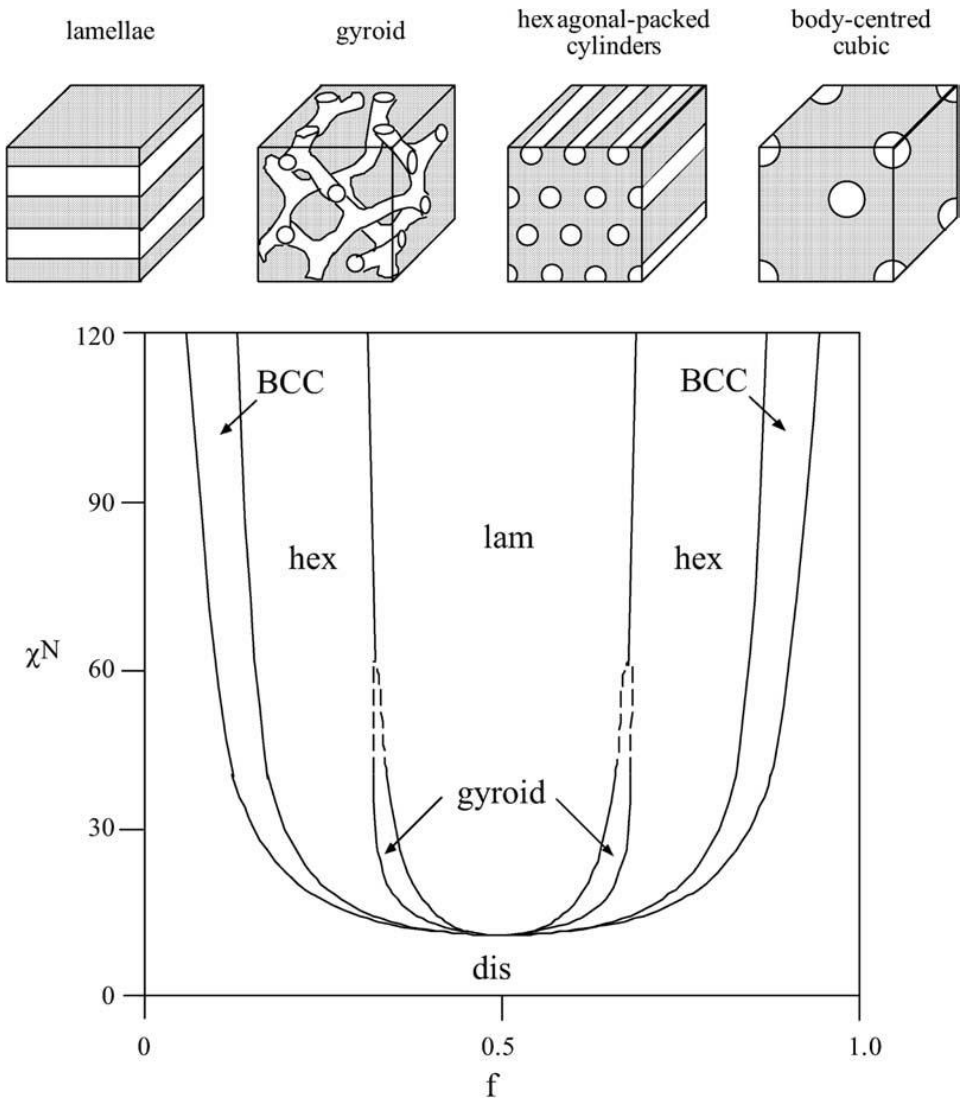


Figure 1.5: Phase diagram showing varying morphologies formed by block copolymer self-assembly(reprint Castelleto and Hamley [44])

Whilst developing a theoretical understanding of block copolymer melts and morphologies, many theories have been employed, but are limited to certain areas of the phase diagram, such as weak segregation limit and strong segregation limit. To tie these together, self-consistent mean field (SCMF) theory has been proposed, which has shown good agreement with experimental results [43], [48]. It predicted, that for a system with $f = 0.5$, $\chi_{AB}N < 10.49$ entropic forces are dominant and the block copolymer exists in a homogenous state. At $\chi_{AB}N \approx 10.49$, there is a balance between entropy and enthalpy such that weak segregation may occur. This phase transition is

known as the order-disorder transition (ODT). When $\chi_{AB}N > 10.49$, enthalpic factors dominate, allowing for strong segregation of the blocks [35], [49]. This has been illustrated in Figure 1.6.

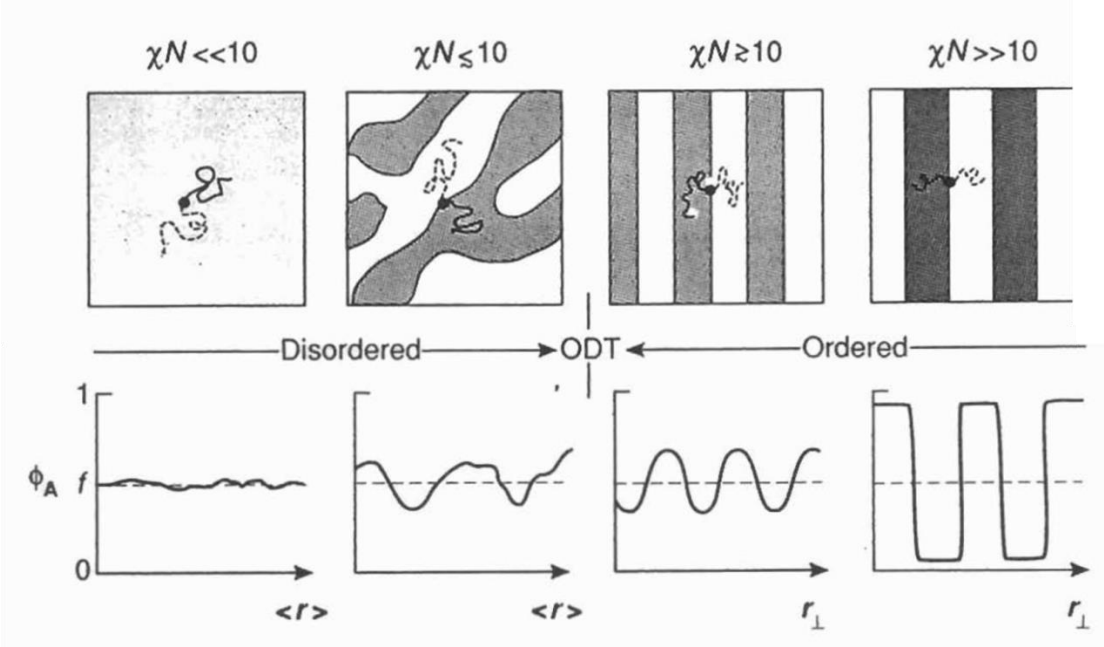


Figure 1.6: Evolution of structure with increasing $\chi_{AB}N$ for a symmetric diblock copolymer [35].

It should be noted that transitions into order-disorder (ODT) region by having $\chi_{AB}N < 10.49$ or by exceeding the order-disorder transition temperature (T_{ODT}) are reversible for block copolymer systems [48].

1.3.3 Thin Films

The properties of sub-micron thick films differ greatly from those in the bulk. In thin films of block copolymers, properties such as the glass transition temperature, the chain diffusion coefficients and viscosity change with decreasing thickness [50]. Additional factors have an impact on the phase separation and morphology of the block copolymer. These include atmosphere-polymer interface and polymer-substrate interface interactions, as well as interplay between the copolymer's natural repeat

spacing, L_0 and the film thickness. As a result, the morphologies formed in thin films are more complex than in the bulk. There has been considerable research in the last decade into understanding and exploiting these factors due to their increasing effect as film thickness decreases [51]. The additional interfaces cause the film components to reconstruct to achieve the lowest energy state. In practice, this causes the block with the lowest interfacial energy to accumulate at the substrate-polymer surface, and the polymer with the lowest surface tension (γ) to preferentially form at the atmosphere-polymer, or free, surface [52]. Furthermore, as the thin film confines the block copolymer, if the film thickness is a non-integer multiple of L_0 then unfavourable morphologies of topographical features may form [50].

1.3.3.1 Interfacial Constraints

One of the major causes of interest in block copolymer thin films is their ability to form highly orientated microdomains. The orientation of domains can be directly controlled by manipulating the substrate-polymer and polymer-atmosphere interfaces as to induce preferential energetic constraints.

Substrate effects on the film can be controlled by changing the substrate material, or alternatively modifying the surface chemistry in various manners. In addition, controlling the "wetting" properties of the polymer with respect to the substrate allow for greater coverage of the polymer. This property is often quantified by contact-angle measurements, which measure the degree of hydrophobicity as a function of angle [53]. For example, on bare silicon, lamellar forming PS-*b*-PMMA will orientate parallel to the substrate, as PMMA preferentially wets silicon [54]. Russell *et al* showed that using a gold layer on the silicon altered the chemistry such that the PS preferentially wetted the substrate [55]. Other substrate materials include titanium,

copper, germanium, silicon nitride and sapphire. Surface modification approaches include the use of polymer brush layers or self-assembled monolayers. Polymer brush layers are typically random copolymers, made up with the same monomers as the block copolymer but in a random order, to form a monolayer which acts as a neutral interface to the block copolymer. They can be end or side grafted to the substrate. One such random copolymer, polystyrene-*random*-poly(methylmethacrylate) (PS-*r*-PMMA), has been extensively investigated as a brush for the PS-*b*-PMMA system [56]–[58]. Grafted homopolymers can also be used, typically to improve wetting by the block copolymer to improve surface coverage [59]–[61]. However, it has also been shown that in some cases, the wetting properties of homopolymer brushes, such as polydimethylsiloxane, can be manipulated through UV-ozone treatment[62]. Self-assembled monolayers (SAMs) based surface modifications involve using small molecules such as thiol-terminated molecules [54], [63] and chlorosilane molecules [61], [64]–[66].

1.3.3.2 Film Thickness

In addition to the interfacial interactions, there is the further constraint imposed by the commensurability between the film thickness (t) and copolymers' characteristic length scale (L_0). The impact of film thickness is illustrated in Figure 1.7.

Morphologies which develop through the surface and the substrate boundary conditions demand that the most energetically compatible block be expressed at each surface. When different components of the block copolymer are present at each interface the film is said to be asymmetric, alternatively, block copolymer films that exhibit the same block at each surface are termed symmetric.

Symmetric films exhibit a similar series of stable smooth states when the film thickness is an integer multiple of the characteristic length scale. If the local film thickness deviates from the appropriate criteria by a sufficient amount (i.e. if t and L_0 are incommensurate) topographical features (typically islands or holes) of height equivalent to L_0 appear at the surface. If the film is sufficiently thick these topographic features are not observed as the incommensurability between t and L_0 can be distributed over many layers of the film. On the other hand, if the film is sufficiently thin it can dewet or rupture forming a variety of spinodal patterns [67].

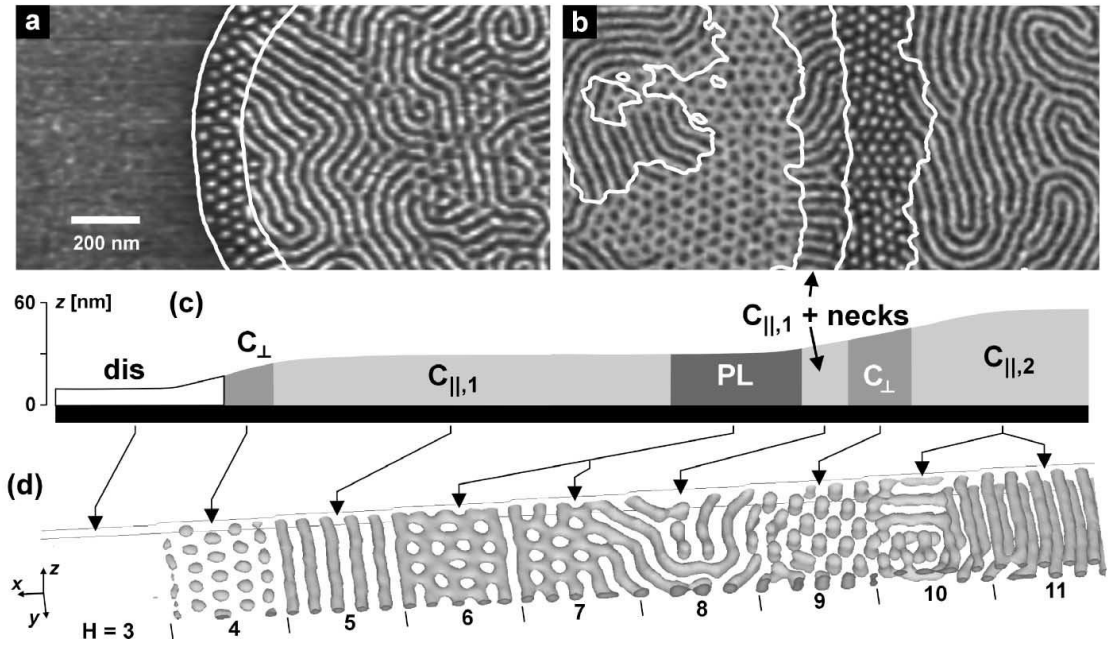


Figure 1.7: (a,b) Tapping mode AFM images of a PS-PB-PS triblock copolymer following solvent annealing. Structures as separated by white lines corresponding to areas of differing thickness. (c) Height profile. (d) Modelled structure of a triblock. C⊥ and C|| denote cylinders perpendicular or parallel respectively to the substrate, and PL denotes perforated lamellae (reprint Knoll *et al* [68]).

1.4 Directed self-assembly

While localised ordering of block copolymers can be readily achieved, to be successfully utilised in various applications, the ability to control the long range orientation of their microphase separation is required. DSA are methods of aligning block copolymers to improving the pattern quality and attain long-range ordered nanopatterns by application of external forces on them. There are two predominant categories of DSA; physical pattern alignment, known as graphoepitaxy, and chemical pattern alignment, known as chemoepitaxy [69]. Both methods require a combination of a top-down fabrication of guiding patterns followed by a bottom-up self-assembly of the block copolymer, as illustrated in Figure 1.8.

1.4.1 Graphoepitaxy

Graphoepitaxy is a technique where physical features such as trenches are utilised to provide topographical confinement and direct the self-assembly to induce order in the pattern. These topographical patterns are fabricated by lithography, with the pattern being etched directly into the substrate [70], or alternatively into e-beam resist materials, such as HSQ [71] and POSS [72]. Initially shown by Segalman *et al* [73], graphoepitaxy has seen huge interest as a method of achieving well-ordered, low defect patterns due to the relative ease in which topographic patterns can be fabricated by conventional lithographic methods. However to achieve this, it is necessary to control both substrate surface and side wall surface affinities independently [74], [75]. The issue with this method is the loss of utilisable surface area, thereby reducing the total number of elements that can be fabricated [27]. Ross *et al* have done extensive work on the use of PS-*b*-PDMS using graphoepitaxy [60], [76], which due to its high χ, could extend the minimum feature size to <10 nm.

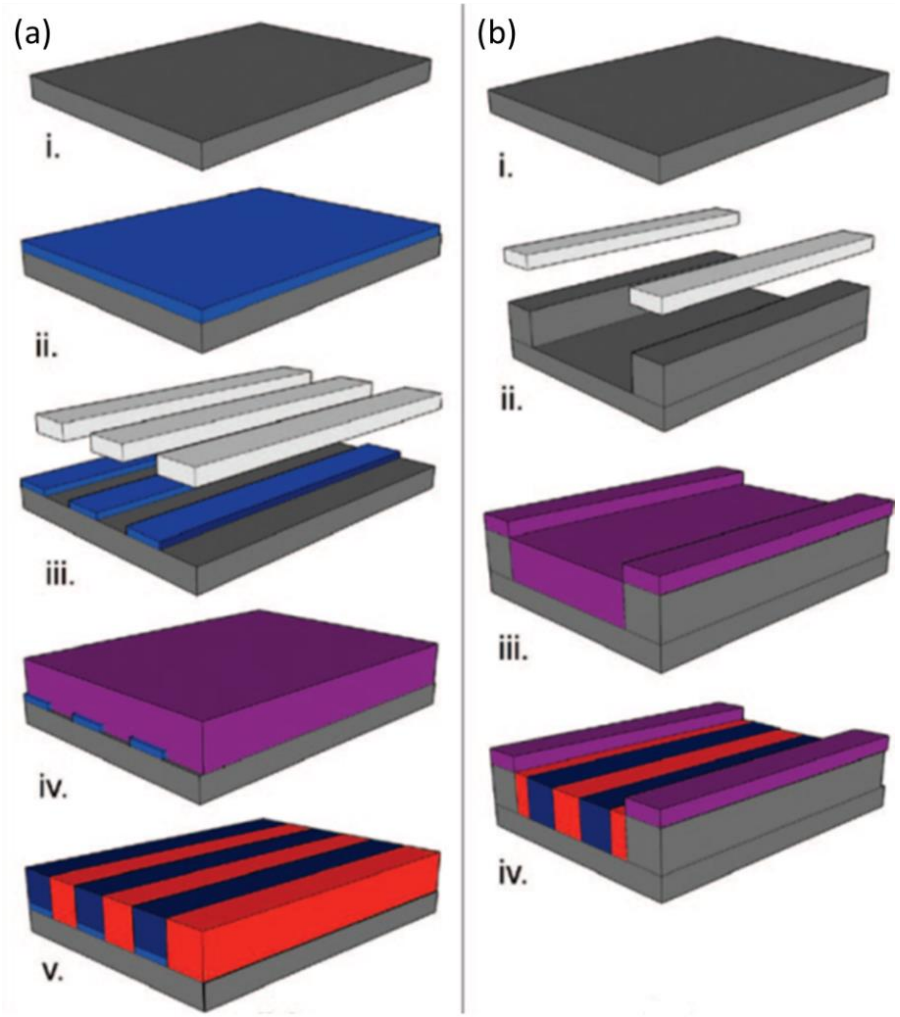


Figure 1.8: Schematic process for (a) chemoepitaxy: (i) bare silicon substrate, (ii) coating with a chemical surface layer, (iii) creating a chemical pattern by exposure to ultraviolet light through a mask and a chemical develop, and (iv,v) self-assembly of a BCP film onto the chemical pattern. (b) Graphoepitaxy (i) bare silicon substrate, (ii) lithographic patterning of topographic surface pattern and (iii,iv) self-assembly of a block copolymer film onto the topographic pattern (reprint Black [77]).

1.4.2 Chemoepitaxy

An alternative method to control the ordering of block copolymer patterns is chemoepitaxy. Chemoepitaxy, or templating, describes a chemically patterned surface where the patterns are similar to the domain size (L_0) of the block copolymer. It typically comprises of an interfacial layer, such as a brush layer, that is patterned via

lithography to induce affinity with a particular block of the block copolymer [78]. This method has become the most actively researched method of creating lithographic quality masks from block copolymer patterns, and hugely influenced by Nealey and co-workers. This method has been under development by Nealey *et al* since 2003 [10], [79]–[81] and has resulted in the LiNe (Liu-Nealey) flow at IMEC [82], [83], a process flow in development for integrated circuit manufacturing and is approaching the defectivity levels required for integration.

1.5 Applications of Block Copolymer Nanostructures

Block copolymers are capable of creating controllable, highly ordered nanoscale structures. Investigations into the use of these nanopatterns as templates for the fabrication of nanodevices, as etch masks, and the controlled placement of nanoparticles are on-going. The differing chemistry of the component blocks can be utilized to order nanoparticles and act as a scaffold following self-assembly [37], or act as nanoporous templates following selective removal of one of the blocks [84].

One of the areas where block copolymers have gained great interest is in the fabrication of nanoelectronics at length scales inaccessible to optical lithography (<14 nm) [13]. The use of directed self-assembly can produce ordered patterns at a substrate surface. Due to the difference in chemical composition of the blocks, it is possible to selectively remove one block via etching. Chemical or "wet" etching uses a solvent or acid that is selective to one of the blocks [85]. Plasma or "dry" etching makes use of the differing chemical structures of the blocks, preferentially eating away one block over the other using mixtures of ionised gases [86]. The resulting pattern can then be transferred to the substrate via two methods.

In the first method, the remaining block acts as a sacrificial etch resist, allowing for direct transfer of the pattern to the substrate [86]. This approach allows for easy substrate processing, however, it suffers from poor etch selectivity during transfer [87]. An alternative is to use the space vacated by the selective etch as a template for the deposition of hard mask material, such as iron or aluminium oxide [88], [89]. This greatly increases the etch contrast, but require additional steps in processing.

These masks allow for the pattern to be transferred to a device layer using plasma etching. Plasma etching utilises a partially ionised gas which is energised using an external magnetic field. They are categorised as reactive ion etching (RIE), which use capacitive coupling plasma, and inductive coupled plasma (ICP), which uses induction to generate the plasma. The ICP technique is capable of much higher plasma densities, and therefore etch rates [90], [91].

Block copolymers can also be used as nanoporous templates. This can be achieved by the selective removal of one of the blocks, followed by backfilling with the desired material. The remaining block can then be removed, leaving discrete, ordered patterns of material. This method has several applications, such as seed templates for nanowire growth [92], the creation of storage media [93], and the fabrication of functional surfaces [94]. Templating can be achieved by an alternate route, through the incorporation of metal salts or nanoparticles directly into the BCP film. In this way, the pattern acts as a scaffold to guide the alignment of the material [95].

Additionally, as more functionalised block copolymer systems are synthesised, more applications become available. The development of conductive BCP systems, for example, has allowed for their incorporation into organic photovoltaic (OPV) devices [96], [97].

1.6 Thesis Overview

As described here, block copolymers provide potential methods for fabricating nanoscale structures using 'bottom-up' self-assembly. This thesis will focus on the use of three block copolymer systems, namely PS-*b*-PEO, PS-*b*-PMMA, and PS-*b*-P2VP.

In Chapter 2, solvent annealing induced evolution of a cylinder PS-*b*-PEO block copolymer self-assembled pattern is discussed. Flipping of the orientation is observed and control over the alignment is demonstrated. Timothy William Collins performed the block copolymer experiments and AFM. Parvaneh Mokarian-Tabari performed the *in-situ* light scattering, ellipsometry, sample etching, and coordinated the research. SEM and TEM was performed by the staff of AML (Advanced Microscopy Laboratory) in CRANN. Intel provided the patterned substrates.

A novel step-wise, thermal-solvent annealing process is demonstrated in Chapter 3. Its ability to induce perpendicular orientation within a lamellar PS-*b*-PEO block copolymer without the use of a neutral layer is shown. Pattern transfer and scalability of this system is discussed. Timothy William Collins and Parvaneh Mokarian-Tabari performed the block copolymer experiments. Timothy William Collins performed the AFM. Parvaneh Mokarian-Tabari performed the sample etching, and coordinated the research. SEM and TEM was performed by the staff of AML, CRANN and at Intel.

Chapter 4 focuses on the development of an application for the quantitative analysis of self-assembled block copolymer patterns. The method is demonstrated through the optimisation of processing conditions of PS-*b*-PMMA cylinder and lamellar block copolymers. Timothy William Collins performed the block copolymer experiments, and developed the application for pattern analysis. Barbara Kosmala performed the sample etching.

In Chapter 5, the fabrication of nanostructured surfaces for optical applications through the use of a large molecular weight PS-*b*-P2VP block copolymer templated process is discussed. Parvaneh Mokarian-Tabari coordinated the research project. Ramsankar Senthamaraikannan performed the block copolymer experiments and AFM, SEM, STEM and EDAX. Timothy William Collins performed film staining, AFM and SEM, developed the 3D model, and performed dimensional analysis on the patterns. Colm Glynn and Colm O'Dwyer performed the optical characterizations, Vis-IR and angle dependant experiments. Cian Cummins performed FIB. David Nugent performed simulations.

Chapter 6 summarises the key accomplishments of each chapter and discusses the future development of block copolymer nanopatterns for nanofabrication.

1.7 References

[1] M. Riordan and L. Hoddeson, "Origins of the pn junction," *IEEE Spectr.*, vol. 34, no. 6, pp. 46–51, 1997.

[2] R. G. Arns, "The other transistor: early history of the metal-oxide semiconductor field-effect transistor," *Eng. Sci. Educ. J.*, vol. 7, no. 5, p. 233, Oct. 1998.

[3] E. Braun and S. MacDonald, *Revolution in Miniature: The History and Impact of Semiconductor Electronics Re-explored in an Updated and Revised Second Edition*, 2, illustr ed. Cambridge University Press, 1982.

[4] G. E. Moore, "Cramming more components onto integrated circuits," *Electronics*, vol. 38, no. 8, pp. 114–118, Sep. 1965.

[5] P. J. Denning and T. G. Lewis, "Exponential Laws of Computing Growth," *Commun. ACM*, vol. 60, no. 1, pp. 54–65, Dec. 2016.

[6] "Transistor Count." [Online]. Available: https://www.revolvy.com/. [Accessed: 03-Apr-2017].

[7] C. G. Willson and B. J. Roman, "The Future of Lithography: SEMATECH Litho Forum 2008," *ACS Nano*, vol. 2, no. 7, pp. 1323–1328, Jul. 2008.

[8] C. Ngo and C. Rosilio, "Lithography for semiconductor technology," *Nucl. Instruments Methods Phys. Res. Sect. B Beam Interact. with Mater. Atoms*, vol. 131, no. 1–4, pp. 22–29, 1997.

[9] S. Jones, "14nm 16nm 10nm and 7nm - What we know now," 2017. [Online]. Available: https://www.semiwiki.com. [Accessed: 02-Aug-2017].

[10] P. F. Nealey, E. W. Edwards, M. Muller, M. P. Stoykovich, H. H. Solak, and J. J. de Pablo, "Self-assembling resists for nanolithography," in *IEEE InternationalElectron Devices Meeting, 2005. IEDM Technical Digest.*, 2005, vol. 0, no. 11, pp. 356–359.

[11] C. Park, J. Yoon, and E. L. Thomas, "Enabling nanotechnology with self assembled block copolymer patterns," *Polymer (Guildf).*, vol. 44, no. 22, pp. 6725–6760, Oct. 2003.

[12] Y. Xia and G. M. Whitesides, "Soft Lithography," *Angew. Chemie Int. Ed.*, vol. 37, no. 5, pp. 550–575, Mar. 1998.

[13] International Technology Roadmap for Semiconductors (ITRS), "Lithography Chapter," 2011.

[14] J. A. Liddle and G. M. Gallatin, "Lithography, metrology and nanomanufacturing.," *Nanoscale*, vol. 3, pp. 2679–2688, 2011.

[15] T. Yamaguchi and H. Yamaguchi, "Block copolymer lithography toward 16-nm-technology nodes and beyond," *NTT Tech. Rev.*, vol. 4, no. 11, pp. 17–24, 2006.

[16] D. J. C. Herr, "Directed block copolymer self-assembly for nanoelectronics fabrication," *J. Mater. Res.*, vol. 26, no. 2, pp. 122–139, 2011.

[17] P. Xie, H. Ren, A. Nainani, H. Dai, C. Bencher, and C. Ngai, "Understanding device impact of line edge/width roughness in frequency domain," in *Proc. SPIE*, 2013, vol. 8684, p. 86840J.

[18] M. C. Smayling, “Lithography alternatives meet design style reality: How do they ‘line’ up?,” in *Proc. of SPIE*, 2016, vol. 9777, p. 977702.

[19] Y. Kuwahara, S. Kawakami, M. Kubota, K. Matsunaga, K. Nafus, P. Foubert, and M. Mao, “EUV process establishment through litho and etch for N7 node,” in *Proc. of SPIE*, 2016, vol. 9776, p. 97760C.

[20] C. Montgomery, J. S. Chun, Y.-J. Fan, S.-H. Jen, M. Neisser, K. D. Cummings, W. Montgomery, T. Saito, L. Huli, D. Hetzer, H. Matsumoto, A. Metz, and V. Rastogi, “Evaluation of novel processing approaches to improve extreme ultraviolet (EUV) photoresist pattern quality,” vol. 9425, p. 942526, 2015.

[21] T. Watanabe and T. Harada, “EUVL Research Activity at Center for EUV Lithography,” *J. Photopolym. Sci. Technol.*, vol. 29, no. 5, pp. 737–744, 2016.

[22] P. Brandt, C. Tranquillin, M. Wieland, S. Bayle, M. Milléquant, and G. Renault, “Alternative stitching method for massively parallel e-beam lithography,” in *Proc. of SPIE*, 2015, vol. 9423, p. 942312.

[23] A. S. Gangnaik, Y. M. Georgiev, and J. D. Holmes, “New Generation Electron Beam Resists: A Review,” *Chem. Mater.*, vol. 29, no. 5, pp. 1898–1917, Mar. 2017.

[24] M. Hatano, K. Kobayashi, H. Kashiwagi, H. Tokue, T. Kono, N. Tetsuro, E. H. Choi, and W. Jung, “NIL defect performance toward high volume mass production,” in *Proc. of SPIE*, 2016, vol. 9777, p. 97770B.

[25] M. W. Thesen, M. Rumler, F. Schlachter, S. Grützner, C. Moormann, M. Rommel, D. Nees, S. Ruttloff, S. Pfirrmann, M. Vogler, A. Schleunitz, and G. Grützner, “Enabling large area and high throughput roll-to-roll NIL by novel inkjetable and photo-curable NIL resists,” in *Proc. of SPIE*, 2014, vol. 9049, p. 90490H.

[26] C. J. Hawker, T. P, and P. Thomas, “Block Copolymer Lithography : Merging ‘ Bottom- Up ’ with ‘ Top- Down ’ Processes,” *MRS Bull.*, vol. 30, no. December, pp. 952–966, 2005.

[27] J. Bang, U. Jeong, D. Y. Ryu, T. P. Russell, and C. J Hawker, “Block copolymer nanolithography: Translation of molecular level control to nanoscale patterns,” *Adv. Mater.*, vol. 21, no. 47, pp. 4769–4792, 2009.

[28] R. A. Farrell, T. G. Fitzgerald, D. Borah, J. D. Holmes, and M. A. Morris, “Chemical Interactions and Their Role in the Microphase Separation of Block Copolymer Thin Films,” *Int. J. Mol. Sci.*, vol. 10, no. 9, pp. 3671–3712, Aug. 2009.

[29] G. M. Whitesides, “Self-Assembly at All Scales,” *Science*, vol. 295, no. 5564, pp. 2418–2421, Mar. 2002.

[30] I. W. Hamley, “Nanotechnology with Soft Materials,” *Angew. Chemie Int. Ed.*, vol. 42, no. 15, pp. 1692–1712, Apr. 2003.

[31] International Technology Roadmap for Semiconductors (ITRS), “Emerging Research Materials Chaper,” 2011.

[32] M. A. Morris, “Directed self-assembly of block copolymers for nanocircuitry fabrication,” *Microelectron. Eng.*, vol. 132, pp. 207–217, 2015.

[33] A.-V. Ruzette and L. Leibler, “Block copolymers in tomorrow’s plastics,” *Nat. Mater.*, vol. 4, no. 1, pp. 19–31, Jan. 2005.

[34] R. A. Segalman, “Patterning with block copolymer thin films,” *Mater. Sci. Eng. R Reports*, vol. 48, no. 6, pp. 191–226, Mar. 2005.

[35] F. S. BATES, “Polymer-Polymer Phase Behavior,” *Science (80-.).*, vol. 251, no. 4996, pp. 898–905, Feb. 1991.

[36] S. B. Darling, “Mechanism for hierarchical self-assembly of nanoparticles on scaffolds derived from block copolymers,” *Surf. Sci.*, vol. 601, no. 13, pp. 2555–2561, 2007.

[37] M. C. Orilall and U. Wiesner, “Block copolymer based composition and morphology control in nanostructured hybrid materials for energy conversion and storage: solar cells, batteries, and fuel cells.,” *Chem. Soc. Rev.*, vol. 40, no. 2, pp. 520–535, 2011.

[38] R. Limary and P. F. Green, “Block Copolymer Thin Films Above and Below the Order-Disorder Transition Temperature,” *MRS Proc.*, vol. 629, p. FF1.5, Feb. 2000.

[39] S. H. Kim, M. J. Misner, and T. P. Russell, “Solvent-induced ordering in thin film diblock copolymer/homopolymer mixtures,” *Adv. Mater.*, vol. 16, no. 23–24, pp. 2119–2123, Dec. 2004.

[40] S. H. Kim, M. J. Misner, and T. P. Russell, “Controlling orientation and order in block copolymer thin films,” *Adv. Mater.*, vol. 20, no. 24, pp. 4851–4856, 2008.

[41] B. Kim, S.-K. W. K. W. Hong, S. Park, J. Xu, S.-K. W. K. W. Hong, and T. P. Russell, “Phase transition behavior in thin films of block copolymers by use of immiscible solvent vapors,” *Soft Matter*, vol. 7, no. 2, pp. 443–447, 2011.

[42] J. Zhao, S. Jiang, X. Ji, L. An, and B. Jiang, “Study of the time evolution of the surface morphology of thin asymmetric diblock copolymer films under solvent vapor,” *Polymer (Guildf).*, vol. 46, no. 17, pp. 6513–6521, Aug. 2005.

[43] M. W. Matsen and M. Schick, “Stable and unstable phases of a diblock copolymer melt,” *Phys. Rev. Lett.*, vol. 72, no. 16, pp. 2660–2663, Apr. 1994.

[44] V. Castelletto and I. W. Hamley, “Morphologies of block copolymer melts,” *Curr. Opin. Solid State Mater. Sci.*, vol. 8, no. 6, pp. 426–438, 2004.

[45] S. Krause, “Polymer-polymer miscibility,” *Pure Appl. Chem.*, vol. 58, no. 12, pp. 1553–1560, Jan. 1986.

[46] J. Burke, “Solubility Parameters: Theory and Application,” in *The American Institute for Conservation Book and Paper Group Annual*, vol. 3, 1984, pp. 13–58.

[47] H. Chu, “Morphologies of strongly segregated diblock copolymers,” *Science (80-.).*, vol. 36, no. 8, pp. 1569–1575, 1995.

[48] J. K. Kim, J. I. Lee, and D. H. Lee, “Self-assembled block copolymers: Bulk to thin film,” *Macromol. Res.*, vol. 16, no. 4, pp. 267–292, 2008.

[49] T. Xu, H.-C. Kim, J. DeRouchey, C. Seney, C. Levesque, P. Martin, C. M. Stafford, and T. P. Russell, “The influence of molecular weight on nanoporous polymer films,” *Polymer (Guildf).*, vol. 42, no. 21, pp. 9091–

9095, 2001.

[50] P. F. Green and R. Limary, “Block copolymer thin films: pattern formation and phase behavior,” *Adv. Colloid Interface Sci.*, vol. 94, no. 1–3, pp. 53–81, Nov. 2001.

[51] M. J. Fasolka and A. M. Mayes, “Block Copolymer Thin Films: Physics and Applications,” *Annu. Rev. Mater. Res.*, vol. 31, no. 1, pp. 323–355, Aug. 2001.

[52] R. Magerle and G. Krausch, “Nanostructured Thin Films via Self-Assembly of Block Copolymers,” *Adv. Mater.*, vol. 14, no. 21, pp. 1579–1583, 2002.

[53] D. Y. Kwok and a. W. Neumann, *Contact angle measurement and contact angle interpretation*, vol. 81, no. 3. 1999.

[54] V. Kapaklis, S. Grammatikopoulos, R. Sordan, A. Miranda, F. Traversi, H. von Känel, D. Trachylis, P. Poulopoulos, and C. Politis, “Nanolithographic templates using diblock copolymer films on chemically heterogeneous substrates.,” *J. Nanosci. Nanotechnol.*, vol. 10, no. 9, pp. 6056–6061, 2010.

[55] T. P. Russell, G. Coulon, V. R. Deline, and D. C. Miller, “Characteristics of the surface-induced orientation for symmetric diblock PS/PMMA copolymers,” *Macromolecules*, vol. 22, no. 12, pp. 4600–4606, Dec. 1989.

[56] P. Mansky, “Controlling Polymer-Surface Interactions with Random Copolymer Brushes,” *Science (80-.).*, vol. 275, no. 5305, pp. 1458–1460, Mar. 1997.

[57] J. I. Lee, S. H. Cho, S. M. Park, J. K. Kim, J. K. Kim, J. W. Yu, Y. C. Kim, and T. P. Russell, “Highly aligned ultrahigh density arrays of conducting polymer nanorods using block copolymer templates,” *Nano Lett.*, vol. 8, no. 8, pp. 2315–2320, 2008.

[58] I. In, Y.-H. H. La, S.-M. M. Park, P. F. Nealey, and P. Gopalan, “Side-chain-grafted random copolymer brushes as neutral surfaces for controlling the orientation of block copolymer microdomains in thin films,” *Langmuir*, vol. 22, no. 18, pp. 7855–7860, Aug. 2006.

[59] Y. S. Jung and C. a Ross, “Orientation-Controlled Self-Assembled Nanolithography Using a Polystyrene−Polydimethylsiloxane Block Copolymer,” *Nano Lett.*, vol. 7, no. 7, pp. 2046–2050, Jul. 2007.

[60] Y. S. Jung, J. B. Chang, E. Verploegen, K. K. Berggren, and C. A. Ross, “A path to ultranarrow patterns using self-assembled lithography,” *Nano Lett.*, vol. 10, no. 3, pp. 1000–1005, 2010.

[61] L. J. T. Landherr, C. Cohen, P. Agarwal, and L. A. Archer, “Interfacial friction and adhesion of polymer brushes,” *Langmuir*, vol. 27, no. 15, pp. 9387–9395, 2011.

[62] A. Oláh, H. Hillborg, G. J. Vancso, A. Olah, H. Hillborg, and G. J. Vancso, “Hydrophobic recovery of UV/ozone treated poly(dimethylsiloxane): Adhesion studies by contact mechanics and mechanism of surface modification,” *Appl. Surf. Sci.*, vol. 239, no. 3–4, pp. 410–423, Jan. 2005.

[63] B. Bergues, J. Lekki, A. Budkowski, P. Cyganik, M. Lekka, A. Bernasik, J. Rysz, and Z. Postawa, “Phase decomposition in polymer blend films cast on homogeneous substrates modified by self-assembled monolayers,” *Vacuum*,

vol. 63, no. 1–2, pp. 297–305, Jul. 2001.

[64] N. Herzer, C. Haensch, S. Hoeppener, and U. S. Schubert, "Orthogonal functionalization of silicon substrates using self-assembled monolayers," *Langmuir*, vol. 26, no. 11, pp. 8358–8365, 2010.

[65] A. Niemz, K. Bandyopadhyay, E. Tan, K. Cha, and S. M. Baker, "Fabrication of nanoporous templates from diblock copolymer thin films on alkylchlorosilane-neutralized surfaces," *Langmuir*, vol. 22, no. 26, pp. 11092–11096, 2006.

[66] D.-H. Park, "The fabrication of thin films with nanopores and nanogrooves from block copolymer thin films on the neutral surface of self-assembled monolayers," *Nanotechnology*, vol. 18, p. 355304, 2007.

[67] R. A. Segalman, K. E. Schaefer, G. H. Fredrickson, E. J. Kramer, and S. Magonov, "Topographic templating of islands and holes in highly asymmetric block copolymer films," *Macromolecules*, vol. 36, no. 12, pp. 4498–4506, 2003.

[68] A. Knoll, A. Horvat, K. S. Lyakhova, G. Krausch, G. J. A. Sevink, A. V. Zvelindovsky, and R. Magerle, "Phase behavior in thin films of cylinder-forming block copolymers," *Phys. Rev. Lett.*, vol. 89, no. 3, pp. 355011–355014, 2002.

[69] R. A. Farrell, E. R. Hosler, G. M. Schmid, J. Xu, M. E. Preil, V. Rastogi, N. Mohanty, K. Kumar, M. J. Cicoria, D. R. Hetzer, and A. DeVilliers, "Manufacturability considerations for DSA," in *Proc. of SPIE*, 2014, vol. 9051, p. 90510Z.

[70] C. T. Black, "Self-aligned self assembly of multi-nanowire silicon field effect transistors," *Appl. Phys. Lett.*, vol. 87, no. 16, pp. 1–3, 2005.

[71] D. Borah, S. Rassapa, M. T. Shaw, R. G. Hobbs, N. Petkov, M. Schmidt, J. D. Holmes, and M. a. Morris, "Directed self-assembly of PS-b-PMMA block copolymer using HSQ lines for translational alignment," *J. Mater. Chem. C*, vol. 1, no. 6, p. 1192, 2013.

[72] D. Borah, S. Rasappa, M. Salaun, M. Zellsman, O. Lorret, G. Liontos, K. Ntetsikas, A. Avgeropoulos, and M. A. Morris, "Soft Graphoepitaxy for Large Area Directed Self-Assembly of Polystyrene-block-Poly(dimethylsiloxane) Block Copolymer on Nanopatterned POSS Substrates Fabricated by Nanoimprint Lithography," *Adv. Funct. Mater.*, pp. 3425–3432, 2015.

[73] R. Segalman, H. Yokoyama, and E. J. Kramer, "Graphoepitaxy of spherical block copolymer films," *Adv. Mater.*, vol. 13, no. 15, pp. 1152–1155, 2001.

[74] J. Zhang, X. Yu, P. Yang, J. Peng, C. Luo, W. Huang, and Y. Han, "Microphase separation of block copolymer thin films.," *Macromol. Rapid Commun.*, vol. 31, no. 7, pp. 591–608, 2010.

[75] D. Borah, C. D. Simao, R. Senthamaraikannan, S. Rasappa, A. Francone, O. Lorret, M. Salaun, B. Kosmala, N. Kehagias, M. Zelsmann, C. M. Sotomayor-Torres, and M. A. Morris, "Soft-graphoepitaxy using nanoimprinted polyhedral oligomeric silsesquioxane substrates for the directed self-Assembly of PS-b-PDMS," *Eur. Polym. J.*, vol. 49, no. 11, pp. 3512–3521, 2013.

[76] Y. S. Jung and C. A. Ross, "Orientation-controlled self-assembled nanolithography using a polystyrene - polydimethylsiloxane block copolymer," *Nano Lett.*, vol. 7, no. 7, pp. 2046–2050, 2007.

[77] C. T. Black, "Polymer self-assembly as a novel extension to optical lithography," *ACS Nano*, vol. 1, no. 3, pp. 147–150, 2007.

[78] I. W. Hamley, "Ordering in thin films of block copolymers: Fundamentals to potential applications," *Prog. Polym. Sci.*, vol. 34, no. 11, pp. 1161–1210, 2009.

[79] S. O. Kim, H. H. Solak, M. P. Stoykovich, N. J. Ferrier, J. J. De Pablo, and P. F. Nealey, "Epitaxial self-assembly of block copolymers on lithographically defined nanopatterned substrates.," *Nature*, vol. 424, no. 6947, pp. 411–4, 2003.

[80] M. P. Stoykovich, M. Muller, S. O. Kim, H. H. Solak, E. W. Edwards, J. J. de Pablo, and P. F. Nealey, "Directed assembly of block copolymer blends into nonregular device-oriented structures," *Science (80-.).*, vol. 308, no. 5727, pp. 1442–1446, 2005.

[81] E. W. Edwards, M. Müller, M. P. Stoykovich, H. H. Solak, J. J. De Pablo, and P. F. Nealey, "Dimensions and shapes of block copolymer domains assembled on lithographically defined chemically patterned substrates," *Macromolecules*, vol. 40, no. 1, pp. 90–96, 2007.

[82] C.-C. Liu, E. Han, M. S. Onses, C. J. Thode, S. Ji, P. Gopalan, and P. F. Nealey, "Fabrication of Lithographically Defined Chemically Patterned Polymer Brushes and Mats," *Macromolecules*, vol. 44, no. 7, pp. 1876–1885, Apr. 2011.

[83] R. Gronheid, P. Rincon Delgadillo, H. Pathangi, D. Van den Heuvel, D. Parnell, B. T. Chan, Y.-T. Lee, L. Van Look, Y. Cao, Y. Her, G. Lin, R. Harukawa, V. Nagaswami, L. D'Urzo, M. Somervell, and P. Nealey, "Defect reduction and defect stability in IMEC's 14nm half-pitch chemo-epitaxy DSA flow," *Proc. SPIE*, vol. 9049, no. Figure 1, p. 904905, 2014.

[84] T. F. Kuech and L. J. Mawst, "Nanofabrication of III–V semiconductors employing diblock copolymer lithography," *J. Phys. D. Appl. Phys.*, vol. 43, no. 18, p. 183001, 2010.

[85] X. Chevalier, C. Nicolet, R. Tiron, A. Gharbi, M. Argoud, J. Pradelles, M. Delalande, G. Cunge, G. Fleury, G. Hadziioannou, and C. Navarro, "Scaling-down lithographic dimensions with block-copolymer materials: 10-nm-sized features with poly(styrene)- block -poly(methylmethacrylate)," *J. Micro/Nanolithography, MEMS, MOEMS*, vol. 12, no. 3, p. 31102, 2013.

[86] D. Borah, M. T. Shaw, S. Rasappa, R. a Farrell, C. O'Mahony, C. M. Faulkner, M. Bosea, P. Gleeson, J. D. Holmes, and M. a Morris, "Plasma etch technologies for the development of ultra-small feature size transistor devices," *J. Phys. D. Appl. Phys.*, vol. 44, no. 17, p. 174012, May 2011.

[87] P. P. Barros, S. Barnola, A. Gharbi, M. Argoud, I. Servin, R. Tiron, X. Chevalier, C. Navarro, C. Nicolet, C. Lapeyre, C. Monget, and E. Martinez, "Etch challenges for DSA implementation in CMOS via patterning," in *Proc. of SPIE*, 2014, vol. 9054, p. 90540G.

[88] C. Cummins, A. Gangnaik, R. A. Kelly, D. Borah, J. O'Connell, N. Petkov,

Y. M. Georgiev, J. D. Holmes, and M. A. Morris, “Aligned silicon nanofins via the directed self-assembly of PS-b-P4VP block copolymer and metal oxide enhanced pattern transfer.,” *Nanoscale*, vol. 7, no. 15, pp. 6712–21, 2015.

[89] T. Ghoshal, R. Senthamaraikannan, M. T. Shaw, J. D. Holmes, and M. A. Morris, “Fabrication of ordered, large scale, horizontally-aligned si nanowire arrays based on an in situ hard mask block copolymer approach,” *Adv. Mater.*, vol. 26, no. 8, pp. 1207–1216, 2014.

[90] H. Jansen, H. Gardeniers, M. De Boer, M. Elwenspoek, and J. Fluitman, “A survey on the reactive ion etching of silicon in microtechnology,” *J. Micromechanics Microengineering*, vol. 6, no. 1, pp. 14–28, Mar. 1996.

[91] S. A. McAuley, H. Ashraf, L. Atabo, A. Chambers, S. Hall, J. Hopkins, and G. Nicholls, “Silicon micromachining using a high-density plasma source,” *J. Phys. D. Appl. Phys.*, vol. 34, no. 18, pp. 2769–2774, Sep. 2001.

[92] O. Lotty, S. Biswas, T. Ghoshal, C. Glynn, C. O’ Dwyer, N. Petkov, M. a. Morris, and J. D. Holmes, “Containing the catalyst: diameter controlled Ge nanowire growth,” *J. Mater. Chem. C*, vol. 1, no. 29, p. 4450, 2013.

[93] S. Garrett, V. Franco, T. Snowden, C. Redden, V. Warke, and M. G. Bakker, “Development of Strategies to Improvement Ordering and Perpendicular Alignment of Cylinder Phase Block Copolymers Used as Templates for Bit Patterned Media,” *Mater. Res. Soc. Symp. Proc.*, vol. 1032, pp. 3–8, 2008.

[94] S. Azlin-Hasim, M. C. Cruz-Romero, T. Ghoshal, M. A. Morris, E. Cummins, and J. P. Kerry, “Application of silver nanodots for potential use in antimicrobial packaging applications,” *Innov. Food Sci. Emerg. Technol.*, vol. 27, pp. 136–143, Feb. 2015.

[95] M. Aizawa and J. M. Buriak, “Block Copolymer Templated Chemistry for the Formation of Metallic Nanoparticle Arrays on Semiconductor Surfaces,” *Chem. Mater.*, vol. 19, no. 21, pp. 5090–5101, Oct. 2007.

[96] S. Huettner, J. M. Hodgkiss, M. Sommer, R. H. Friend, U. Steiner, and M. Thelakkat, “Morphology-Dependent Charge Photogeneration in Donor–Acceptor Block Copolymer Films Based on Poly(3-hexylthiophene)- block -Poly(perylene bisimide acrylate),” *J. Phys. Chem. B*, vol. 116, no. 33, pp. 10070–10078, Aug. 2012.

[97] S. B. Darling, “Block copolymers for photovoltaics,” *Energy Environ. Sci.*, vol. 2, no. 12, p. 1266, 2009.

Chapter 2

Cyclical “Flipping” of Orientation in Hexagonal Forming Polystyrene-b-Poly(ethylene Oxide)

2.1 Abstract

We studied the kinetics of nanopattern evolution in PS-*b*-PEO diblock copolymer thin films. Using scanning force microscopy, a highly unexpected cylindrical flipping of morphology from normal to parallel to the film plane was detected during solvent annealing of the film (with average thickness of 30 nm) at high vapour pressure. Using an *in-situ* time resolved light scattering device combined with an environmental cell enabled us to obtain kinetic information at different vapour pressures. The data indicated that there is a threshold value for the vapour pressure necessary for the structural transition. We propose a swelling and de-swelling mechanism for the orientation flipping of the morphology. The cyclic transition occurs faster in thick films (177 nm) where the mass uptake and solvent volume fraction is smaller and therefore the driving force for phase separation is higher. We induced a stronger segregation by confining the chains in graphoepitaxial patterned substrates. As expected, the cyclic transition occurred at higher rate. Our work is another step forward to understanding the structure evolution and also controlling the alignment of block copolymer nano-cylinders independently of thickness and external fields.

2.2 Introduction

Self-organized block copolymer systems have been shown to have a host of applications [1], [2] most notably in the fabrication of inorganic structures used in electronic, optoelectronic [3], [4] and magnetic devices [5]. Absolute and precise control of pattern orientation (i.e. to the surface plane) is central to their possible use and requires a profound understanding of phase behaviour [6] and structure evolution [2], [7], [8] during post annealing of the BCP films. In this work, we demonstrate that pattern orientation coupled to pattern alignment can be achieved for cylinder forming PS-*b*-PEO films. We also show highly unexpectedly cyclic transitions with anneal

time of the polymer structure between perpendicular and parallel arrangements of microphase separated cylinders in these films using *in-situ* time resolved light scattering data combined with ex-situ time evolution AFM experiments. This is the first time such observations have been reported. In particular, our work shows how orientation of the pattern can be determined independently of the initial film thickness, surface segregation effects, and “solvent fields” [9]–[14].

Microphase separation in BCP systems has emerged as potentially the most practical self-assembly technique for fabrication of ultra-small nanoelectronics circuitry. However, achieving long range ordered patterns of controlled orientation (to surface) and alignment (to an in-plane surface direction) is the key to the industrial development of this technology. To perfect pattern formation for application, a good understanding of structure formation is needed. Thermal and solvent annealing of thin film block copolymers affords a means to induce the ordered microphase separation of these systems and so deliver organized patterns for industrial applications [15]. Russell and co-workers have pioneered the use of solvent annealing to direct the orientation of cylindrical patterns at the substrate surface using the ‘solvent field’ generated by solvent evaporation [16]–[18]. This work, however, demonstrates that solvent annealing is a (poorly understood) dynamic process that may offer considerable advantages in terms of structural control. To this effect, the dynamics of pattern formation in thin films (30 nm and 177 nm) of cylinder forming PS-*b*-PEO exposed to toluene vapour are detailed herein.

2.3 Experimental

2.3.1 Materials

We used PS-*b*-PEO block copolymer purchased from Polymer Source Inc. with average molecular masses of blocks M_{PS} = 42 kg mol^{-1} and M_{PEO} = 11 kg mol^{-1} and polydispersity of 1.07. Thin and thick (30 and 177 nm) PS-*b*-PEO films were spun cast from HPLC toluene solution from Sigma-Aldrich onto bare and topographically patterned silicon substrates with 2 nm thick native oxide layer. The silicon substrates were provided and patterned by Intel using electron beam lithography technique.

2.3.2 Characterization

For solvent annealing, the films were placed inside individual screw cap bottles of 100 mL volume with a toluene reservoir and were placed in the oven. The saturated vapour pressure is a function of temperature only, which means that by changing the temperature we are able to change the vapour pressure inside the cell. The films were exposed to toluene at different nominal vapour pressures, 12.3 kPa (at 50 °C) and 3 kPa (at 12 °C) for different periods of time. Every 5-10 minutes one sample was removed from the oven. The samples were quenched at room temperature. The topographic and phase images of the films were recorded with a Park XE-100 AFM system in non-contact mode under ambient conditions using silicon microcantilever probe tips with a force constant of 42 N m^{-1} to study the structure evolution. Film thickness was measured by a Woollam spectroscopic ellipsometer M-2000U. *In-situ* time resolved light scattering experiments were performed in a custom made environmental cell (Figure 2.4) that was heated by heating tapes to prevent wall condensation. During the annealing, a laser beam (He-Ne, 633 nm) incident on the sample is reflected. The intensity of the incident and the reflected light is measured by

two photodiodes. The specular reflection (reflectivity) was collected for 40 minutes and the reflectivity-time data was analysed.

2.4 Results

2.4.1 Cyclic Transition

Evidence for structural orientation control and the highly unusual cyclical ‘flipping’ of orientation is shown in Figure 2.1. These films were solvent annealed at 50 °C with nominal saturated vapour pressure of toluene about 12.3 kPa. Although these effects occur over a range of temperatures, 50 °C was the optimum temperature to work with as significantly higher temperatures lead to severe de-wetting of the films and lower temperatures did not provide sufficient driving force for this transition to happen. AFM images were collected after removal from the vapour. The film initially forms micelle structures, see Figure 2.1a, as evident by the bright “hill” structures, due to the micellization of PS-*b*-PEO in solution [19]. This configuration is stable for approximately 35 minutes when small voids begin to appear, presumably due to micelle coalescence, Figure 2.1b. This period appears to represent solvent diffusion through the film. PS is a glassy polymer and in an appropriate organic solvent, case II diffusion takes place [20], [21]. Case II diffusion is characterised by solvent propagating through a glassy polymer with a well-defined front; ahead of the solvent front is solvent-poor and remains glassy, while behind the front, the polymer is solvent-rich and plasticized. It is this plasticization which lowers the glass transition temperature, T_g, giving the polymer chains enhanced mobility. It can be described by two factors, the impact of the solvent volume fraction on the diffusion coefficient, and the time required for the solvent to locally plasticise the glassy matrix. Due to the kinetics of plasticization, case II diffusion is distinguished by an initial linear uptake of solvent, before crossing into a $t^{1/2}$ regime, similar to Fickian diffusion, as the

polymer becomes saturated [22], [23]. This is a relatively slow process as the volume fraction of the solvent has to reach a critical value before the polymer chains can extend and relax. At this time a front forms and propagates in the film. After 40 minutes of exposure the chains are stretched enough for front propagation, mass uptake is large enough and the phase transition to a vertical cylindrical (i.e. PEO cylinders within a PS matrix) occurs (Figure 2.1c). Surprisingly, this structure is not the thermodynamically stable state of the final film structure. Once formed, it can be repeatedly transformed between a parallel and vertical orientation dependent on solvent anneal time. This is highly unusual as additional solvent exposure normally only refines the structure through defect annihilation. Figure 2.1 panels d-h represent the recycling of these cylindrical structures. It should be noted that the structures formed extend through the film and are not surface effects only. This can be proven by selective wet/dry etching which removes the PEO cylinders from the outermost surface to the substrate-polymer interface (See Appendix – Chapter 2, Figure S2.7.1-S2.7.3).

We suggest that this flipping process results directly from a solvent swelling and de-swelling process as the number of times this recycling occurs cannot be a result of continued uptake of solvent since the film cannot swell infinitely. As the solvent swells the film, the film reaches a critical thickness where a parallel arrangement is more thermodynamically favourable [12], [24] and the film reconstructs to that shown in Figure 2.1 panels f and h (note that Figure 2.1d represents an intermediate structure where both vertical and parallel arrangements are observed).

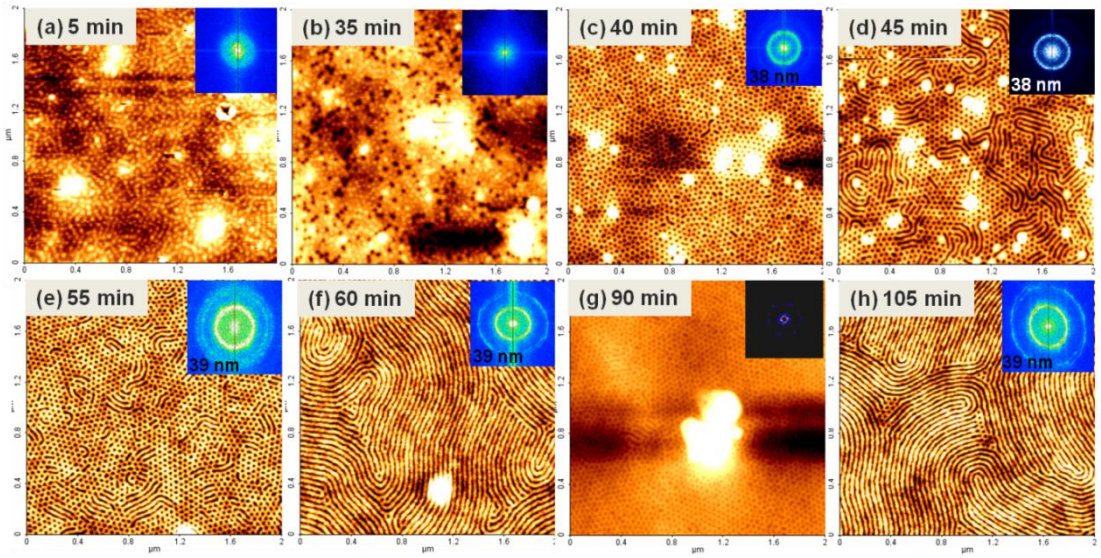


Figure 2.1. AFM topographic images showing repeated conversion of vertical and parallel orientation in a hexagonal forming PS-*b*-PEO film of 30 nm thick (a) after 5 min exposure to toluene at 12.3 kPa, (b) 35 min, (c) 40 min, (perpendicular arrangement), (d) mixed perpendicular and parallel arrangements, (e) 55 min, (f) 60 minutes, (g) 90 min, (h) 105 min. The images are 2x2 μm^2. The insets are FFT results, showing the pitch of about 39 nm.

It is suggested that the parallel cylinder orientation film continuously recycles into the vertical arrangement because this structure cannot maintain the volume of solvent absorbed and effectively ‘thins’ as excess solvent is released. This is schematically illustrated in Figure 2.2. The release of solvent might be associated with the surface energy differences of the film (surface composition is very different) or because of internal strain differences between the vertical and parallel arrangements. It is clear for this process to occur that both the vertical and parallel morphologies have very similar free energies of formation and small differences in conditions allow one structure to realise a different arrangement depending on e.g. thickness of the swelling film, solvent content etc. It should be noted that a recent GISAXS study of structure rearrangement [25] suggests lamellae PS-*b*-PB systems can go through de-swelling within a few minutes after exposure to toluene. However, this is solvent dependent as de-swelling in chloroform does not appear to occur for similar films [26].

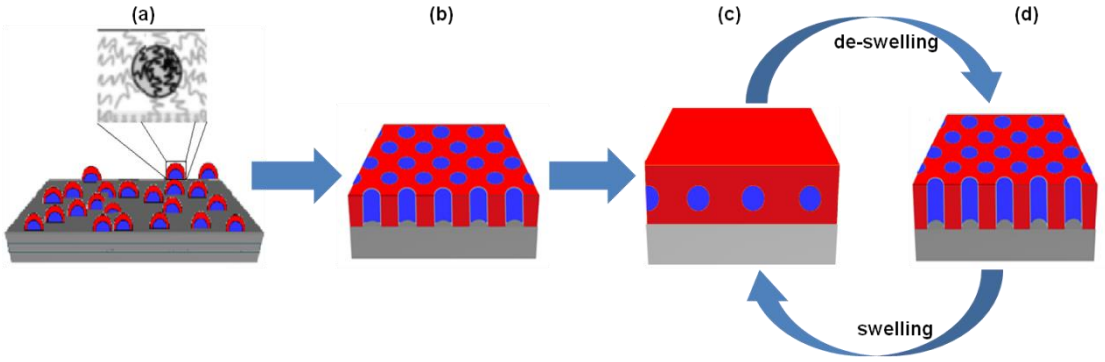


Figure 2.2. Schematic illustration of structural re-cycling in PS-*b*-PEO film (a) micelle formation after exposure to toluene, (b) perpendicular arrangement of the structure due to solvent uptake, (c) parallel orientation due to further swelling, (d) deswelling leads to flipping of the parallel to vertical alignment.

2.4.2 Thickness effect

This phenomenon was observed for all films prepared here and, for example, the cyclical nature of structural evolution was not affected by the initial film thickness. A thick film (177 nm) shows a similar behaviour to the thinner film but the rate of structural conversion is significantly quicker in the thicker film. In Figure 2.3b, after 20 minutes the perpendicular cylinders are already formed - for the thinner film it takes 40 minutes to reach this point (see Figure 2.1c). This is followed by a parallel orientation of cylinders (Figure 2.3c) which grow in length through the annealing process (see Figure 2.3c,d,f,h). The more rapid transition in thick films could be due to lower solvent uptake. By increasing the film thickness, the mass uptake and, therefore, the solvent volume fraction in the film decrease [27], leading to a strong Flory-Huggins interaction parameter between the polymer segments, which induces the driving force for the early phase separation (see Equation 2.1).

$$\chi_{eff} = \chi\,(1-\varphi_s) \qquad (2.1)$$

χ_{eff} and χ are the Flory-Huggins interaction parameters in presence and absence of the solvent. φ_s is the volume fraction of solvent.

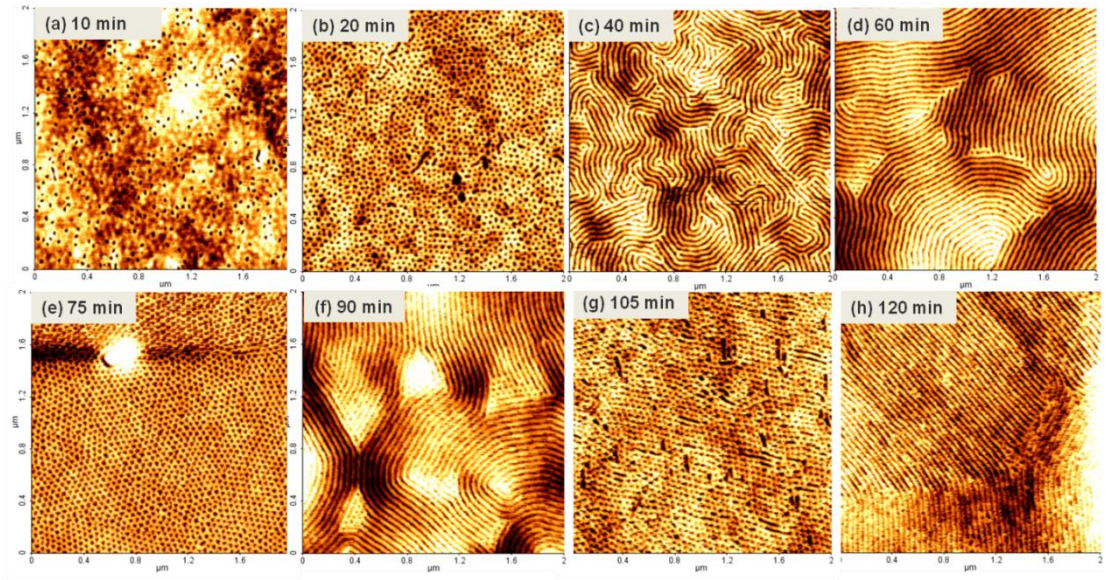


Figure 2.3. Cyclic transition in thick (177nm) PS-*b*-PEO films exposed to toluene for different annealing times. A transformation similar to thin film (shown in Figure 2.1) happens but at higher transition rate. A parallel structure is formed after 40 minutes (c) as opposed to 60 minutes in Figure 2.1f. The images are 2x2 μm^2.

2.4.3 *In-situ* time resolved light scattering

To validate the tentative model described here, we have performed an *in-situ* time resolved light scattering experiment in an environmental cell allowing samples to be annealed under different toluene pressures. This allowed the verification of the case II diffusion scenario (through the threshold value for vapour pressure) and monitoring of the solvent uptake through reflectivity. The vapour pressure in the reaction chamber was established by flowing nitrogen through a temperature controlled solvent reservoir so that the solvent vapour pressure was determined by the reservoir temperature. Figure 2.4 is the schematic diagram of the set up. To perform the experiment at 50 °C and to avoid condensation, most of the experimental set up parts including the bubbler, all tubes carrying the gas and the environmental chamber were wrapped in heating tapes (not shown here). The temperature was set 1°C above the annealing temperature at 51°C to avoid condensation and was controlled by a thermometer at different points. More details about this experimental set up can be found elsewhere [27]. Figure 2.5

shows reflectivity-time graphs during toluene exposure of PS-*b*-PEO film at saturated vapour pressure of 12.3 kPa (50 °C) and 3 kPa (at 12 °C). In both cases there is an immediate change in reflectivity after exposure to toluene. According to the Fresnel equation, reflectivity is a function of the thickness. Therefore the change in reflectivity is due to change in thickness and density. However, there is a clear difference between the reflectivity changes and the structure evolution at low and high vapour pressure (Figure 2.5).

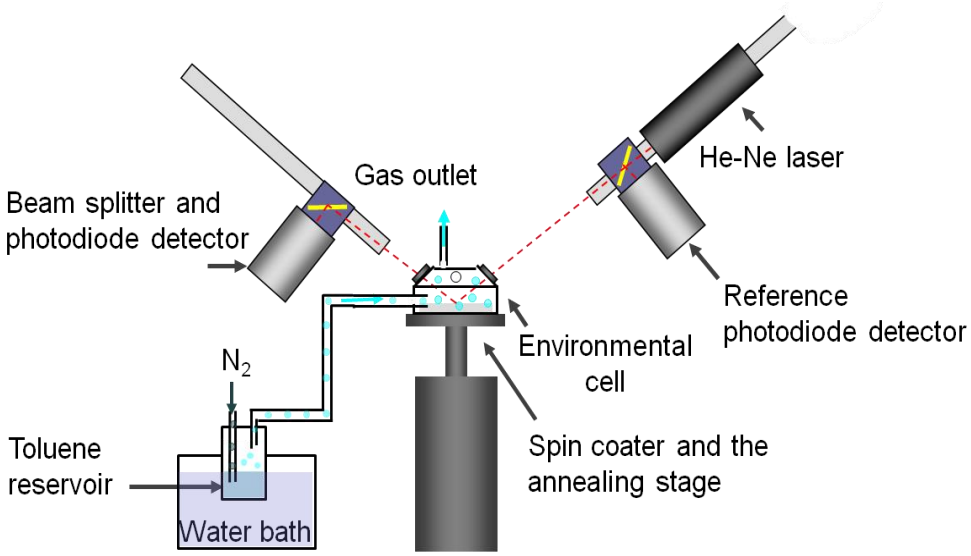


Figure 2.4. Schematic diagram showing the main components of the *in-situ* light scattering set up during solvent and thermal annealing in a custom-made environmental cell [27]. Nitrogen was blown into a toluene reservoir. The temperature of the reservoir was controlled in a water bath. The cell can be saturated with toluene with different nominal vapor pressures. The reflectivity- time data was recorded during the annealing. To avoid wall condensations, most components were wrapped in heating tapes (not shown here).

When the film is exposed to toluene at low vapour pressure (3 kPa), there is no structural change after 120 minutes (see the insets Figure 2.5b). This is because micelles form within 5 minutes of exposure and remain stable (see the lower inset in Figure 2.5). Also after the initial drop in reflectivity which is due to swelling and an increase in film thickness, there are no further pronounced changes (Figure 2.5b). It is

thought that at lower vapour pressure (3 kPa), the osmotic pressure that acts on a semi-permeable surface of a glassy polymer is not high enough to overcome the resistance exerted by immobilized chains in glassy PS. A contact angle measurement (α=74°) at a similar surface is consistent with the top layer consist of hydrophobic glassy PS. At high vapour pressure (12 kPa) there are 3 different regimes in Figure 2.5a. After an immediate change in the reflectivity due to a change in refractive index, a metastable equilibrium state is achieved for about 8 minutes. The small fringes are due to interference effects of the laser light from the top of the film and the polymer-substrate interface. After about 8 – 10 min there is a sharp but gradual decrease in the reflectivity before it plateaus. Between 30 and 40 min there is a discernible (but relatively small) increase in the reflectivity. The changes in the reflectivity observed are consistent with the AFM time evolution experiment shown in Figure 2.3. Three distinct reflectivity regimes in Figure 2.5 correspond to the formation of the initial three different patterns formed in PS-*b*-PEO films, as shown in the AFM images in Figure 2.3. The interval of 0-8 min represents the micelle structure, 8 – 25 minutes represents vertical cylinder formation and stability, whilst 25 – 35 minutes represent horizontal cylinder structure formation. The effect of the temperature is controversial in our experiment. While the higher temperature is expected to decrease the Flory Huggins interaction parameter and therefore reduce the driving force for separation, in our experiment the phase separation and the subsequent cyclic transition happens at higher temperature. One possible reason could be due to accessibility of the polymer chains to the solvent in the interior of the film. Low temperature does not provide enough pressure for the solvent to diffuse into the glassy layer easily. This can be clearly seen in Figure 2.5b in which the change in reflectivity (which reflects the change in thickness) is not apparent. On the other hand in Figure 2.5a, the high temperature provides enough

vapour pressure for diffusion of the vapour into the film and creates enough chain mobility for structure configuration. However, due to the complicated relationship of the reflectivity with thickness, it is not easy to predict the exact trend of thickness change during the swelling. But nevertheless, three distinctive regimes in reflectivity-time data (Figure 2.5a) and the coincident of time duration of each zone with structural change in AFM images back up our theory that the structural changes are related to thickness fluctuations.

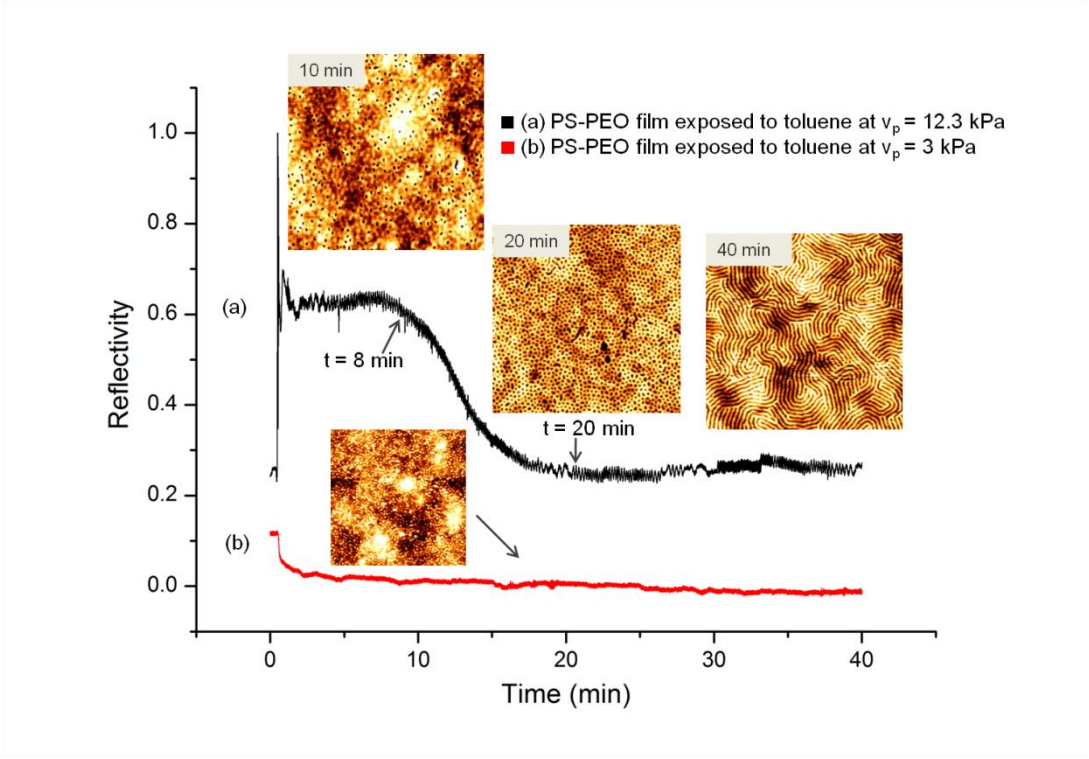


Figure 2.5. Specular reflectivity measured during the exposure of the PS-*b*-PEO film to toluene vapour (a) at 12.3kPa and (b) 3 kPa. The insets are AFM images during structure evolution. At high vapour pressure there are three different regimes correspond to different morphologies formed during that time. At low vapour pressure there is no change in reflectivity during the exposure and also no morphology evolution, suggesting a vapour pressure threshold is needed for the transition. The inset AFM images are 2x2 μm^2.

2.4.4 Graphoepitaxy

If solvent exposure is to be a practical (e.g. to define parallel nanowire structures) method of controlling nanopattern orientation, it is also necessary to combine the

solvent anneal methodology with a technique such as graphoepitaxy [5], [28]–[31] that facilitates pattern alignment (i.e. relative to an in-plane surface direction). These methods of directing the self-assembly process may impose additional boundary conditions which may prevent orientation control. Therefore, substrates were studied that were engineered with parallel channels of 400 nm width and 30 nm depth. Samples were prepared and processed similar to methodology described in Figure 2.1. The film thickness was sufficient to just fill the channels, i.e. about 30 nm (just enough to allow parallel cylinder morphologies) and the films demonstrated that orientation control coupled to directed alignment of both vertical and parallel pattern orientations could be achieved (Figure 2.6).

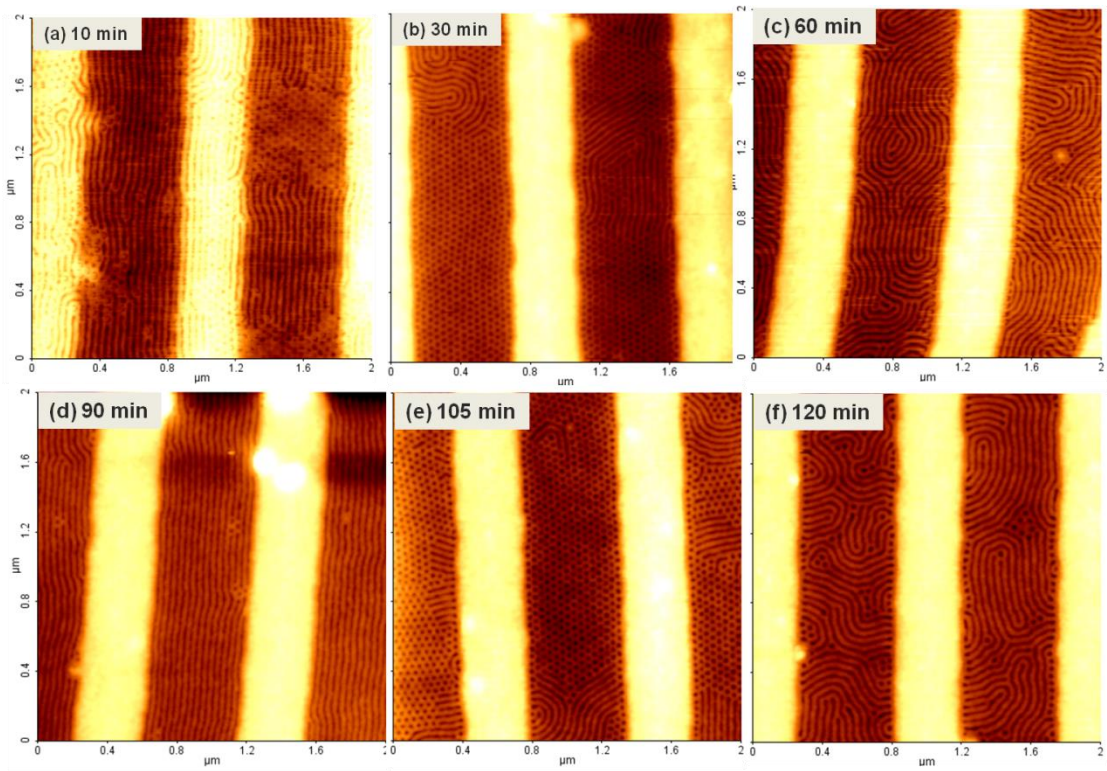


Figure 2.6. The effect of graphoepitaxy on cyclic transition. (a) The parallel lines form quickly, within 10 min of exposure. Then the structure fluctuates between dotes and lines (b and c). It reaches the best parallel alignment after 90 min. (e) and (f) more transition of perpendicular and parallel rays of cylinder. The images are 2x2 μm^2.

Ordered pattern formation is very rapid (indeed little evidence of micelle formation was observed even prior to solvent annealing) and the first ordered phase observed is a parallel arrangement of cylinders. As can be seen in Figure 2.6, the morphology of the cylinder structure switches between parallel and perpendicular arrangements with time, but at a significantly faster rate than seen on flat substrates. The films also exhibit strong graphoepitaxial effects typical of the PS-*b*-PEO system [32], because PEO interacts strongly with a silicon surface due to its higher polarity compared to PS [33]. This could account for the faster kinetics as graphoepitaxy is mediated by the strong interaction of one component with the topography and so induces component segregation [34]. In strongly segregated block copolymers, the chains are more stretched and solvent uptake happens faster [26] thus explaining the faster kinetics for both microphase separation and structure cycling.

2.5 Conclusions

In summary, we have demonstrated continuous control of pattern structure and alignment through solvent exposure. We have investigated the nature of a cyclic transition observed in PS-*b*-PEO thin films during the solvent annealing process. The morphology fluctuates between perpendicular and parallel arrays of cylinders over time. *In-situ* light scattering measurements indicate that during solvent annealing, structure cycles occur according to the amount of solvent in the film. The data indicates that there is a minimum value for the vapour pressure and solvent volume fraction in the film necessary for the full structural transitions to occur. This can be related to a case II diffusion in which a critical value of solvent is needed for formation and propagation of the front through the film. The cyclic structural transitions occur faster in both thick and topographically confined films consistent with a mechanism where structural transitions are related to solvent volume uptake.

2.6 References

[1] I. W. Hamley, “Ordering in thin films of block copolymers: Fundamentals to potential applications,” *Prog. Polym. Sci.*, vol. 34, no. 11, pp. 1161–1210, 2009.

[2] L. Tsarkova, G. J. A. Sevink, and G. Krausch, “Nanopattern Evolution in Block Copolymer Films: Experiment, Simulations and Challenges,” in *Advances in Polymer Science*, no. May 2012, 2010, pp. 33–73.

[3] L. Qiang, Z. Ma, Z. Zheng, R. Yin, and W. Huang, “Novel Photo-Crosslinkable Light-Emitting Rod/Coil Copolymers: Underlying Facile Material for Fabricating Pixelated Displays,” *Macromol. Rapid Commun.*, vol. 27, no. 20, pp. 1779–1786, Oct. 2006.

[4] S. B. Darling, “Block copolymers for photovoltaics,” *Energy Environ. Sci.*, vol. 2, no. 12, p. 1266, 2009.

[5] S. Xiao, X. Yang, E. W. Edwards, Y.-H. La, and P. F. Nealey, “Graphoepitaxy of cylinder-forming block copolymers for use as templates to pattern magnetic metal dot arrays,” *Nanotechnology*, vol. 16, no. 7, pp. S324–S329, Jul. 2005.

[6] A. Knoll, A. Horvat, K. S. Lyakhova, G. Krausch, G. J. A. Sevink, A. V. Zvelindovsky, and R. Magerle, “Phase behavior in thin films of cylinder-forming block copolymers,” *Phys. Rev. Lett.*, vol. 89, no. 3, pp. 355011–355014, 2002.

[7] A. Knoll, K. S. Lyakhova, A. Horvat, G. Krausch, G. J. A. Sevink, A. V Zvelindovsky, and R. Magerle, “Direct imaging and mesoscale modelling of phase transitions in a nanostructured fluid,” *Nat. Mater.*, vol. 3, no. 12, pp. 886–891, Dec. 2004.

[8] Y. Wang, X. Hong, B. Liu, C. Ma, and C. Zhang, “Two-dimensional ordering in block copolymer monolayer thin films upon selective solvent annealing,” *Macromolecules*, vol. 41, no. 15, pp. 5799–5808, 2008.

[9] A. Knoll, R. Magerle, and G. Krausch, “Phase behavior in thin films of cylinder-forming ABA block copolymers: Experiments,” *J. Chem. Phys.*, vol. 120, no. 2, pp. 1105–1116, Jan. 2004.

[10] S. H. Anastasiadis, T. P. Russell, S. K. Satija, and C. F. Majkrzak, “Neutron

reflectivity studies of the surface-induced ordering of diblock copolymer films,” *Phys. Rev. Lett.*, vol. 62, no. 16, pp. 1852–1855, Apr. 1989.

[11] M. W. Matsen, “Self-assembly of block copolymers in thin films,” *Curr. Opin. Colloid Interface Sci.*, vol. 3, no. 1, pp. 40–47, 1998.

[12] I. W. Hamley, “Nanostructure fabrication using block copolymers,” *Nanotechnology*, vol. 14, no. 10, pp. R39–R54, Oct. 2003.

[13] M. J. Fasolka and A. M. Mayes, “Block Copolymer Thin Films: Physics and Applications,” *Annu. Rev. Mater. Res.*, vol. 31, no. 1, pp. 323–355, Aug. 2001.

[14] R. A. L. Jones, L. J. Norton, E. J. Kramer, F. S. Bates, and P. Wiltzius, “Surface-directed spinodal decomposition,” *Phys. Rev. Lett.*, vol. 66, no. 10, pp. 1326–1329, Mar. 1991.

[15] S. M. O’Driscoll, C. T. O’Mahony, R. A. Farrell, T. G. Fitzgerald, J. D. Holmes, and M. A. Morris, “Toroid formation in polystyrene-block-poly(4-vinyl pyridine) diblock copolymers: Combined substrate and solvent control,” *Chem. Phys. Lett.*, vol. 476, no. 1–3, pp. 65–68, 2009.

[16] S. H. Kim, M. J. Misner, T. Xu, M. Kimura, and T. P. Russell, “Highly oriented and ordered arrays from block copolymers via solvent evaporation,” *Adv. Mater.*, vol. 16, no. 3, pp. 226–231, 2004.

[17] H. Elbs, C. Drummer, V. Abetz, and G. Krausch, “Thin Film Morphologies of ABC Triblock Copolymers Prepared from Solution,” *Macromolecules*, vol. 35, no. 14, pp. 5570–5577, Jul. 2002.

[18] K. Fukunaga, H. Elbs, R. Magerle, and G. Krausch, “Large-Scale Alignment of ABC Block Copolymer Microdomains via Solvent Vapor Treatment,” *Macromolecules*, vol. 33, no. 3, pp. 947–953, Feb. 2000.

[19] G. Riess, “Micellization of block copolymers,” *Prog. Polym. Sci.*, vol. 28, no. 7, pp. 1107–1170, 2003.

[20] T. Alfrey, E. F. Gurnee, and W. G. Lloyd, “Diffusion in glassy polymers,” *J. Polym. Sci. Part C Polym. Symp.*, vol. 12, no. 1, pp. 249–261, Mar. 2007.

[21] N. . Thomas and A. . Windle, “A theory of case II diffusion,” *Polymer (Guildf).*, vol. 23, no. 4, pp. 529–542, Apr. 1982.

[22] G. Ross, “A Phenomenological Description of Case-I1 Diffusion in Polymeric

Materials .,” *Europhys. Lett.*, vol. 32, no. 5, pp. 391–396, 1995.

[23] M. Souche and D. Long, “Case-II diffusion and solvent-polymer films drying: A meso-scale model,” *Epl*, vol. 77, no. 4, 2007.

[24] A. Horvat, K. S. Lyakhova, G. J. A. Sevink, A. V. Zvelindovsky, and R. Magerle, “Phase behavior in thin films of cylinder-forming ABA block copolymers: Mesoscale modeling,” *J. Chem. Phys.*, vol. 120, no. 2, pp. 1117–1126, Jan. 2004.

[25] C. M. Papadakis, Z. Di, D. Posselt, and D.-M. Smilgies, “Structural Instabilities in Lamellar Diblock Copolymer Thin Films During Solvent Vapor Uptake,” *Langmuir*, vol. 24, no. 24, pp. 13815–13818, Dec. 2008.

[26] U. Zettl, A. Knoll, and L. Tsarkova, “Effect of Confinement on the Mesoscale and Macroscopic Swelling of Thin Block Copolymer Films,” *Langmuir*, vol. 26, no. 9, pp. 6610–6617, May 2010.

[27] P. Mokarian-Tabari, M. Geoghegan, J. R. Howse, S. Y. Heriot, R. L. Thompson, and R. A. L. Jones, “Quantitative evaluation of evaporation rate during spin-coating of polymer blend films: Control of film structure through defined-atmosphere solvent-casting,” *Eur. Phys. J. E*, vol. 33, no. 4, pp. 283–289, Dec. 2010.

[28] S. O. Kim, H. H. Solak, M. P. Stoykovich, N. J. Ferrier, J. J. De Pablo, and P. F. Nealey, “Epitaxial self-assembly of block copolymers on lithographically defined nanopatterned substrates.,” *Nature*, vol. 424, no. 6947, pp. 411–4, 2003.

[29] R. A. Segalman, H. Yokoyama, and E. J. Kramer, “Graphoepitaxy of spherical domain block copolymer films,” *Adv. Mater.*, vol. 13, no. 15, pp. 1152–1155, 2001.

[30] J. Y. Cheng, F. Zhang, H. I. Smith, G. J. Vancso, and C. A. Ross, “Pattern registration between spherical block-copolymer domains and topographical templates,” *Adv. Mater.*, vol. 18, no. 5, pp. 597–601, 2006.

[31] D. Sundrani, S. B. Darling, and S. J. Sibener, “Guiding Polymers to Perfection: Macroscopic Alignment of Nanoscale Domains,” *Nano Lett.*, vol. 4, no. 2, pp. 273–276, 2004.

[32] T. G. Fitzgerald, R. A. Farrell, S. O’Driscoll, C. T. O’Mahony, J. D. Holmes,

and M. A. Morris, “Orientation and Translational Control of PS-b-PEO/PS Thin Films via Solvent Annealing and Graphoepitaxy Techniques,” *e-Journal Surf. Sci. Nanotechnol.*, vol. 7, no. April, pp. 471–475, 2009.

[33] C. Neto, M. James, and A. M. Telford, “On the composition of the top layer of microphase separated thin PS-PEO films,” *Macromolecules*, vol. 42, no. 13, pp. 4801–4808, 2009.

[34] R. A. Farrell, T. G. Fitzgerald, D. Borah, J. D. Holmes, and M. A. Morris, “Chemical Interactions and Their Role in the Microphase Separation of Block Copolymer Thin Films,” *Int. J. Mol. Sci.*, vol. 10, no. 9, pp. 3671–3712, Aug. 2009.

2.7 Appendix

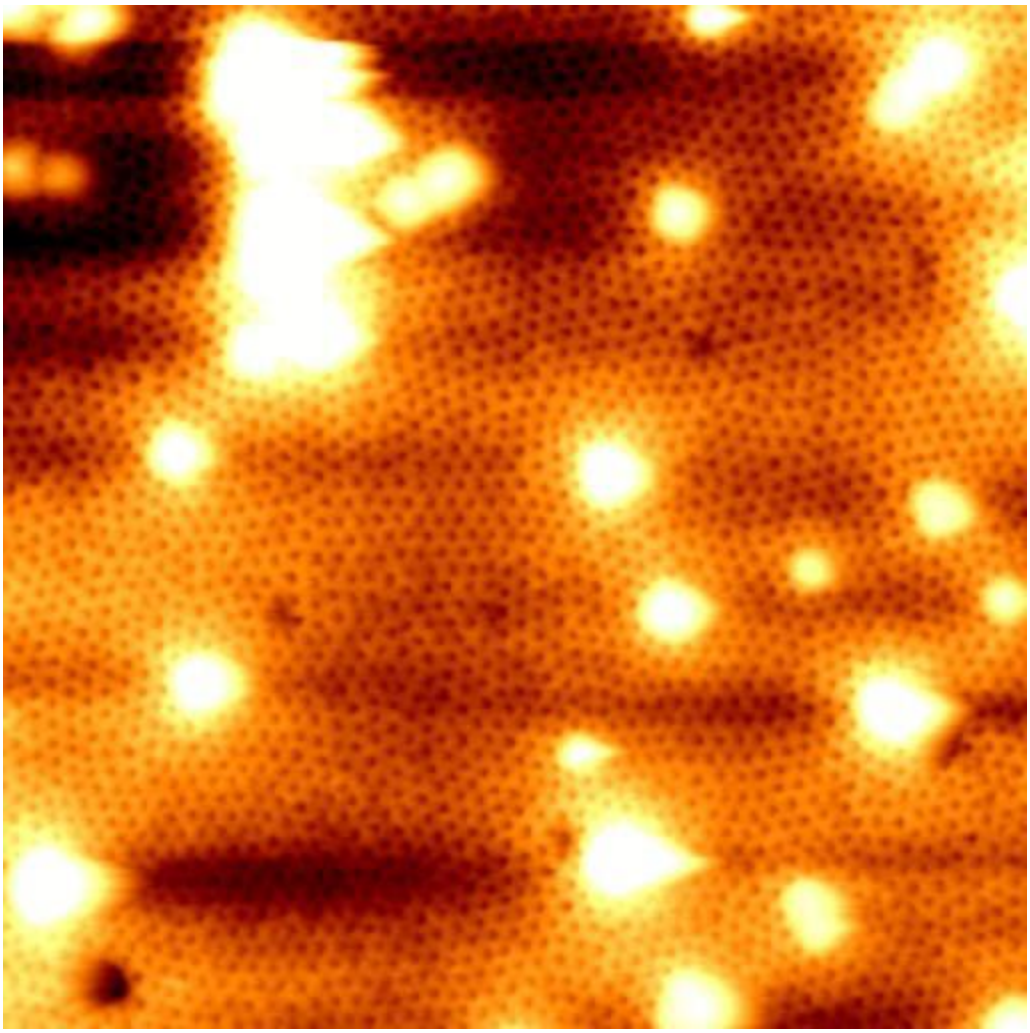


Figure S2.7.1. AFM topography image of as-cast PS-*b*-PEO film (30 nm). The image is 2x2 μm^2.

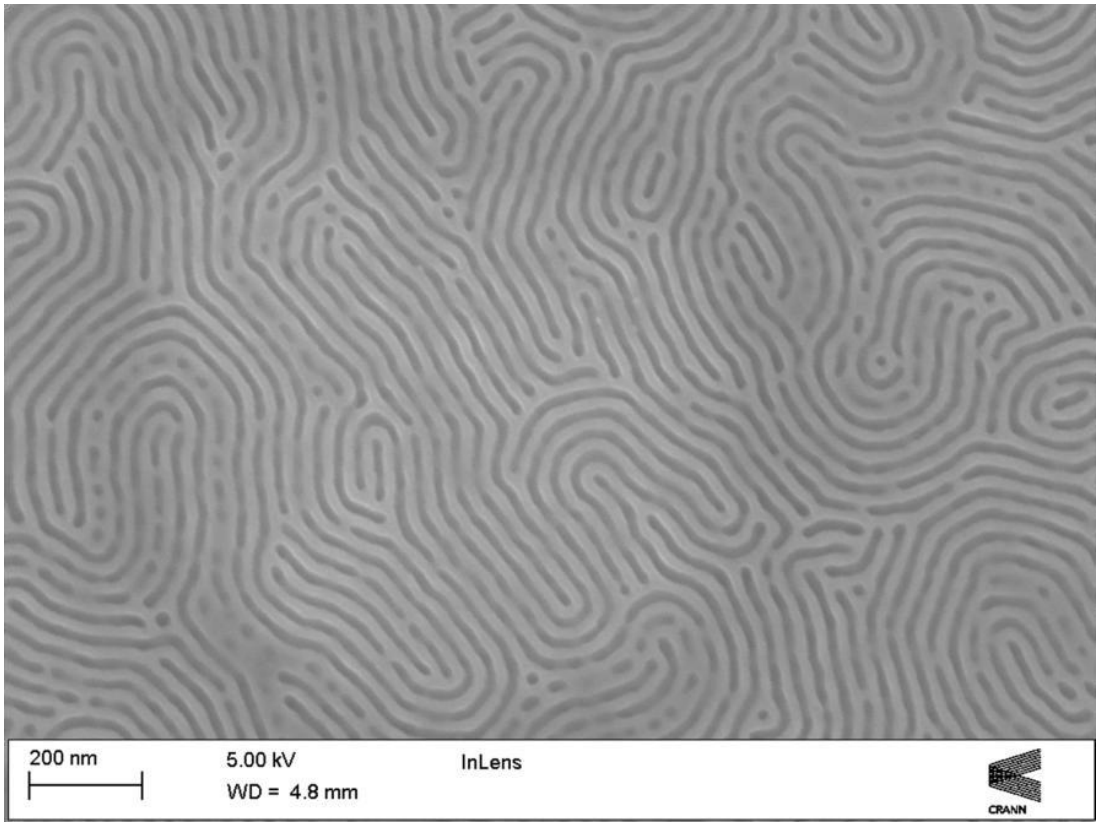


Figure S2.7.2. SEM image of nanowires fabricated by PS-*b*-PEO film. PEO lines have been removed by Ar/O_2 plasma dry etch. The remaining PS template has been pattern transferred with SF_6/CF_4 to a silicon substrate.

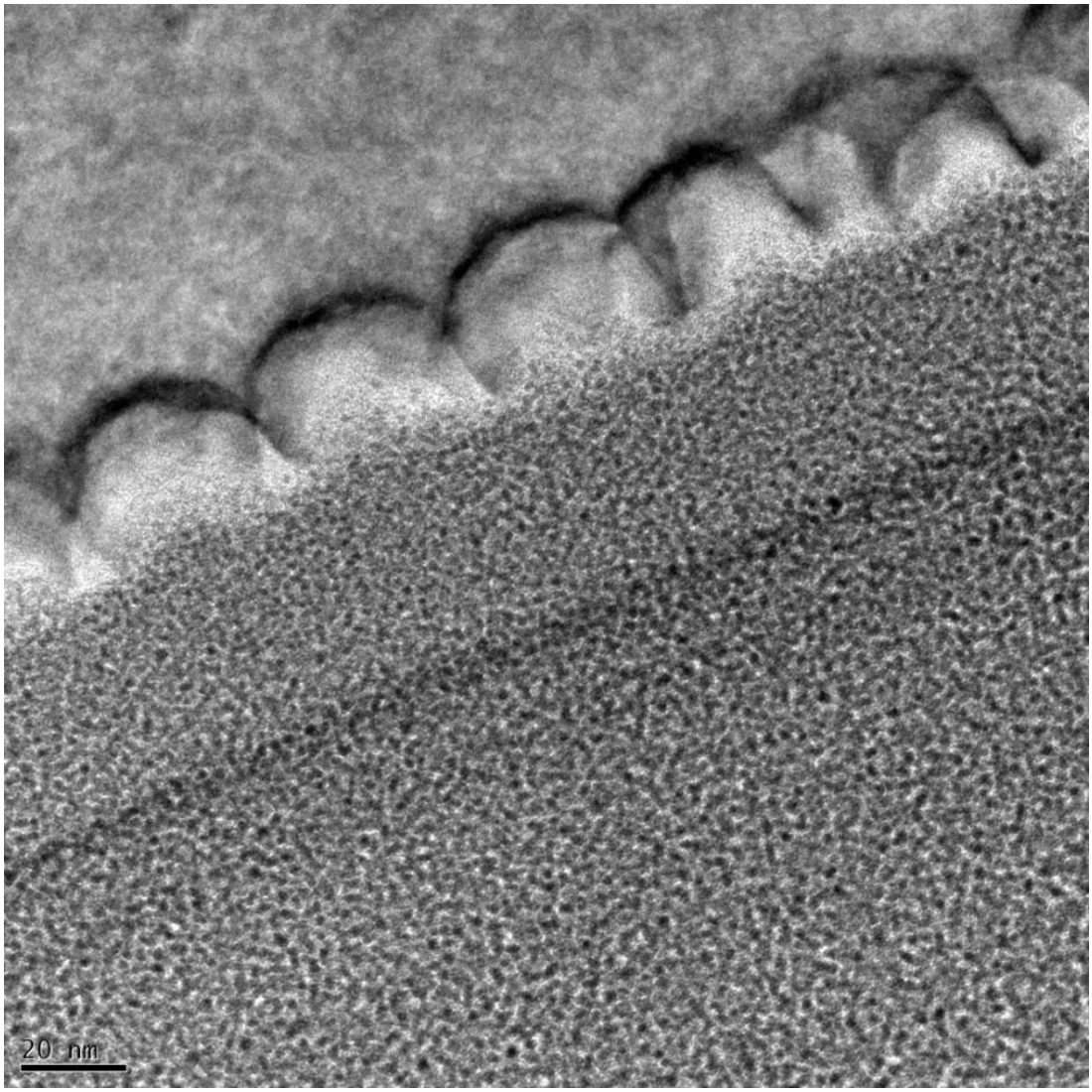


Figure S2.7.3. TEM cross section of PS-*b*-PEO dot patterns. PEO cylinders have been removed by Ar/O_2 plasma dry etch. The remaining PS template has been pattern transferred with SF_6/CF_4 to a silicon substrate. The image shows that the structures formed extend through the film and are not surface effects only.

Chapter 3

Brushless Microphase Separation of Lamellar Polystyrene-b-Poly(ethylene Oxide) Thin Films

3.1 Abstract

Creating perpendicular alignment in lamellar block copolymer systems has considerable industrial and commercial significance most importantly for generating nanowire structures in electronic devices. In general, these lamellar systems require careful interface engineering to obtain vertical orientation of the blocks. To avoid the strong preferential adsorption of one block to either the substrate or the polymer/air interface, the surface must be 'neutralised' by chemical brushes or external forces e.g. solvent fields. Reported here is a stepwise thermo/solvent annealing process allowing the formation of perpendicular domains of PS-*b*-PEO lamellar structures while avoiding brush or other surface modification. This BCP has a relatively small minimum feature size and can be used to generate substrate patterns for use in fabrication of nanowire electronic device structures.

3.2 Introduction

Microphase-separated BCP nanostructures are being heavily investigated mostly because of their potential application in the generation of nanoelectronic devices and other circuit elements. A major motivation of the research is in the possible development of ultra-small dimension substrate patterning without a need for expensive EUV lithography [1], [2]. BCPs that form lamellar structures are the most applicable here, as selective removal of one block generates a resist or template pattern [3], [4]. To date, efforts have centered on the use of PS-*b*-PMMA because of its compatibility with modern microelectronic fabrication techniques. Lamellar PS-*b*-PMMA with molecular weights less than 74 kg mol^{-1}, however, are limited by long vacuum annealing periods (in excess of 3 hours) for self-assembly [5], complex brush chemistry for orientation control [6], a relatively large minimum feature size [7] and

poor etch contrast [8], [9]. There is, therefore, a need to develop not only new BCPs but also new processing methodologies to avoid complex surface modifications.

Whilst self-assembly and controlling orientation in block copolymers have been widely investigated [10]–[16], studies related to PS-*b*-PEO thin films have been confined to asymmetric hexagonal, cylinder forming systems [12], [17]–[20]. Although the hexagonal systems can form line-like structures, there are no experimental reports, to the best of our knowledge, concerning the creation of perpendicular domains in lamellar PS-*b*-PEO films. Lamellar systems have advantages in lithographic applications because of their etchability [8]. Self-consistent mean field theory predicts that perpendicular block orientation is more favourable at neutral surfaces due to higher conformational freedom [21]. However, other factors such as surface roughness [22], [23], the differences in interfacial energy of the blocks with the surface [14], [24], [25], and incommensurability of the film thickness with the bulk value of copolymer lamellar period [14], [15], [21], [26] can also result in perpendicular orientation in lamellar systems. In this chapter, we introduce a simple stepwise thermo/solvent annealing process, which is a combination of thermal and solvent annealing to generate the perpendicular nanostructures in lamellar PS-*b*-PEO systems. In this method the perpendicular alignment of the blocks is facilitated without use of a polymer brush or any complex surface functionalisation chemistry.

3.3 Experimental

3.3.1 Polymers

Two symmetric PS-*b*-PEO diblock copolymers (labelled PS24-PEO24.5 and PS12.5-PEO14) with number average molecular weight ($M_{n,PS}$ = 24 kg mol^{-1} / $M_{n,PEO}$ = 24.5 kg mol^{-1}, PDI = 1.09, ($\boldsymbol{f_{PEO}^{v}} \cong 0.5$) and ($M_{n,PS}$ = 12.5 kg mol^{-1} / $M_{n,PEO}$ = 14 kg mol^{-1}, PDI = 1.09, ($\boldsymbol{f_{PEO}^{v}} \cong 0.52$) from Polymer Source were used to demonstrate the stepwise thermo/solvent annealing process for generating nanopatterns. The copolymers were used as bought and with no further modification. Thin films of PS-*b*-PEO were spin coated onto silicon wafers from 1 wt. % polymer solution in toluene (3000 rpm for 30 s). The properties of each diblock copolymer are summarised in Table 3.1.

Sample Code	$M_{n,PS}$ (kg mol^{-1})	$M_{n,PEO}$ (kg mol^{-1})	$\boldsymbol{f_{PEO}^{v}}$	$\boldsymbol{T_{PEO}^{g}}$ (°C)	$\boldsymbol{T_{PEO}^{m}}$ (°C)	$\boldsymbol{T_{PEO}^{c}}$ (°C)
PS24-PEO24.5	24	24.5	0.5	-65	63	43
PS12.5-PEO14	12.5	14	0.52	-48	56	36

Table 3.1. The properties of the copolrmers based on the data sheet. $\boldsymbol{f_{PEO}^{v}}$, $\boldsymbol{T_{PEO}^{g}}$, $\boldsymbol{T_{PEO}^{m}}$ and $\boldsymbol{T_{PEO}^{c}}$ are the volume fraction, glass transition, melting and crystallisation temparature of PEO, respectively.

3.3.2 Stepwise thermo/solvent Annealing

In the stepwise thermo/solvent annealing process the films of PS24-PEO24.5 were thermal annealed in the oven at 90 °C then cooled to 70 °C (above the melting point of PEO). The samples were then removed from the oven and placed in a 100 ml vessel with toluene and water reservoirs and returned to the oven at 68 °C. The samples were annealed at 46 °C (i.e. above the crystallisation temperature of PEO block) for two hours. The overall process is described graphically in Figure 3.1, which also describes the intention of each stage of the process. The same process was applied on thin films

of PS12.5-PEO14. However, the annealing temperatures at different steps were modified based on the melting and crystallisation temperature of PEO block in this system. More details are provided in section 3.4.

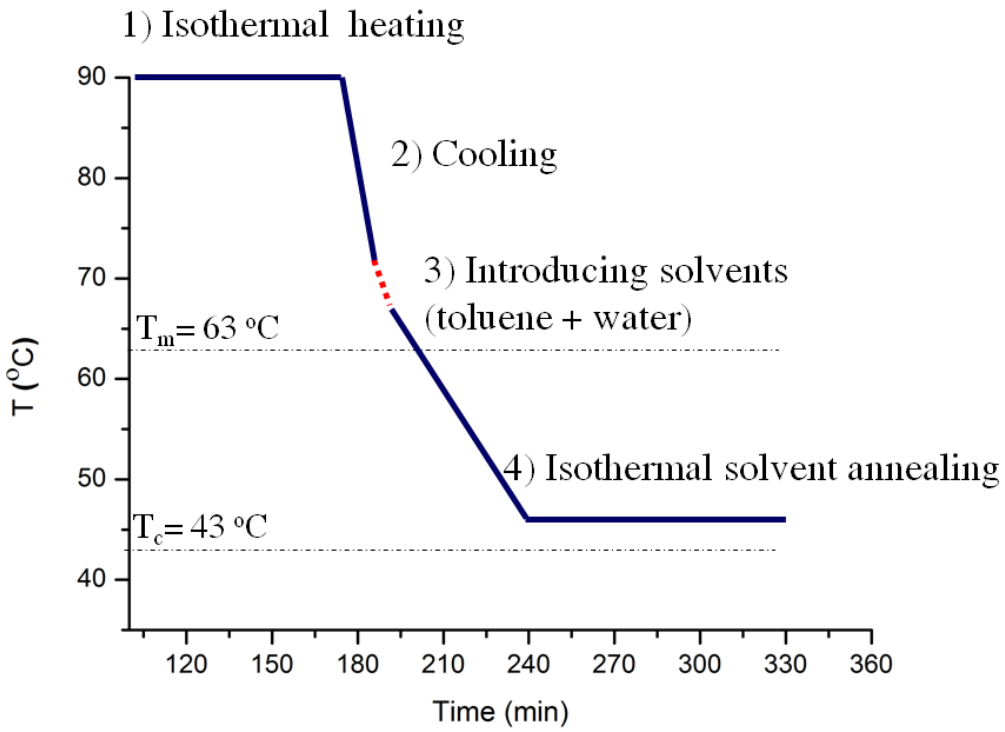


Figure 3.1. The 4 critical steps in stepwise thermo/solvent annealing of PS24-*b*-PEO24.5 film; (1) Isothermal annealing for 2-3 hours at 90 °C, (2) Cooling the film to 70 °C and removing from the oven, (3) putting the samples in the vial with toluene and water reservoir and returning the samples to the oven at 68 °C (above PEO melting point), (4) Solvent annealing the samples at 46 °C (above crystallization temperature of PEO). The black dotted lines show the melting and crystallization temperature of PEO.

3.3.3 Film characterisation

Atomic Force Microscopy (AFM). The topographic and phase images of the films were recorded with a Park XE-100 AFM system in non-contact mode under ambient conditions using silicon microcantilever probe tips with a force constant of 42 N m^{-1}.

Transmission Electron Microscopy (TEM). Site-selective cross sectional TEM sample preparation was performed using an Omniprobe lift-out on a dual-beam FEI

Strata 400 focused ion-beam (FIB). All TEM imaging was performed on a FEI Technai G20 LaB_6 operating at an accelerating voltage of 200 kV.

Scanning Electron Microscopy (SEM). SEM images were obtained using a high resolution field emission Zeiss Ultra Plus operating between 5 and 10 keV. For cross-sectional SEM image, the sample was cleaved with a diamond knife and mounted on a 90° cross section holder and tilted at various angles.

3.3.4 Etch and pattern transfer

Two different methods of wet and dry etching were carried out to remove PEO blocks selectively. For wet etch, the PS-*b*-PEO films on Si substrate were immersed in hydriodic acid (HI) at 60 °C for 5 days followed by rinsing with methanol and water and dried with nitrogen [27]. The dry etch was performed in an Oxford Instruments Plasmatech in RIE mode using a mixture of tetrafluoromethane (CF_4) and O_2 at the pressure of 20 mTorr. The remaining PS mask was pattern transferred to a silicon substrate using a combination of sulfur hexafluoride (SF_6) and octafluorocyclobutane (C_4F_8) gasses in an STS AOE Surface Technology Systems Advanced Oxide Etch inductively coupled plasma (ICP) etcher. The residual PS stripes after the pattern transfer were removed by O_2 plasma [8], [9]

3.4 Results and Discussion

3.4.1 Stepwise Annealing

In order to generate perpendicular lamellae, a range of thermal and solvent annealing steps, for example, in toluene, water, chloroform and tetrahydrofuran *etc.* (and mixtures thereof) were tested based on the asymmetric, cylinder forming systems [12], [19], [28]. No lateral phase separation was observed in the film, see Figure 3.2. The Flory-Huggins interaction parameter (χ) between PS and PEO at a given temperature (T) can be calculated using the equation reported by Zhu *et al.* [29], (χ = -7.05 x 10^{-3} + 21.3/T). Calculating the degree of polymerization (N), N = 860 for the PS24-PEO24.5 systems, and N = 479 for the PS12.5-PEO14 systems. In our experimental conditions (T = 20 - 100 °C) the phase segregation strength χN is larger than 10.50, therefore it is likely that the lamellae domains have formed parallel to the surface plane. This is consistent with the known strong affinity between the polar, hydrophilic PEO and the silicon substrate surface as well as the significantly lower surface energy of PS (σ_{PS} = 31 mN m^{-1} and σ_{PEO} = 43 mN m^{-1}).

Theoretical [21], [30] and experimental [22]–[24], [31]–[34] studies indicate that perpendicular orientation is achieved using a processing method that alters the interface chemistry (e.g., using polymer brushes). This also reduces the occurrence of break-out crystallisation, a phenomenon observed within miscible crystalline/rubbery BCPs, which results in the formation of large, irregular crystals, irrespective of the BCP composition [35], [36]. The latter point is important as PS-*b*-PEO is a semicrystalline BCP with the PEO being the crystalline block. Patterns form in these systems via two competing self-organizing mechanisms, [37]–[41] microphase separation and/or crystallization. Both these processes have common kinetically controlling parameters (i.e., temperature, pressure etc.) and changes in one parameter

can change the competitive balance of these mechanisms. In contrast to amorphous copolymers where thermodynamics defines the orientation of the lamellae, in semicrystalline polymers the morphology is dictated by kinetics of the crystallisation [42].

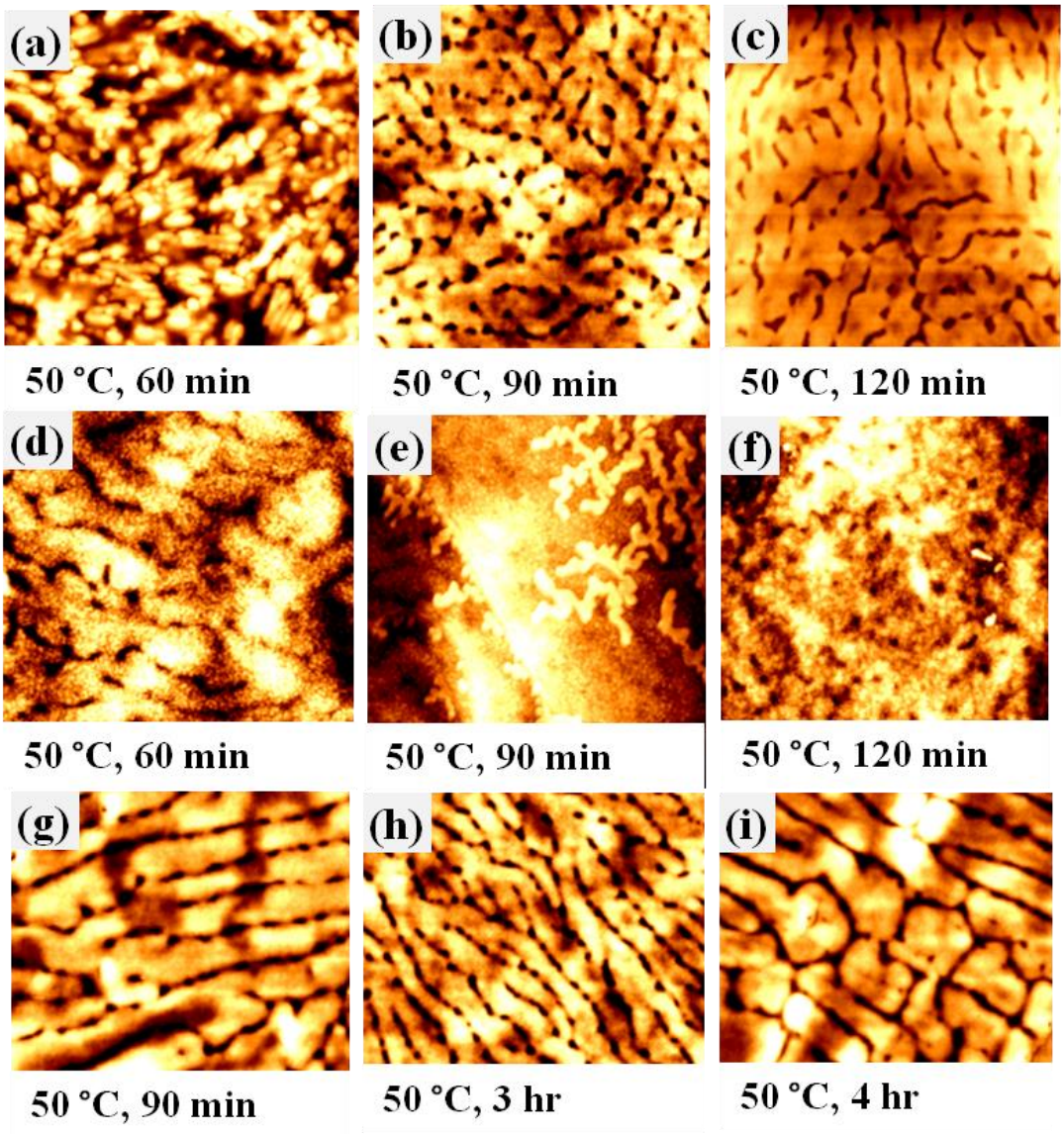


Figure 3.2. AFM topography images of of PS24-PEO24.5 films after conventional annealing at 50 °C in (a-c) toluene vapour, (d-f) chloroform vapour and (g-i) mixed toluene and water vapour atmosphere over different period of time. No microphase separation is observed on the top surface of the film.

Above the crystallization temperature (T_c) the incompatibility between the blocks provides enough driving force to facilitate microphase separation and the formation of

the lamellar morphologies. However, below the (T_c), crystallization will drive the formation of alternating layers of the polymer blocks. In the first step of the thermo/solvent annealing, samples are heated at 90 °C for 2-3 hours, which is above the melting temperature of PEO ($\boldsymbol{T_{PEO}^{m}}$ = 63 °C). High temperature makes the polymer chains highly mobile, allowing unfolding and stretching of the chains. Long annealing times encourages homogenous nucleation of PEO alignment. If the annealing time is short (in our experiment less than 2 hours), the structure evolution is dominated by the polymer-substrate interfaces [43], [44]. In Steps 2 and 3 of the thermo/solvent annealing process, the film was cooled to 70 °C and then removed from the oven and placed inside a screw cap bottle (100 ml) and placed in an oven at 68 °C, with a toluene and water reservoir. The temperature of the oven was set a few degrees above the melting point of PEO ($\boldsymbol{T_{PEO}^{m}}$ = 63 °C).

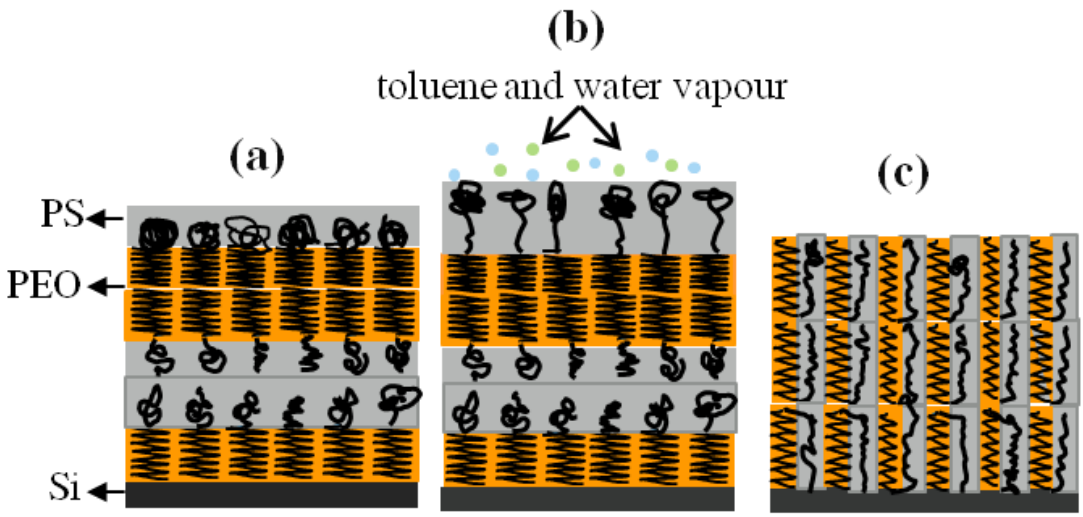


Figure 3.3. Schematic presentation of proposed structure evolution of lamellar PS-*b*-PEO thin film during stepwise thrmo/solvent annealing suggesting (a) parallel orientation of PS and PEO blocks on bare Si substrate after thermal annealing, (b) The swelling of PS chains upon exposure to toluene and the subsequent aggregation of PS chains upon exposure to water vapour to minimize the contact with water, (c) diffusion of PEO to the surface and the perpendicular alignment of the blocks.

Toluene is a good solvent for both polymers but slightly selective for PS whilst water is selective for PEO (the Hildebrand solubility parameter for PS, PEO and toluene are σ_{PEO} = 24.3 $MPa^{0.5}$, σ_{PS} = 18.61 $MPa^{0.5}$, $\sigma_{toluene}$ = 18.3 $MPa^{0.5}$) [45].

We believe that while exposure to toluene will allow PS chains to swell and stretch, as shown in Figure 3.3, the presence of water causes the PS chains to aggregate to minimize the PS – H_2O interactions (Figure 3(b)). The PEO – H_2O interactions are thermodynamically favourable and PEO will, therefore, attempt to maximize its concentration at the film surface area to maximize the contact with water and offset the tendency for PS to be at the surface because of its lower surface energy. Also, the diffusion of toluene molecules in the film will act to reduce the PEO-substrate interactions and decrease the likelihood of forming PEO layers at the polymer – substrate interface [43]. In this way, this annealing step should favour vertical over horizontal alignment of the lamellae (Figure 3.3(c)). Note that the chain orientations shown in Figure 3.3 are not the exact configuration. The chains can be either parallel or perpendicular in both PS and PEO phase-separated domains independently. In the final stage of the stepwise annealing process (step 4), the films are solvent annealed with water and toluene for 2 hrs at 46 °C. This temperature is above the PEO crystallization temperature ($\boldsymbol{T_{PEO}^{C}}$ = 43 °C) and should provide sufficient time for microphase separation ($\chi N \cong 52$) while avoiding breakout crystallization. Upon removal from the oven, if any crystallization occurs it will be confined within micro phase separated domains and therefore the structure will be sustained. The overall process is described in Figure 3.1. The resulting film morphology can be seen in Figure 3.4(a). A perpendicular alignment (i.e. linear structures) of PS and PEO domains with a half pitch of 24 nm was achieved in PS24-PEO24.5.

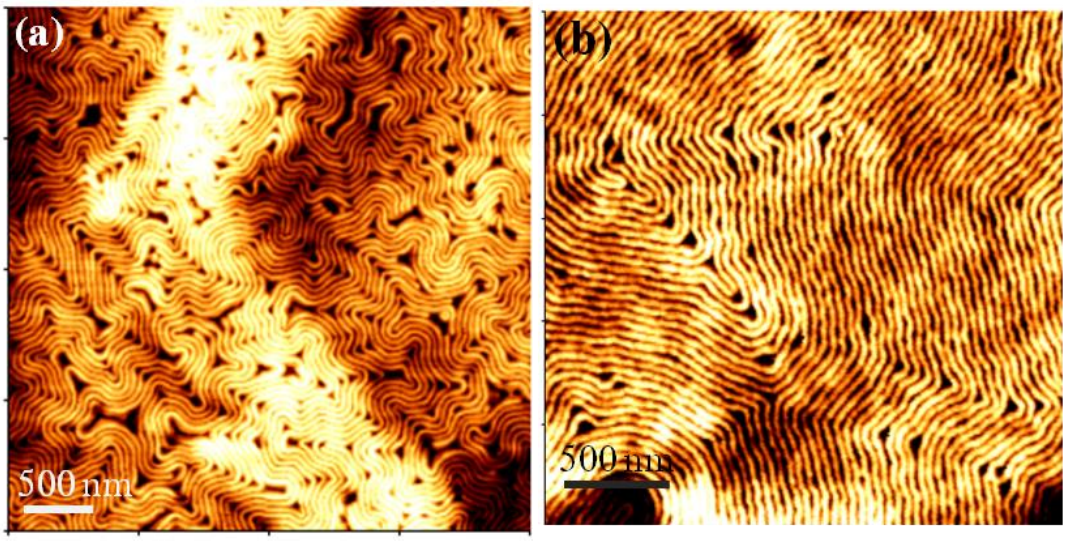


Figure 3.4. An AFM topography image of the laterally phase separated lamellar PS-*b*-PEO films after stepwise thermo/solvent annealing process (a) in PS24-*b*-PEO24.5 film with half pitch of 24 nm and (b) in PS12.5-*b*-PEO14 film with 17 nm half pitch.

3.4.2 Influence of Molecular Weight

To confirm the validity of this approach, the same method was applied to the PS12.5-*b*-PEO14 block copolymer with number average molecular weight, $M_{n,\mathrm{PS}}$ = 12.5 K and $M_{n,\mathrm{PEO}}$ = 14 K (see Table 3.1). As this block copolymer has a lower molecular weight compared to PS24-PEO24.5, the melting and crystallization temperature of PEO block are lower, and therefore, the annealing temperature was adjusted accordingly. The films were isothermally annealed at 90 °C for 150 minutes, then cooled to 75 °C and then exposed to toluene and water, before being returned to the oven at 66 °C and thermo/solvent annealed at 40 °C for 135 minutes. The data presented in Figure 3.4(b) shows phase-separated PS-*b*-PEO lines with half pitch size of 17 nm. The measured pitch values, $\boldsymbol{d_{PS24-PEO24.5}}$ = 48 *nm* and $\boldsymbol{d_{PS12.5-PEO14}}$ = 34 nm have a relatively good agreement with mean field theory for prediction of domain spacing in lamellar semicrystalline diblock ($\boldsymbol{d = NN_a^{-5/12}}$) [46]. N is the total degree of polymerisation and N_a is the degree of polymerisation for the amorphous block.

3.4.3 Pattern transfer

To demonstrate that these structures have a morphology consistent with the surface imaging in Figure 3.4 (i.e. the patterns are not restricted to the surface region and may be used to generate topographical patterns), we attempted to use the polymer patterns to create substrate topography via pattern transfer. PEO removal can be achieved by either a wet or dry etch. A wet, selective etch of the PEO segment can be achieved using HI (the film is immersed in aqueous HI at 60 °C for 5 days followed by rinsing with methanol and water) [27]. Subsequent TEM cross-section analysis (Figure 3.5(a)) shows that the pattern extends from the exterior towards the substrate surface. As can be seen, the wet etch methodology is not successful in removing the entire polymer and either residual material or a wetting layer was formed. More extensive etch periods by wet method led to degradation of the structure. A more successful process was developed using a dry etch procedure performed in an Oxford Instruments Plasmatech in RIE mode using a mixture of CF_4/O_2. Figure 5(b) shows the tilted cross-section image of the film after the etch. Only residual PEO could be detected using either FTIR or XPS (See Appendix – Chapter 3, Figure S3.6.1 and S3.6.2, respectively). The remaining PS mask after the PEO etch was pattern transferred to a silicon substrate using a SF_6/CF_4 etch [8], [9] followed by a thermal oxidation to remove all traces of polymer. A SEM image of the film, as displayed in Figure 3.5(c), shows the silicon pattern that results, and it can be concluded that successful pattern transfer of the PS template into the Si substrate and fabrication of Si nanowires has been achieved. This is a notable result, because typically the systems that have generally been used for pattern transfer to substrate surfaces are PS-*b*-PMMA or PS-*b*-PMDS, and this work extends the range of polymers that may be used without any surface modification (i.e., brushes, SAMs, etc.). PS-*b*-PEO may have considerable advantages over other

systems because of its relatively high χ value allowing extensibility to very small feature sizes [18] and the ease of chemically modifying the PEO block.

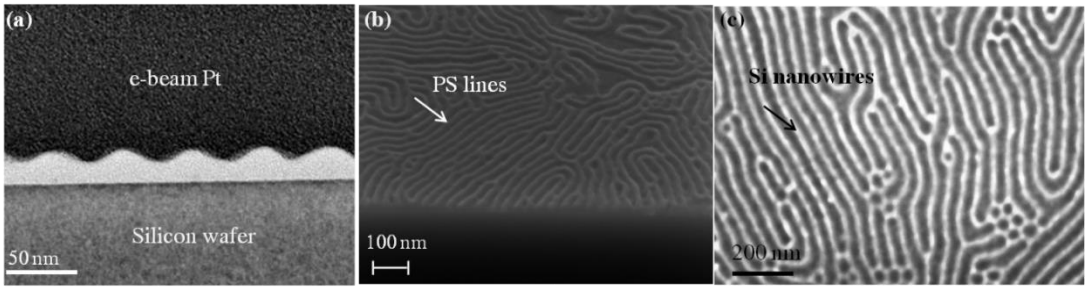


Figure 3.5. Etch and pattern transfer of PS-*b*-PEO film. (a) a TEM cross-section image of the film after the wet etch in HI, (b) a tilted cross section SEM image of PS template at a 30° after removal of PEO with CF_4/O_2 dry etch, (c) a SEM image silicon nanowires through pattern transfer of PS template.

3.5 Conclusions

In summary, we have developed a simple method, stepwise thermo/solvent annealing, to achieve laterally phase-separated line morphology in lamellar PS-*b*-PEO systems without neutralizing the surface of the Si substrate or modifying the polymer solution. The stepwise thermo/solvent annealing consists of four critical steps: (i) isothermal annealing of the sample to mobilize the polymer chains, (ii) cooling the sample to allow unfolded chains structure to slowly relax, (iii) mixed solvent annealing, each selective for one polymer and finally, (iv) non-isothermal (thermo/solvent) annealing starts from above melting temperature of PEO and stops a few degrees above the crystallization temperature of PEO block. This simple method could possibly be a generic methodology that could be successfully applied to other semicrystalline block copolymer systems. As outlined here, applying the method to two different lamellar PS-*b*-PEO systems allowed the generation of well-defined vertical lamellae structures, which were utilized for pattern transfer into silicon substrate and may ultimately

enable the fabrication of arrays of nanowires on large area substrates, for example, silicon wafers.

3.6 References

[1] S. O. Kim, H. H. Solak, M. P. Stoykovich, N. J. Ferrier, J. J. De Pablo, and P. F. Nealey, "Epitaxial self-assembly of block copolymers on lithographically defined nanopatterned substrates.," *Nature*, vol. 424, no. 6947, pp. 411–4, 2003.

[2] S. W. Chang, R. Ayothi, D. Bratton, D. Yang, N. Felix, H. B. Cao, H. Deng, and C. K. Ober, "Sub-50 nm feature sizes using positive tone molecular glass resists for EUV lithography," *J. Mater. Chem.*, vol. 16, no. 15, p. 1470, 2006.

[3] R. A. Farrell, T. G. Fitzgerald, D. Borah, J. D. Holmes, and M. A. Morris, "Chemical Interactions and Their Role in the Microphase Separation of Block Copolymer Thin Films," *Int. J. Mol. Sci.*, vol. 10, no. 9, pp. 3671–3712, Aug. 2009.

[4] R. A. Farrell, N. Petkov, M. A. Morris, and J. D. Holmes, "Self-assembled templates for the generation of arrays of 1-dimensional nanostructures: From molecules to devices," *J. Colloid Interface Sci.*, vol. 349, no. 2, pp. 449–472, Sep. 2010.

[5] D. Borah, S. Rasappa, R. Senthamaraikannan, M. T. Shaw, J. D. Holmes, and M. A. Morris, "The sensitivity of random polymer brush-lamellar polystyrene-b-polymethylmethacrylate block copolymer systems to process conditions," *J. Colloid Interface Sci.*, vol. 393, no. 1, pp. 192–202, 2013.

[6] P. Mansky, "Controlling Polymer-Surface Interactions with Random Copolymer Brushes," *Science (80-.).*, vol. 275, no. 5305, pp. 1458–1460, Mar. 1997.

[7] D. J. C. Herr, "Directed block copolymer self-assembly for nanoelectronics fabrication," *J. Mater. Res.*, vol. 26, no. 2, pp. 122–139, 2011.

[8] D. Borah, M. T. Shaw, S. Rasappa, R. A. Farrell, C. O'Mahony, C. M. Faulkner, M. Bosea, P. Gleeson, J. D. Holmes, and M. A. Morris, "Plasma etch technologies for the development of ultra-small feature size transistor devices," *J. Phys. D. Appl. Phys.*, vol. 44, no. 17, p. 174012, May 2011.

[9] R. A. Farrell, N. Petkov, M. T. Shaw, V. Djara, J. D. Holmes, and M. A.

Morris, “Monitoring PMMA Elimination by Reactive Ion Etching from a Lamellar PS- b -PMMA Thin Film by ex Situ TEM Methods,” *Macromolecules*, vol. 43, no. 20, pp. 8651–8655, Oct. 2010.

[10] I. W. Hamley, “Ordering in thin films of block copolymers: Fundamentals to potential applications,” *Prog. Polym. Sci.*, vol. 34, no. 11, pp. 1161–1210, 2009.

[11] M. W. Matsen, “Self-assembly of block copolymers in thin films,” *Curr. Opin. Colloid Interface Sci.*, vol. 3, no. 1, pp. 40–47, 1998.

[12] S. H. Kim, M. J. Misner, and T. P. Russell, “Controlling orientation and order in block copolymer thin films,” *Adv. Mater.*, vol. 20, no. 24, pp. 4851–4856, 2008.

[13] S. Hong, W. J. MacKnight, T. P. Russell, and S. P. Gido, “Structural Evolution of Multilayered, Crystalline−Amorphous Diblock Copolymer Thin Films,” *Macromolecules*, vol. 34, no. 9, pp. 2876–2883, Apr. 2001.

[14] G. J. Kellogg, D. G. Walton, A. M. Mayes, P. Lambooy, T. P. Russell, P. D. Gallagher, and S. K. Satija, “Observed Surface Energy Effects in Confined Diblock Copolymers,” *Phys. Rev. Lett.*, vol. 76, no. 14, pp. 2503–2506, Apr. 1996.

[15] M. W. Matsen, “Thin films of block copolymer,” *J. Chem. Phys.*, vol. 106, no. 18, pp. 7781–7791, May 1997.

[16] S. Kim, R. M. Briber, A. Karim, R. L. Jones, and H. Kim, “Environment-Controlled Spin Coating To Rapidly Orient Microdomains in Thin Block Copolymer Films,” *Macromolecules*, vol. 40, no. 12, pp. 4102–4105, Jun. 2007.

[17] L. Li, Y. Séréro, M. H. J. Koch, and W. H. de Jeu, “Microphase Separation and Crystallization in an Asymmetric Diblock Copolymer: Coupling and Competition,” *Macromolecules*, vol. 36, no. 3, pp. 529–532, Feb. 2003.

[18] S. Park, D. H. Lee, J. Xu, B. Kim, S. W. Hong, U. Jeong, T. Xu, and T. P. Russell, “Macroscopic 10-terabit-per-square-inch arrays from block copolymers with lateral order.,” *Science*, vol. 323, no. February, pp. 1030–1033, 2009.

[19] P. Mokarian-Tabari, T. W. Collins, J. D. Holmes, and M. A. Morris, “Cyclical ‘Flipping’ of Morphology in Block Copolymer Thin Films,” *ACS Nano*, vol. 5, no. 6, pp. 4617–4623, Jun. 2011.

[20] T. H. Kim, J. Hwang, W. S. Hwang, J. Huh, H.-C. Kim, S. H. Kim, J. M. Hong, E. L. Thomas, and C. Park, "Hierarchical Ordering of Block Copolymer Nanostructures by Solvent Annealing Combined with Controlled Dewetting," *Adv. Mater.*, vol. 20, no. 3, pp. 522–527, Feb. 2008.

[21] G. G. Pereira and D. R. M. Williams, "Thin Films of Perpendicularly Oriented Diblock Copolymers: Lamellar Distortions Driven by Surface−Diblock Interfacial Tensions," *Macromolecules*, vol. 32, no. 5, pp. 1661–1664, Mar. 1999.

[22] E. Sivaniah, Y. Hayashi, S. Matsubara, S. Kiyono, T. Hashimoto, K. Fukunaga, E. J. Kramer, and T. Mates, "Symmetric Diblock Copolymer Thin Films on Rough Substrates. Kinetics and Structure Formation in Pure Block Copolymer Thin Films," *Macromolecules*, vol. 38, no. 5, pp. 1837–1849, Mar. 2005.

[23] E. Sivaniah, Y. Hayashi, M. Iino, T. Hashimoto, and K. Fukunaga, "Observation of Perpendicular Orientation in Symmetric Diblock Copolymer Thin Films on Rough Substrates," *Macromolecules*, vol. 36, no. 16, pp. 5894–5896, Aug. 2003.

[24] T. Xu, C. J. Hawker, and T. P. Russell, "Interfacial Interaction Dependence of Microdomain Orientation in Diblock Copolymer Thin Films," *Macromolecules*, vol. 38, no. 7, pp. 2802–2805, Apr. 2005.

[25] J. Kao, J. Tingsanchali, and T. Xu, "Effects of Interfacial Interactions and Film Thickness on Nonequilibrium Hierarchical Assemblies of Block Copolymer-Based Supramolecules in Thin Films," *Macromolecules*, vol. 44, no. 11, pp. 4392–4400, Jun. 2011.

[26] T. L. Morkved and H. M. Jaeger, "Thickness-induced morphology changes in lamellar diblock copolymer ultrathin films," *Europhys. Lett.*, vol. 40, no. 6, pp. 643–648, Dec. 1997.

[27] H. Mao and M. A. Hillmyer, "Nanoporous polystyrene by chemical etching of poly(ethylene oxide) from ordered block copolymers," *Macromolecules*, vol. 38, no. 9, pp. 4038–4039, 2005.

[28] T. G. Fitzgerald, R. A. Farrell, S. O'Driscoll, C. T. O'Mahony, J. D. Holmes, and M. A. Morris, "Orientation and Translational Control of PS-b-PEO/PS Thin Films via Solvent Annealing and Graphoepitaxy Techniques," *e-Journal Surf. Sci. Nanotechnol.*, vol. 7, no. April, pp. 471–475, 2009.

[29] L. Zhu, S. Z. D. Cheng, B. H. Calhoun, Q. Ge, R. P. Quirk, E. L. Thomas, B. S. Hsiao, F. Yeh, and B. Lotz, "Phase structures and morphologies determined by self-organization, vitrification, and crystallization: Confined crystallization in an ordered lamellar phase of PEO-b-PS diblock copolymer," *Polymer (Guildf).*, vol. 42, no. 13, pp. 5829–5839, 2001.

[30] I. I. Potemkin, "Lamellar Orientation in Thin, Supported Diblock Copolymer Films: Strong Segregation Theory," *Macromolecules*, vol. 37, no. 9, pp. 3505–3509, May 2004.

[31] E. Huang, T. P. Russell, C. Harrison, P. M. Chaikin, R. A. Register, C. J. Hawker, and J. Mays, "Using Surface Active Random Copolymers To Control the Domain Orientation in Diblock Copolymer Thin Films," *Macromolecules*, vol. 31, no. 22, pp. 7641–7650, 1998.

[32] P. Busch, D. Posselt, D. Smilgies, B. Rheinländer, and F. Kremer, "Lamellar Diblock Copolymer Thin Films Investigated by Tapping Mode Atomic Force Microscopy: Molar-Mass Dependence of Surface Ordering," *Macromolecules*, vol. 36, no. 23, pp. 8717–8727, Nov. 2003.

[33] R. D. Peters, X. M. Yang, and P. F. Nealey, "Morphology of Thin Films of Diblock Copolymers on Surfaces Micropatterned with Regions of Different Interfacial Energy," *Macromolecules*, vol. 35, no. 5, pp. 1822–1834, Feb. 2002.

[34] W. Stocker, "Lamellar Orientation at the Surface of Thin Block Copolymer Films," vol. 9297, no. 98, pp. 5536–5538, 1998.

[35] W. N. He and J. T. Xu, "Crystallization assisted self-assembly of semicrystalline block copolymers," *Prog. Polym. Sci.*, vol. 37, no. 10, pp. 1350–1400, 2012.

[36] E. Metwalli, J. Perlich, W. Wang, A. Diethert, S. V. Roth, C. M. Papadakis, and P. Müller-Buschbaum, "Morphology of semicrystalline diblock copolymer thin films upon directional solvent vapor flow," *Macromol. Chem. Phys.*, vol. 211, no. 19, pp. 2102–2108, 2010.

[37] I. W. Hamley, "Crystallization in Block Copolymers," in *Interfaces Crystallization Viscoelasticity*, vol. 148, Berlin, Heidelberg: Springer Berlin Heidelberg, 1999, pp. 113–137.

[38] M. Muthukumar, "Competing Interactions and Levels of Ordering in Self-Organizing Polymeric Materials," *Science (80-.).*, vol. 277, no. 5330, pp.

1225–1232, Aug. 1997.

[39] Y.-L. Loo, R. A. Register, A. J. Ryan, and G. T. Dee, "Polymer Crystallization Confined in One, Two, or Three Dimensions," *Macromolecules*, vol. 34, no. 26, pp. 8968–8977, Dec. 2001.

[40] G. Reiter, G. Castelein, P. Hoerner, G. Riess, A. Blumen, and J.-U. Sommer, "Nanometer-Scale Surface Patterns with Long-Range Order Created by Crystallization of Diblock Copolymers," *Phys. Rev. Lett.*, vol. 83, no. 19, pp. 3844–3847, Nov. 1999.

[41] Y.-L. Loo, R. A. Register, and A. J. Ryan, "Polymer Crystallization in 25-nm Spheres," *Phys. Rev. Lett.*, vol. 84, no. 18, pp. 4120–4123, May 2000.

[42] G. Reiter, G. Castelein, P. Hoerner, G. Riess, J.-U. Sommer, and G. Floudas, "Morphologies of diblock copolymer thin films before and after crystallization," *Eur. Phys. J. E*, vol. 2, no. 4, p. 319, 2000.

[43] P. Yang and Y. Han, "Crystal Growth Transition from Flat-On to Edge-On Induced by Solvent Evaporation in Ultrathin Films of Polystyrene-b-Poly(ethylene oxide)," *Langmuir*, vol. 25, no. 17, pp. 9960–9968, Sep. 2009.

[44] D. Chen, Y. Gong, H. Huang, T. He, and F. Zhang, "Competition of Lamellar Orientation in Thin Films of a Symmetric Poly(styrene)- b -poly(l -lactide) Diblock Copolymer in Melt State," *Macromolecules*, vol. 40, no. 18, pp. 6631–6637, Sep. 2007.

[45] A. F. M. Barton, *CRC Handbook of Polymer–Liquid Interaction Parameters and Solubility Parameters*. Boca Raton: CRC Press, 1990.

[46] M. D. Whitmore and J. Noolandi, "Theory of crystallizable block copolymer blends," *Macromolecules*, vol. 21, no. 5, pp. 1482–1496, Sep. 1988.

3.7 Appendix

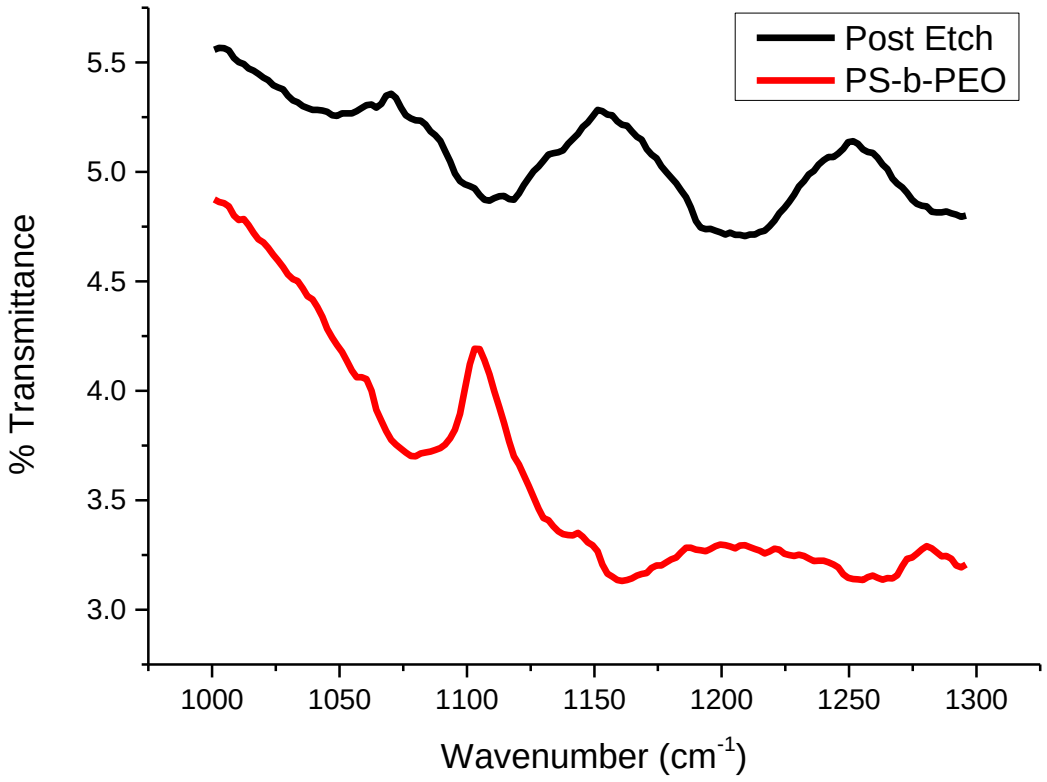


Figure S3.7.1. FTIR spectra of PS24-*b*-PEO24.5 as prepared (red) and following dry etching (black). The characteristic C-O-C ether peak at 1070-1130 cm^{-1} is significantly less defined following etching.

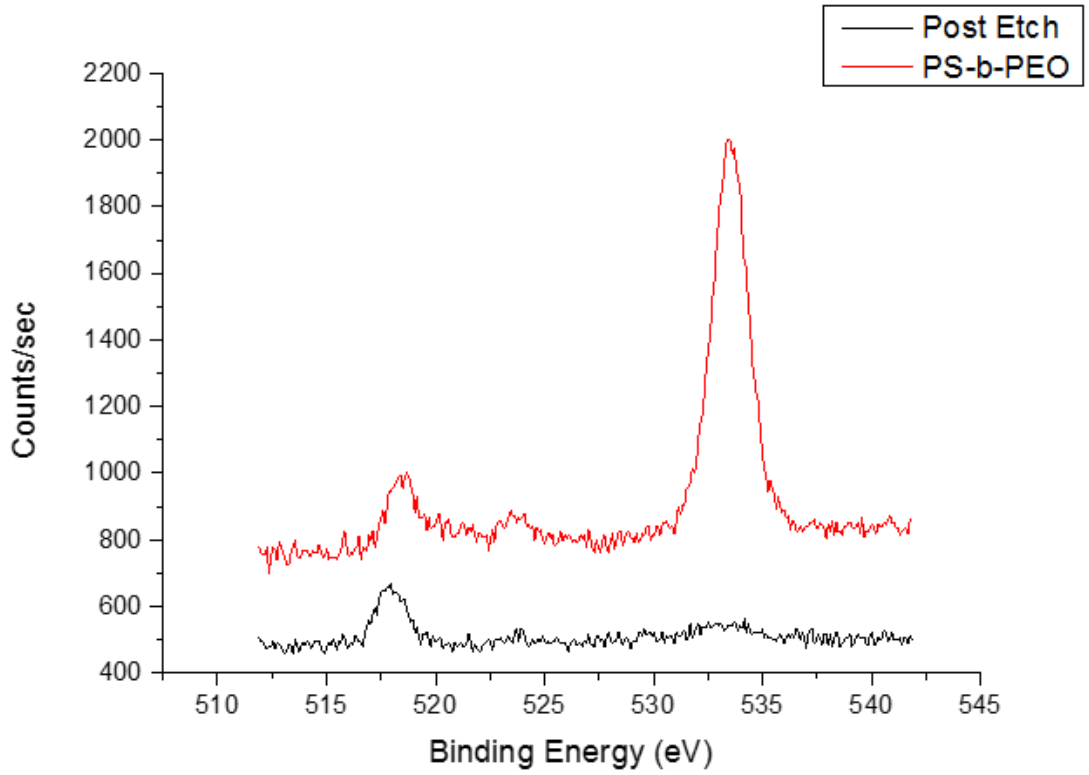


Figure S3.7.2. XPS spectra of PS24-*b*-PEO24.5 as prepared (red) and following dry etching (black). The characteristic oxygen 1s peak at 533 eV has been largely removed by the etching process.

Chapter 4

Dimensional and Defectivity Data Collection for Block Copolymer Thin Film Metrology

4.1 Abstract

Block copolymers have a wide range of potential applications in nanoscale fabrication due to their tuneable feature size, well-ordered patterns and scalability. For these patterns to be successfully utilised, long range order, and low defectivity must be achieved as the fabrication of these systems have exacting specifications. To achieve this high level of order, detailed metrology is required. This chapter demonstrates applications for quantitative measurement of feature size, uniformity and defectivity within BCP patterns. These methods are applied to PS-*b*-PMMA films. The ability to identify defects in both dot and line patterns, in addition to determining uniformity of the period, critical dimension, including line-width roughness and line-edge roughness is also shown.

4.2 Introduction

High density, ordered arrays of nanostructures on substrate surfaces have been intensely explored due to their potential applications in semiconductor devices, information storage, photonic materials and bio-sensors [1]–[5]. In these applications, there is a requirement for nanostructures with structural uniformity, with precise control on the arrangement, shape and orientation. Within the semiconductor industry, as the ability of well-established photolithography techniques approach the physical limitations of dimensions that can be achieved, the establishment of alternative techniques has become paramount [6]–[8]. As challenges in "top-down" methods have impeded their advancement, interest in "bottom-up" self-assembly techniques has grown [9]. The self-assembly of block copolymers (BCPs) in thin films offers a cost-effective, scalable method to obtain ordered, sub-20 nm features [10], [11].

Whilst significant work has been performed on the use of PS-*b*-PMMA, a number of challenges must be overcome before their introduction. These include poor etch selectivity to dry etch processes [12], and limited ability to achieve features in the sub-10 nm range due to its relatively small Flory-Huggins interaction parameter (χ, measures the chemical dissimilarity of the BCP constituent blocks) of 0.038 [13]. The most significant roadblock is the large amount of defects that exist in BCP generated patterns compared to other lithographical techniques, with defect densities of <0.01 cm^{-2} required [14], [15]. Advanced methods, such as directed self-assembly have shown significant defect reduction, however levels still exceed industry requirements [16]. These factors necessitate the development of "high-χ" BCPs, with smaller period, improved etch contrast and reduced defectivity [17]–[21], including PS-*b*-PDMS [22], [23], PS-*b*-P4VP [24] and PS-*b*-PHEMA [25]. As new systems are produced, they must undergo a process of evaluation to determine their viability. To aid in their assessment, a quantitative method for pattern evaluation is required.

Quantitative analysis of BCP patterns have been conducted for two decades, beginning with Fourier transform as a method of determining L_0 and estimating order [26]. This was expanded into the study of defects within patterns as microscopy methods advanced by Harrison *et al* [27] and Segalman *et al* [28]. Since then, improved tools have been developed allowing for more in-depth analysis, notably by Simão *et al* [23], [29] and Murphy *et al* [30], [31]. More advanced methods for analysis of BCP patterns have been introduced in DSA processes [32]–[35]. However, these developments have been predominantly been in-house, giving little detail on the exact methods employed.

In this work, novel applications for analysing both dot and line patterns on planar silicon substrates from SEM and AFM images are described. It is shown that it is

capable of determining key properties including defectivity, L_0, CD, LWR, LER, and ordering. It is applied to real scenarios to illustrate its utility and robustness.

4.3 Experimental Method

4.3.1 Materials

Planer substrates used were single crystal <100> silicon wafers (P type) with a native oxide layer (~2 nm). Cylinder and lamellar forming PS-*b*-PMMA BCPs were supplied by Arkema under the tradename Nanostrength® EO. These BCPs have a target period (L_0) and PS: PMMA volume ratio as detailed in Table 4.1. These BCPs were used in association with PS-*r*-PMMA random copolymers, functionalised for the creation of brush layers. Propylene glycol methyl ether acetate (PGMEA) (ReagentPlus, ≥99.5%), acetone (ACS reagent, ≥99.5%), 2-propanol (IPA) (CHROMASOLV, for HPLC, 99.9%), sulfuric acid (H_2SO_4, ACS reagent, 95.0-98.0%), hydrogen peroxide (H_2O_2, contains inhibitor, 30 wt. % in H_2O, ACS reagent), and acetic acid (ACS reagent, ≥99.7%) were purchased from Sigma-Aldrich and used as received. De-ionized (DI) water was used wherever necessary.

Table 4.1. Details of the block copolymers used for the present study.

Name	Type	Morphology	PS:PMMA vol. ratio	Target Period/nm	Brush
C35	Pure	Cylinders	70:30	35	NL1
L40	Pure	Lamellar	45:55	40	NL2
L40S	Blend	Lamellar	45:55	40	NL2

4.3.2 Process

Substrates were cut into 2 cm^2 pieces cleaned by ultrasonication in acetone and IPA for 10 min each and dried under a stream of nitrogen gas. This was followed by surface activation in a piranha solution (1:3 v/v 30% H_2O_2/H_2SO_4) at 90 °C for 30 min, followed by rinsing in excess DI water and dried under nitrogen flow. This process produces hydroxyl groups on the surface. PS-*r*-PMMA solutions of 1-2 wt.% in PGMEA were spin-cast on silicon substrates at 1500 rpm for 30 sec. Samples were annealed under vacuum at 170 °C for 30-360 min (NL1) and 360 min (NL2), allowing for brush layers to be grafted to the substrate. The substrates were then rinsed repeatedly with PGMEA to remove ungrafted polymer brush and dried at 60 °C for 30 min.

BCP films thin films were deposited onto brush coated substrates by spin coating (1500 rpm, 30 sec) from solutions of 1-2 wt. % in PGMEA. Films were thermally annealed at 275 °C for 20 min (L40, L40S) and 30 min (C35).

For characterization purposes, PS-*b*-PMMA films were subjected to a selective PMMA etch to enhance contrast and create the type of matrix-space pattern required for pattern transfer. For C35 films, a wet etch method was used where the film was exposed to UV (184.9 nm and 253.7 nm) for 10 min under nitrogen in a UV/ozone system (PSD Pro Series Digital UV Ozone System; Novascan Technologies, Inc., USA) to cross-link the PS block. The PMMA block was then etched by substrate immersion in acetic acid for 10 min, followed by rinsing with excess DI water and dried under nitrogen flow [36]. L40 and L40S films were dry etched with an Oxford Instruments Plasmatech 100 system operating in RIE mode using oxygen (O_2) and

trifluoromethane (CHF_3). A selective reactive ion etch process at 100W, with CHF_3/O_2 flow rates of 40sccm/5sccm at 10mTorr for 40-60 sec was used [37].

4.3.3 Characterization

4.3.3.1 Scanning Electron Microscopy (SEM)

Top-down SEM images of samples were obtained by a Zeiss Ultra Plus and Zeiss Supra 40 Scanning Electron Microscopes operating at an accelerating voltage of 3-5 kV.

4.3.3.2 Atomic Force Microscopy (AFM)

AFM (Park systems, XE-100) was operated in non-contact mode under ambient conditions using silicon microcantilever probe tips with a force constant of 42 N m^{-1}. Topographic images were recorded.

4.3.4 Image Analysis

Microscopy images of BCP patterns were processed using Park XEI, ImageJ and Gwyddion image software. Processed and unprocessed images were characterised using an image analysis program coded in Matlab (v. R2016a, The Mathworks, Natick, MA).

4.4 Results

Examples of two types of nanopattern morphologies, dots and lines, produced from BCP self-assembly of PS-*b*-PMMA are presented in Figure 4.1. These patterns have undergone selective PMMA etching to enhance the contrast between the PS and PMMA blocks with darker regions representing the space vacated by the PMMA block. While these patterns can be assessed visually to some extent, it is not possible

to discern the extent of non-uniformity and defectivity without quantitative analysis, as demonstrated in Table 4.2.

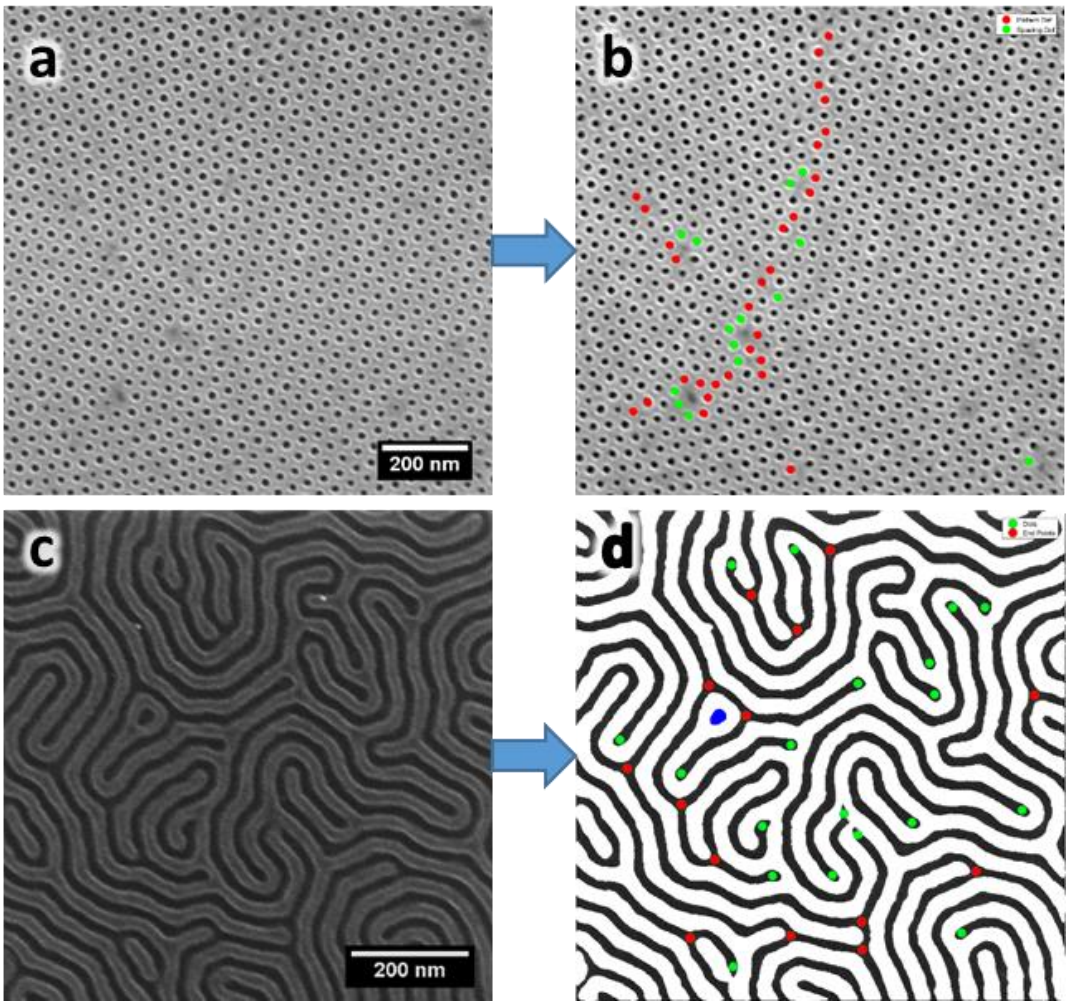


Figure 4.1. Sample SEM images of PS-*b*-PMMA demonstrating defect analysis. (a, b) corresponds to cylinder forming C35. (c, d) corresponds to lamellar forming L40.

Table 4.2. Data for the images in Figure 4.1, demonstrating the data gained from the quantitative analysis process.

Image	Polymer	L_0 /nm	L_0 3σ /nm	CD /nm	CD 3σ /nm	LER /nm	Defect /um^2	Order
a	C35	37.9	9.5	13.4	3.3	n/a	43.2	0.68
c	L40	38.7	6.9	24.3	5.7	3.7	62.9	0.34

4.4.1 Dots Pattern Analysis

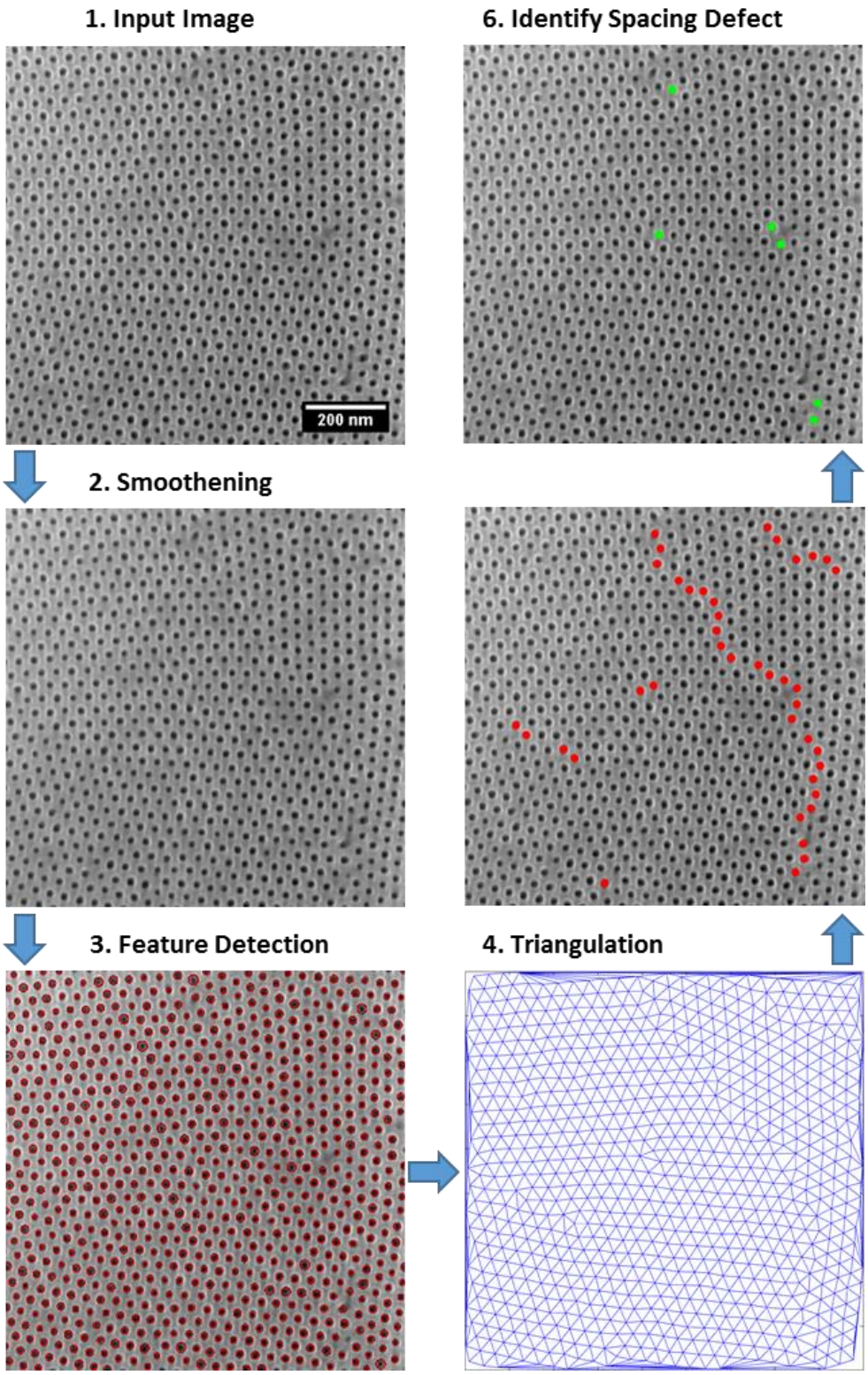


Figure 4.2. A visual overview of the analysis method for dot patterns

In order to perform quantitative analysis of dimensions and defects in hexagonal dot arrays, we developed an image analysis technique as outlined in Figure 4.2. In order to determine useful information from SEM and AFM images, some details must first be input to the application. These comprise the image width in nanometres and an estimated range for dots size. From this information, along with details measured from the input image, the script determines the nanometre-pixel ratio necessary to return information in the correct units. The dot size range is necessary to prevent false-positives which would skew the results, and allows the script to be adapted for different polymer systems with different feature sizes.

The next stage of the analysis is the application of a smoothening filter to remove noise and enhance contrast, yielding a "cleaner" image. Noise in SEM results from charging and edge effects which can cause distortions and speckling [38]. In AFM, noise can be the result of environmental effects, i.e. vibrations, as well as mechanical interactions [39]. In order to negate these effects, many different smoothening methods have been employed, such as Gaussian filter [40], [41], median and double median filters [31], [42] and bilateral filtering [43]. The effects of these filters are shown in Figure 4.3, employing the in-built Gaussian and median filters, and a bilateral filter developed by D. Lanman based on work by Winnemoller *et al* [44], [45]. Gaussian filtering is a linear operator, thus does not preserve object edges, by averaging the pixel values within the filter range. The median filter is a non-linear, edge preserving operation, which replaces the pixel values with the median value within the filter area [42]. The double median filter is a small, 3x3 pixel median filter to remove speckling followed by a larger median filter to remove additional noise. Here, the larger filter is half the size of the single median filter. Bilateral filtering is

another non-linear, edge preserving filter, which applies a Gaussian filter within smooth areas while preventing averaging over image edges [43].

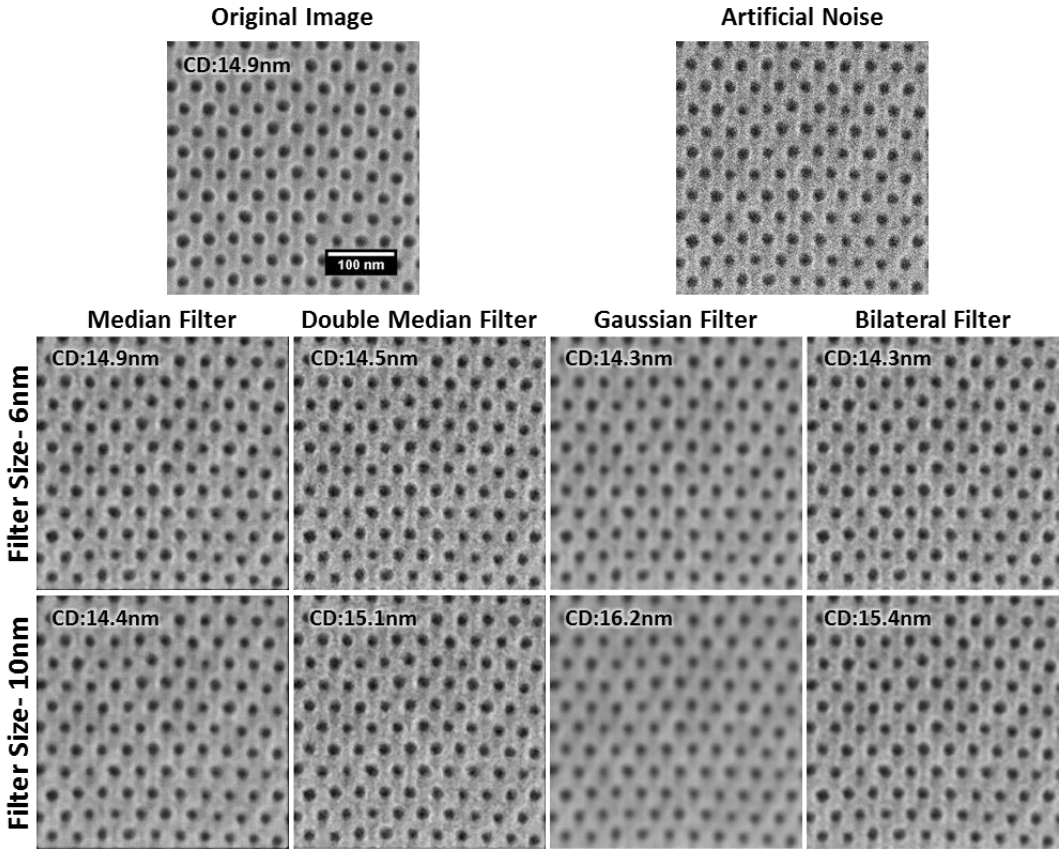


Figure 4.3. A comparison of smoothening filters for noise reduction. Noise was added to original image prior to filtering. Labelled are the mean CD as determined by the script.

From Figure 4.3, it can be seen that a median filter, with a size proportional to 6 nm yielded the best results, maintaining feature size in comparison to the original image while removing the artificial noise.

The next stage is the detection of the dots. Previous works have utilised thresholding and particle counting to detect features [46], [47]. However, this method can lead to conjoined or elongated features if the surface is not smooth. An alternative is the use of a circle Hough transform directly on the smoothened image. This identifies features by transforming the image into a 3D parametric space, similar to a Fourier transform.

It also has the benefits of being more resilient to noise and non-uniform brightness. In this method, pixels with high gradients, i.e. dot edge pixels, are transformed into a 3D parameter space, called an accumulator array. Within this array, maxima points represent circles, which can be transformed back to real space. False returns are filtered by setting a minimum and maximum radius, as well as a sensitivity parameter [48], [49]. Figure 4.4 shows a comparison of the thresholding and Hough transform methods.

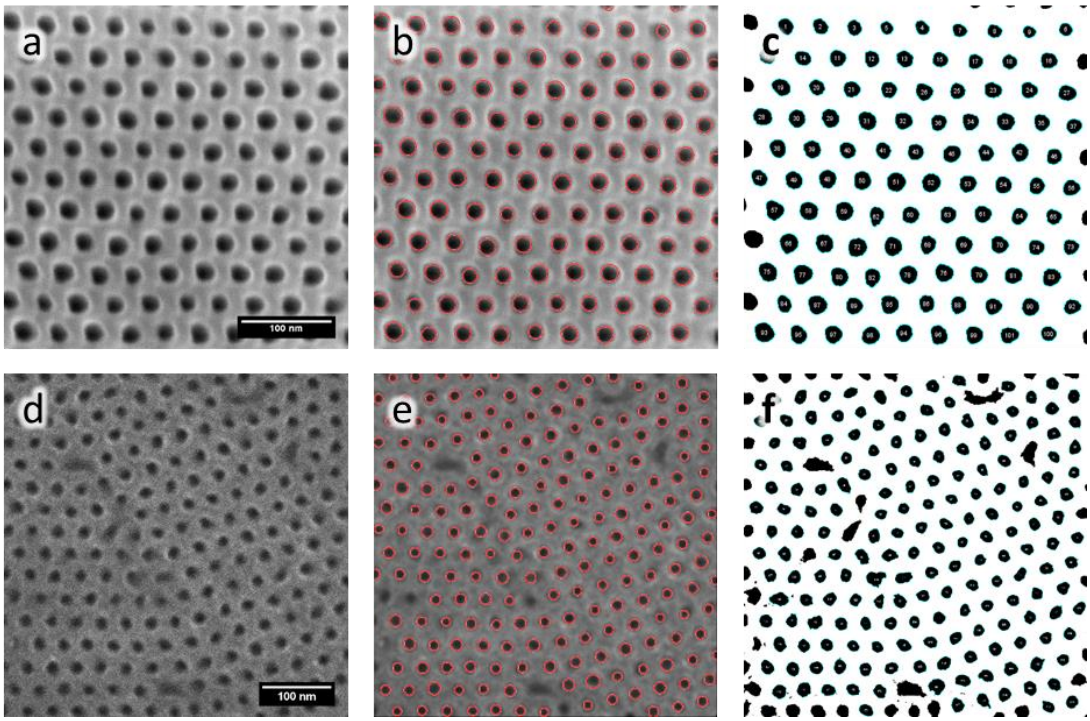


Figure 4.4. A comparison of the Hough transform and threshold methods of feature detection. (a-c) shows the good agreement between both methods on smooth films. (d-f) demonstrate the skewing of features that occurs using the threshold method on non-ideal images.

Table 4.3. Comparison of detected CD uniformity from each method

Image	Method	CD/nm	CD 3σ/nm
b	Hough	17.05	6.57
c	Threshold	16.92	7.05
e	Hough	14.74	4.85
f	Threshold	18.14	5.92

Following this step, relating the position of each dot with its neighbours is necessary to measure the L_0 and identify pattern defects. Both Delaunay triangulations and Voronoi diagrams have been explored in the analysis of hexagonal dot arrays [28], [50], [51]. The Delaunay triangulation works by relating points in triangles, in this case circle centres, such that no points are inside the circumcircle of the triangle [52]. This method is ideal for analysis of hexagonal arrays of dot features as it can reliably identify the number of neighbours each dot has. For a perfectly ordered pattern, each dot should have 6 neighbours; points without 6 neighbours represent pattern defects [53], as depicted in Figure 4.5 (a). The triangulation lines are used to determine L_0 by calculating the Euclidian distance between centres.

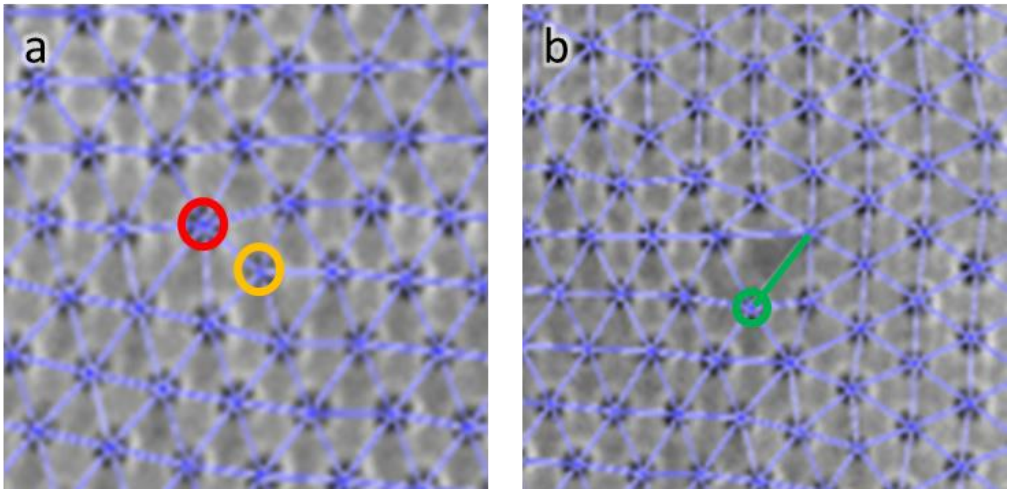


Figure 4.5. Detection of defects. (a) Illustrates a defect pair, where the red circle indicates a dot with 7 neighbours and the yellow circle a dot with 5 neighbours. (b) Demonstrates where the Delaunay triangulation can fail to identify a defect if they align correctly. The green circle and line indicate a dot with 6 neighbours, however the indicated edge and neighbour are too far out of alignment.

Next, "healthy" dots, those which meet the 6 neighbour criteria, are examined to determine if any of their neighbours are too far away. These "spacing defects" may occur where defects align with the pattern. Figure 4.5 (b) shows an enlarged area in which such a scenario exists. In these tests, the 3 sigma limit of the L_0 distribution was

employed as the boundary beyond which edges were detected as defective; however this can be modified to fit specified parameters. Following the identification of all pattern and spacing defects, the L_0 was again calculated excluding all defective points in order to determine a representative "optimised" L_0.

To determine the degree of order in the pattern, an appropriate metric must be applied. This has most commonly been translational and orientational correlation functions [28], [50], [54], [55]. Here, a simplified method of quantifying order is used, a Legendre polynomial order parameter, S_2 described by Zwetkoff [56], [57]:

$$S_2 = \frac{3\langle cos^2\,\theta\rangle - 1}{2} \tag{4.1}$$

where θ is the difference between a director or average orientation and each elements orientation. For a pattern with perfect alignment, $S_2 = 1$, while in a random system it is equal to 0. By taking the edges from the Delaunay triangulation which are not connected to defects and converting them to vectors, an estimate of the degree of ordering can be determined [58]. This is visualised in Figure 4.6, which shows a single grain boundary, and multiple grain boundaries. The order parameter decreases with increasing grains due to the difference in orientation of the dots within.

Finally, descriptive statistics are calculated such as the L_0 3σ and feature size 3σ. The L_0 and feature size are plotted to a Gaussian distribution, allowing for a visualisation of the dimensional uniformity [59].

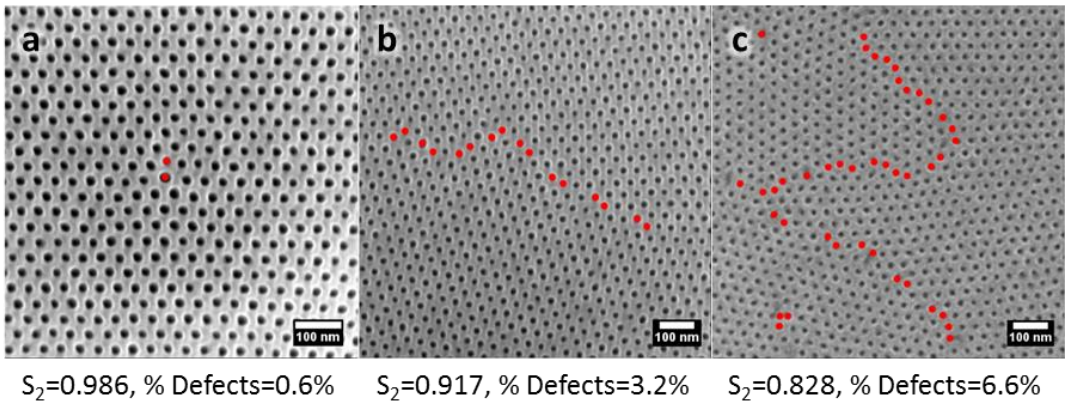


Figure 4.6. Comparison of the order parameter S2 with number of grains, (a) a single grain; (b) two grains; and (c) three grains.

4.4.2 Application of Dot Analysis

To demonstrate the utility of this analysis, it was applied to a real world scenario, the optimisation of brush surface for a cylinder-forming PS-*b*-PMMA BCP. Previous work has shown that the surface affinity has a strong influence on the self-assembly process [60]–[63]. Differentiating variations in pattern quality can be difficult, especially if the changes are minor. To overcome this, analysis was performed on C35 BCP films cast on a NL2 brush layer grafted under different conditions as a method to determine the optimal conditions. In order to reduce variables, the BCP film annealing conditions were maintained at 275 °C for 30 min, while modifying the brush anneal time with constant temperature of 170 °C. AFM and SEM images of the resulting pattern are showed in Figure 4.7. Statistical results produced by the analysis of the SEM images can be found in Table 4.4. From the analysis, it is noted that the best results are achieved at 180 and 360 min, with marginal differences in defectivity, however the 360 min anneal time represents the highest degree of uniformity.

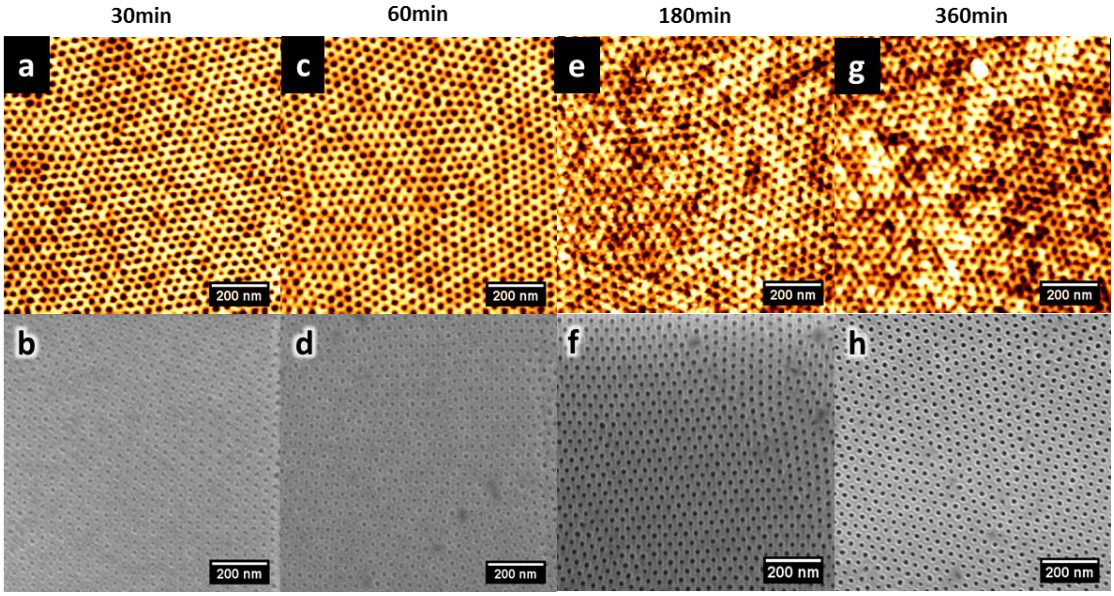


Figure 4.7. Comparison of AFM (top) and SEM (bottom) images of C35 patterns formed on brush layers annealed at 170°C for a,b) 30 min, c,d) 60 min, e,f) 180 min, g,h) 360 min.

Anneal Time	L_0 3σ /nm	CD 3σ /nm	Defect /um^2	Pattern defects	Spacing defects	Defect%	Order
30 min	13.4±0.5	6.3±0.5	55±9	47	18	7.3±1.0	0.71±0.06
60 min	14.8±0.9	6.8±0.9	169±67	2361	422	21±7.4	0.80±0.07
180 min	10.0±1.3	6.5±2.1	49±35	831	339	6.3±4.5	0.84±0.13
360 min	9.6±0.4	5.3±1.0	50±9	652	275	6.2±1.1	0.82±0.08

Table 4.4. Details on the uniformity, defectivity and order with brush anneal time averaged over a minimum of 3 SEM images.

Of particular interest to the analysis method is Figure 4.8, which illustrates the variation of L_0, CD and CD 3σ with anneal time. The curves are ordered by nanometre-pixel ratio, showing the impact of image resolution on the results. The tails on the right of each curve for CD and CD 3σ represent the results from AFM images. These images are of lower resolution than SEM images, typically scanning an area of 4μm^2 with a resolution of 256x256 pixels. In contrast, SEM images are recorded at a resolution of ~1024x768 pixels. Increasing the AFM resolution to 512x512 pixels improved the agreement between the AFM and SEM results. It is worth noting however that the L_0 measured shows only minor deviation with varying resolution.

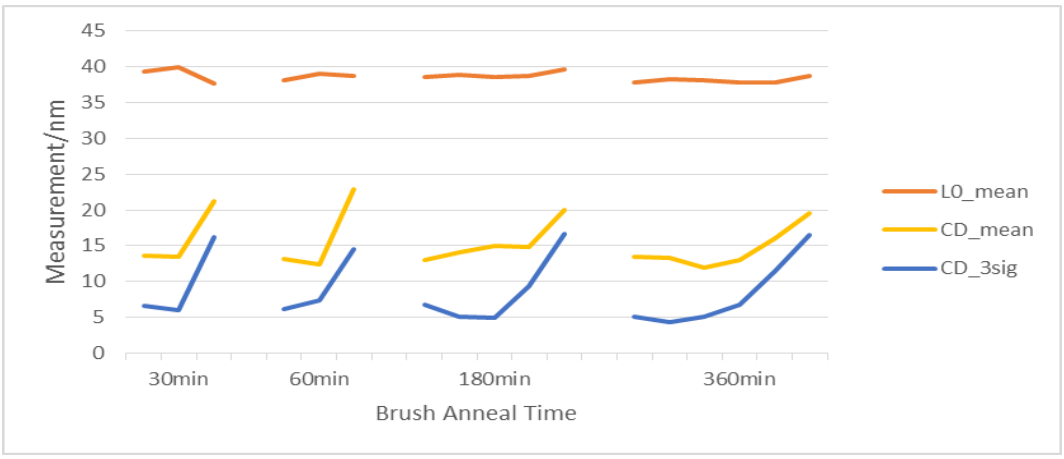


Figure 4.8. Comparison of L_0, CD and CD 3σ with anneal time. Results are ordered by nanometre-pixel ratio of image analysed.

It is also observed that the defect ratio (the ratio of defects to the number of features) and area analysed do not demonstrate a strong correlation, as it would be expected that smaller sample areas would result in few detected defects, see Figure 4.9.

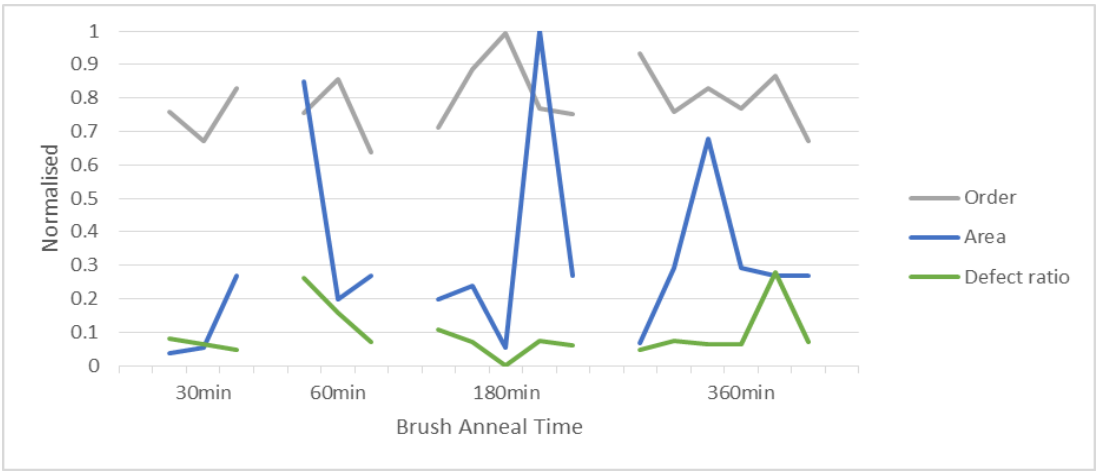


Figure 4.9. Comparison of order parameter, defect ratio and area (normalised) with anneal time. Results are ordered by nanometre-pixel ratio of image analysed.

4.4.3 Line Pattern Analysis

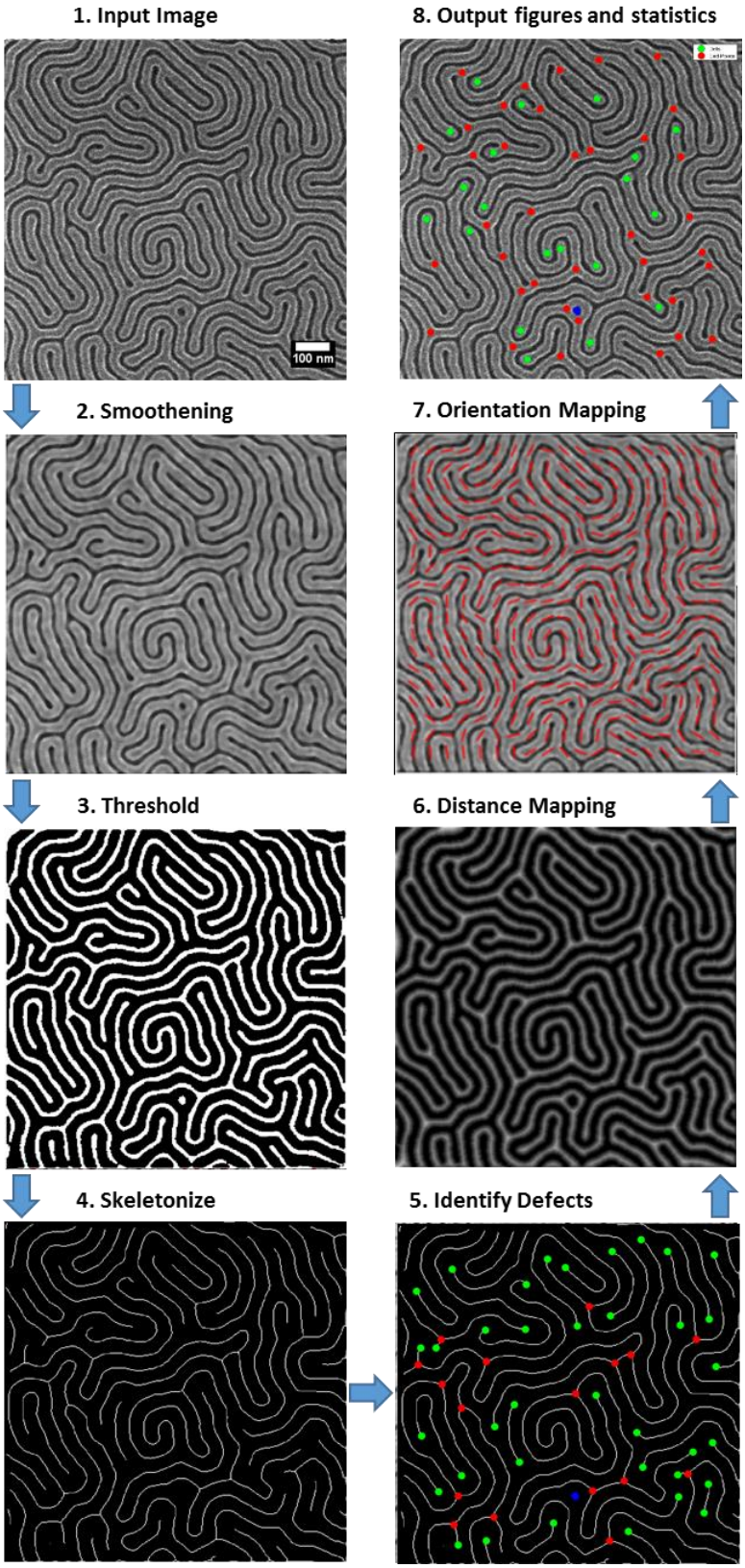


Figure 4.10. An overview of the analysis process for line patterns.

Analysis of fingerprint line patterns was performed as outlined in Figure 4.10. As with the dot pattern analysis, the initial step is the input of the image width for the determination of the nanometre-pixel ratio.

In order to detect features in a line pattern, the image must be threshold to a binary image. This approach has also been used to analyse human fingerprints [64]. This process represents the two polymer blocks as either black or white segments. As shown in Figure 4.4, thresholding can generate errors in the detected pattern due to inconsistences in brightness, contrast, edge effects and background noise. To retain as much information as possible, the image must be levelled and smoothened prior to thresholding to eliminate unwanted artefacts, see Figure 4.11. To level the image, a large averaging filter was applied to generate a background map of the image. This background map is then subtracted from the original image and the contrast enhanced to create a levelled image. A median filter with nominal size of 14 nm is then applied to smoothen the image and reduce noise. This filter can be larger than those applied to the dot patterns, due to the structure of the patterns, this does not distort the features as with dots.

Segmentation of the image to binary can now be performed by the application of a thresholding process [47]. Here, a local Otsu threshold was then applied. This method calculates the threshold based on the mean local intensity in the region surrounding each pixel, allowing for a more accurate binary image then if a global threshold was used as it is more robust to latent variations following smoothening [65], [66]. When the surface is not uniform, such as the presence of featureless areas or surface defects, this method can result in additional artefacts. To account for this, the objects are filtered by area so that features below a limit are removed.

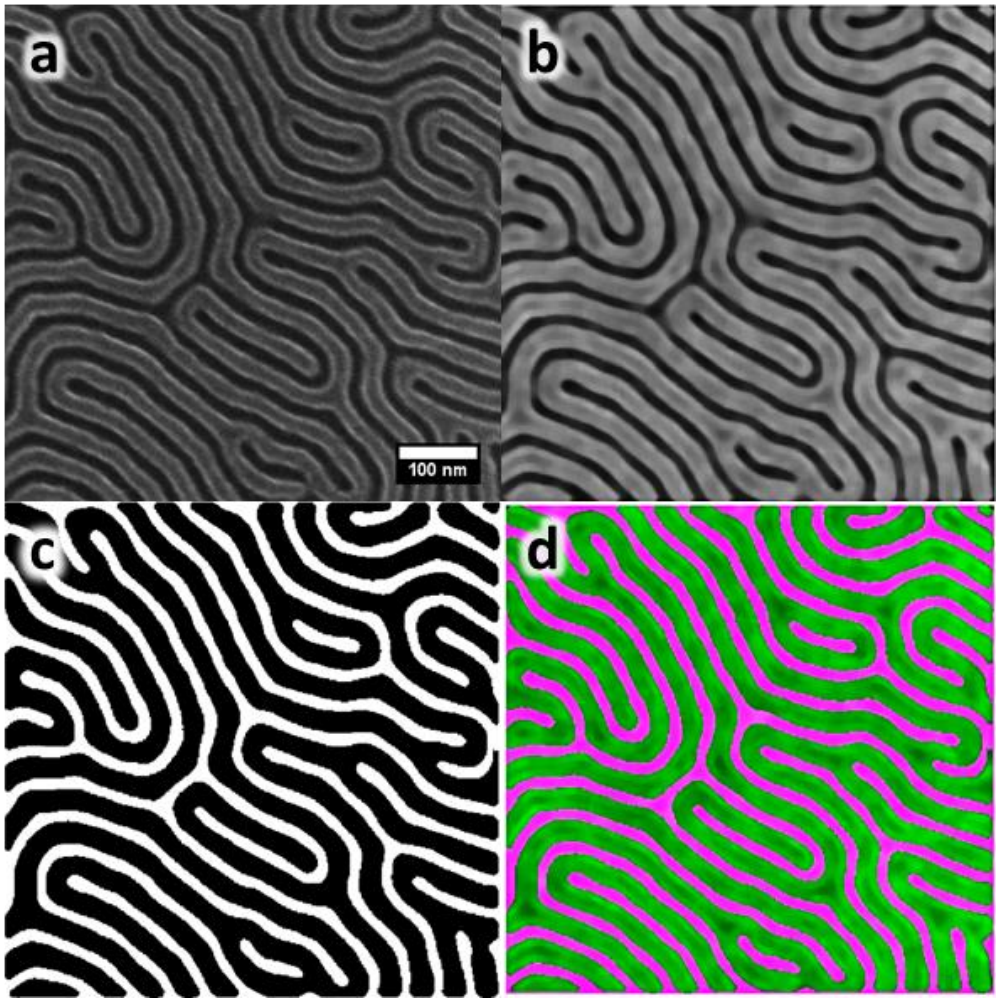


Figure 4.11. Image smoothening and thresholding to binary. a) Input image. b) Smoothened image following background removal and a median filter of size 14nm. c) Binary image after a local Otsu threshold and filtering of latent noise. d) Binary image overlaid on the original image.

Effectively, analysis of the continuous networks formed by lamellar patterns can be achieved by reducing them to skeletons. Skeletonization is a morphological operation where an object is thinned from its boundaries to an unbroken single pixel line which is equidistant from the boundaries, which maintains the connectivity of the network and allows for easier analysis of the structure. This method is has previously been used for the analysis of BCP patterns [31], [67]–[69]. However, the default process in Matlab can often leave "spurs", short branches that are generated from irregularities in the object boundary [70]. An improved method that reduces the incidence of spurs

was developed by Howe [71], based on work by Rumpf and Telea [72], and is implemented here. Both methods are compared in Figure 4.12.

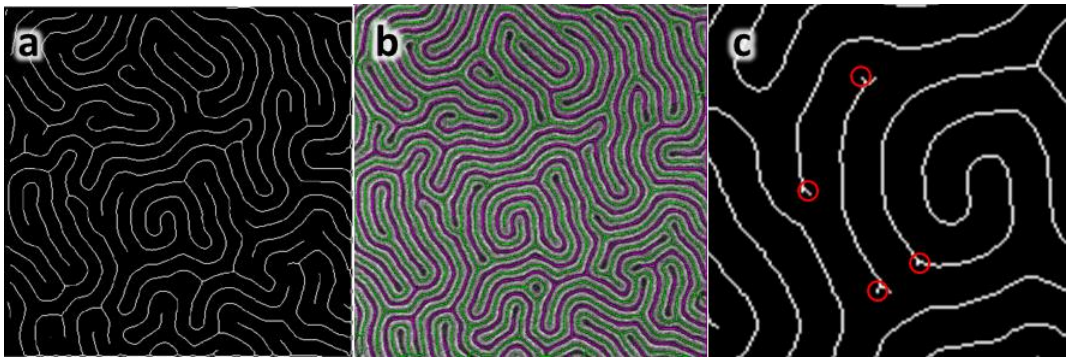


Figure 4.12. Image skeletonization: a) skeletonization using the Howe method, b) skeleton overlaid on the original image, c) skeletonization using the default method, with additional spurs highlighted.

The next step in analysis is the detection and classification of defects. Typical defects present in line patterns are dots, junctions and endpoints. Dots are identified from the binary image by taking objects with an area corresponding to the line width [73]. Objects smaller than this are typically noise from the thresholding process and can be removed, while larger objects are short lines. Junctions and endpoints are then counted by analysing the skeleton [31], [74]. Each pixel on the skeleton is investigated for the number of neighbouring line pixels. Pixels which are part of a line will have 2 neighbouring pixels, whilst endpoints, where a line ends, will only have 1. Junctions, where 2 or more lines meet, will have 3 or more neighbouring pixels. This counting process is illustrated in Figure 4.13. In order to prevent false counting of defects along the image edge, a border of width 50 nm is excluded from the counting.

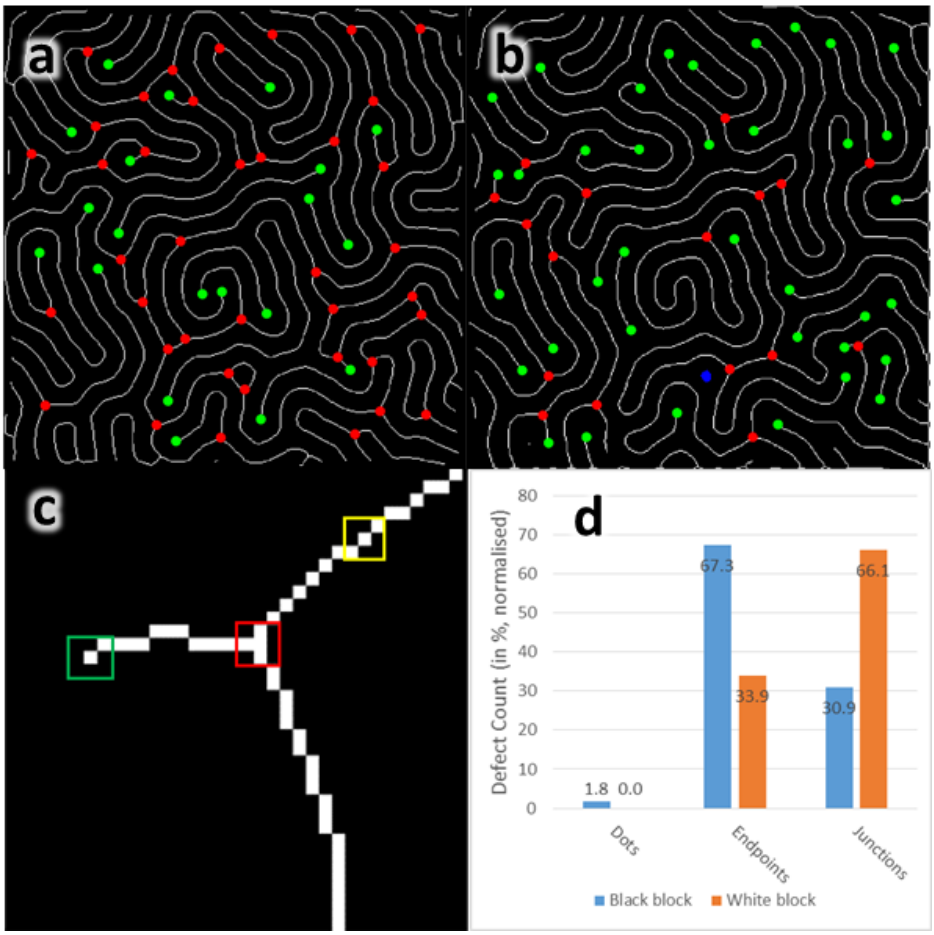


Figure 4.13. Defect analysis performed on skeleton images: a) defects labelled on white block, b) defects labelled on the black block. c) Skeleton pixels representing a junction and endpoint. The yellow box represents points along the line with 2 neighbours, the green box represents an endpoint with only 1 neighbour, and the red box represents a junctions with 3+ connected pixels. d) Normalised values of defect classifications present in each block.

The defect density can then calculated from the sum of dots, junctions and endpoints in the area analysed, as in Equation 4.2 [75].

$$Defect\ Density = \frac{n_{dots}+n_{\text{endpoints}}+n_{\text{junctions}}}{Area} \tag{4.2}$$

To create a complete count of all defects, analysis must be performed on black and white parts of the image. For BCPs, certain classes of defects are block specific, such as dots in the PMMA segment presented here. A dot in one block will have at least

one junction in the corresponding block, however there is not always a correlation between defects making it necessary to investigate both domains.

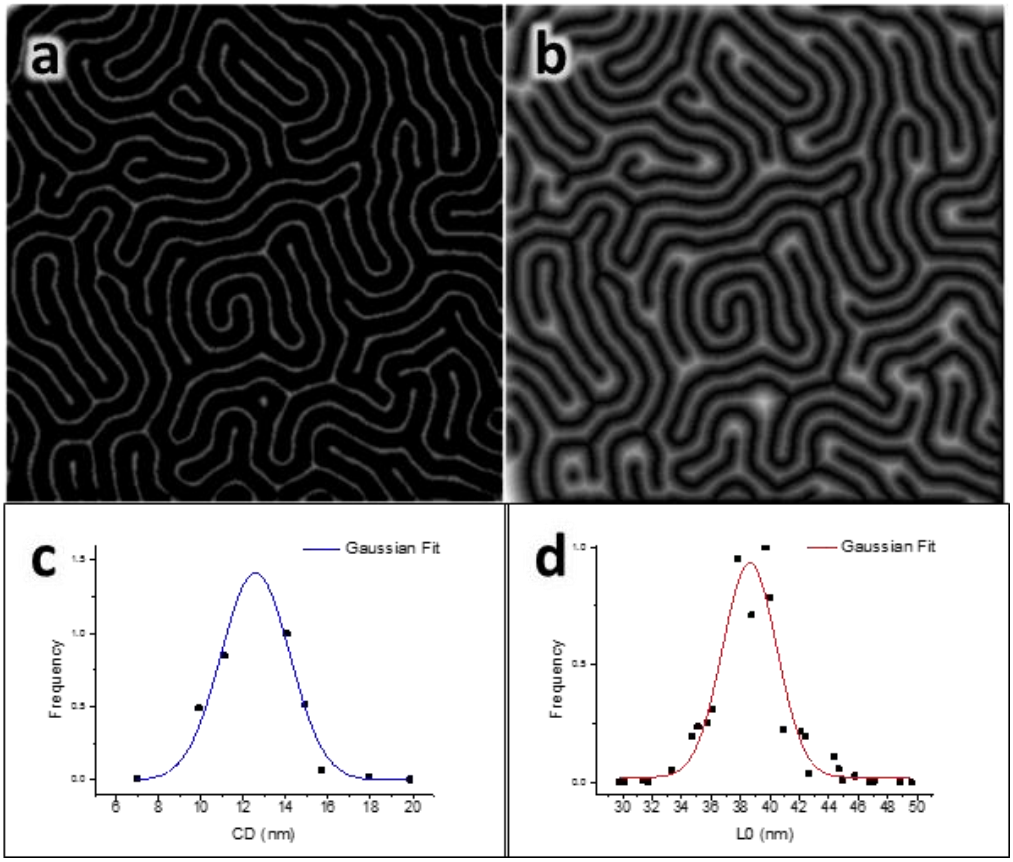


Figure 4.14. Measurement of CD and L_0 a) distance map on the binary image for CD measurement, b) distance map of the skeleton for L_0 measurement, c,d) black CD and L_0 fit to a Gaussian distribution, respectively.

The next piece of data that is determined is the line width (CD) and L_0. This can be achieved using distance transforms. An Euclidean distance transform is applied, generating a distance map of the objects showing the shortest distance across the object at each point [76]. To measure the CD, the distance transform is applied to the binary image. This generates a maxima at the centre of each object which can be read with reference to the skeleton. Areas near the image edge and near defects are removed to eliminate distortions that may exist. To measure the L_0, the same method is applied to the skeleton, giving the Euclidean distance between line centres, see Figure 4.14. As

with defects, this analysis is performed on both of the blocks. While the feature sizes should aggregate to the L_0 and the L_0's should remain the same, large deviations can identify any inconsistences in the analysis which may otherwise be unnoticed.

One of the key challenges to the integration of BCPs into semiconductor fabrication is the issue of line roughness [22], [77]. As feature size shrinks, LWR and LER have become an issue in lithography patterns as these parameters have not scaled with size [78]. Line roughness can result in increased variation in resistance and capacitance, resulting in high failure rates. LWR is typically characterised by the 3σ value, where σ is the standard deviation from the average line width. LER is similarly defined as the deviation in the line edge. The ITRS roadmap requires the LWR to be <8% of the line width to achieve acceptable device performance [79]. For the 15 nm node, the LER requirement is 0.92 nm. While significant work has been undertaken in mitigating roughness in traditional top-down processes [80], [81], the ability of BCP patterns to achieve these benchmarks remains in question [82]. However, continued work in development and optimisation of new BCP systems has shown encouraging progress [83], [84]. To determine the LWR, the 3σ standard deviation can be determined from the distribution shown in Figure 4.14 (c) by statistical analysis. For LER analysis, results reported for top-down fabricated patterns are predominantly straight lines, which can be easily determined using a linear fit. For BCPs, data is typically taken from patterns aligned within patterned substrates which can be analysed similarly. For fingerprint patterns, due to the patterns inherent curvature, linear data is not available, so alternative methods must be explored. Approaches to this issue have previously be demonstrated, Isawa *et al* [85] developed an equation to determine the FER from the LWR.

$$LWR^2 = 2FER^2 \tag{4.3}$$

Murphy *et al* [31] demonstrated an edge-line centre mapping method. Here, both methods are implemented. To create an ideal line for reference, the skeleton is smoothened by a process of dilation and thinning, as shown in Figure 4.15 (a). A distance transform is then applied between the skeleton and the binary object boarder, as with the determination of CD. By taking the standard deviation of the resulting "half-width" measurements, an estimate of the LER is taken.

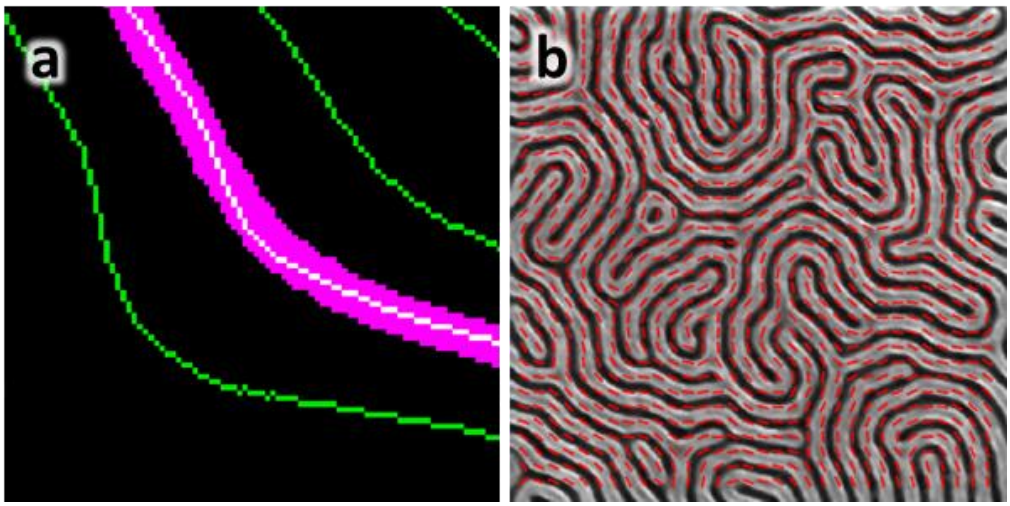


Figure 4.15. a) Skeleton smoothening for LER measurement. The white line represents the original skeleton, the green lines indicate the outline of the line pattern and the pink line shows the smoothened centre line. b) Pattern with orientation map.

The next step is to determine the degree of order within the pattern. To achieve this, a method of determining the orientation within human fingerprints developed by Peter Kovesi was implemented [86]. This method estimates the local orientation at each point, generating an orientation map of the image as shown in Figure 4.15 (b). As with the dot patterns, an orientational parameter can be determined using Equation 4.1, with the reference angle set as the average orientation over the entire image. Finally,

descriptive statistics and images are produced, providing detailed information on the pattern.

4.4.4 Application of Line Analysis

To show the analysis in operation, it was applied to 2 different PS-*b*-PMMA lamellar systems. Recent work has shown the potential of BCP-BCP blends, along with additional additives, as a method of improving BCP patterns, in particular the reduction of defectivity [21], [87], [88]. To investigate this approach, a pure BCP system, L40, and a BCP-BCP blend, L40S, were used. Both systems have a target L_0 of 40 nm. Films were cast on a NL1 brush layer at 1 wt. % and 1.4 wt. % to evaluate the effect of film thickness. Samples were then anneal at 275 °C for 30 minutes, and dry-etched to enhance the contrast during microscopy characterization.

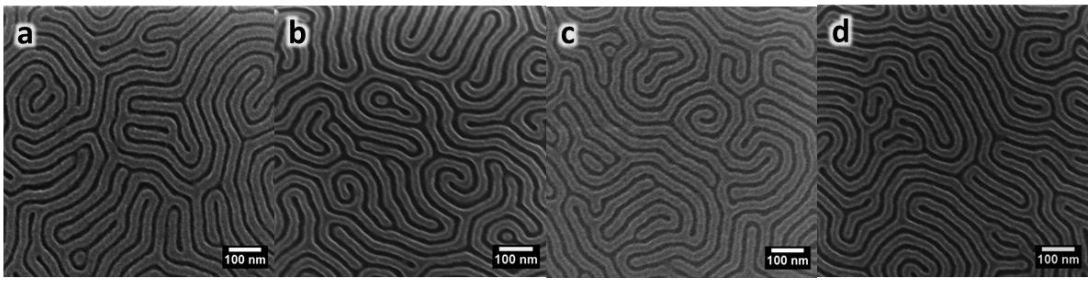


Figure 4.16. Comparison of pure and blend PS-*b*-PMMA: (a, b) L40, and (c, d) L40S cast at 1 wt. % and 1.4 wt. % respectively.

As can be seen in Figure 4.16, the patterns appear quite similar. However, there are important differences as noted in Table 4.5. Here, statistics are averaged over 3 images. It can be seen that the pure BCP L40, when cast at 1.4%, demonstrated notable lower defectivity, LER and variation in line width and period. It is notable however that the blend L40S shows little variation with film thickness, allowing for greater versatility.

Polymer	Wt. %	L_0/nm	L_0 3σ /nm	CD /nm	LWR /nm	LER /nm	Defect /um^2
L40	1%	38.6±0.6	11.0±3.2	27.7±0.4	9.8±3.0	6.3±1.9	90±13
L40	1.4%	39.1±0.2	7.4±0.5	26.7±0.4	6.8±0.4	5.2±1.0	61±14
L40S	1%	39.6±1.1	8.8±1.2	29.1±0.3	8.3±1.5	5.9±0.9	68±1
L40S	1.4%	40.3±1.0	9.6±0.6	27.5±1.6	8.0±0.1	5.8±0.7	62±15

Table 4.5. Details on the uniformity and defectivity of lamellar systems.

An important note for the application of this analysis is the correlation between nanometre-pixel ratio and the measured LWR and LER, see Figure 4.17. Here, the first data point in each group represents a higher magnification (higher resolution) image. This trend is due to the relatively small number of pixels that comprise the width of the line at lower resolutions. Similar trends have been observed in other analytical tools [31].

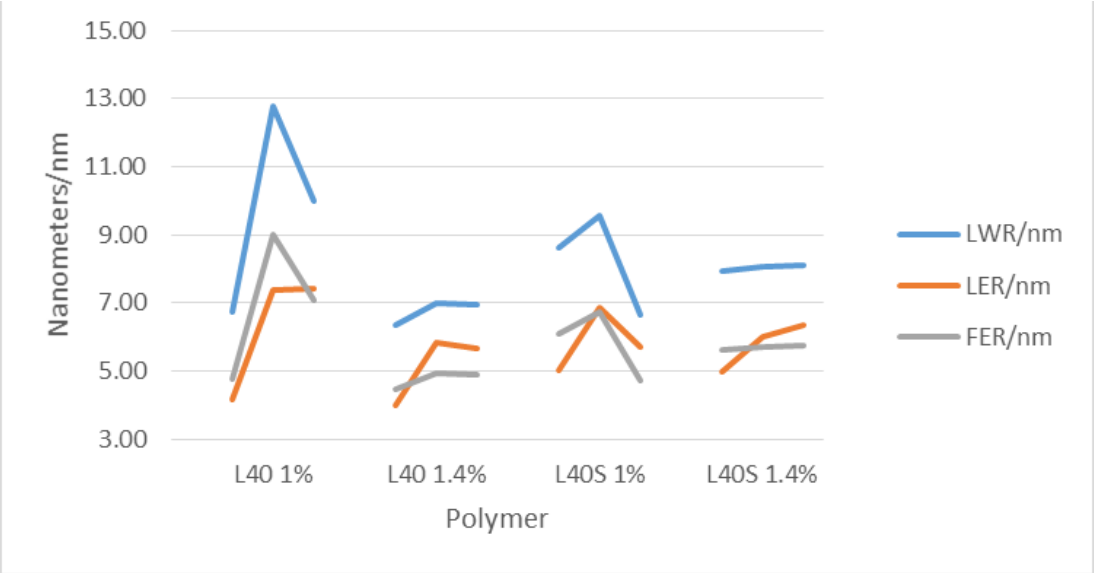


Figure 4.16. Comparison of LWR, LER and FER with nanometre-pixel ratio for each BCP.

4.5 Conclusions

In summary, methods for BCP dot and line pattern analysis have been demonstrated, providing many key metrics to facilitate the future integration of BCPs into industrial fabrication processes. Through the application of innovative and conventional procedures, a robust means of determining defectivity and uniformity was developed. As demonstrated here, applying these methods to two different PS-*b*-PMMA systems allowed for the determination of optimum materials and processes, which will be utilised in future work. It is expected that the robustness and adaptability of this method could aid in the future optimisation and development of BCP systems, as has already been demonstrated elsewhere [89].

4.6 References

[1] M. A. Morris, "Directed self-assembly of block copolymers for nanocircuitry fabrication," *Microelectron. Eng.*, vol. 132, pp. 207–217, 2015.
[2] S. Ji, L. Wan, C. C. Liu, and P. F. Nealey, "Directed self-assembly of block copolymers on chemical patterns: A platform for nanofabrication," *Prog. Polym. Sci.*, vol. 54–55, pp. 76–127, 2016.
[3] A. Nunns, J. Gwyther, and I. Manners, "Inorganic block copolymer lithography," *Polym. (United Kingdom)*, vol. 54, no. 4, pp. 1269–1284, 2013.
[4] A. Noro, Y. Tomita, Y. Shinohara, Y. Sageshima, J. J. Walish, Y. Matsushita, and E. L. Thomas, "Photonic Block Copolymer Films Swollen with an Ionic Liquid," *Macromolecules*, vol. 47, no. 12, pp. 4103–4109, Jun. 2014.
[5] Y. Chan and Y. Mi, "A study of the versatile micropatterns of diblock copolymer micelles: The effect of copolymer concentration, substrate, film thickness and micelles morphology," *Polymer (Guildf).*, vol. 45, no. 10, pp. 3473–3480, 2004.
[6] Y. Kuwahara, S. Kawakami, M. Kubota, K. Matsunaga, K. Nafus, P. Foubert, and M. Mao, "EUV process establishment through litho and etch for N7 node," in *Proc. of SPIE*, 2016, vol. 9776, p. 97760C.
[7] K. Ichimura, K. Yoshida, S. Harada, T. Nagai, M. Kurihara, and N. Hayashi, "HVM readiness of nanoimprint lithography templates: defects, CD, and overlay," vol. 9423, p. 94230D, 2015.
[8] P. Brandt, C. Tranquillin, M. Wieland, S. Bayle, M. Milléquant, and G. Renault, "Alternative stitching method for massively parallel e-beam lithography," in *Proc. of SPIE*, 2015, vol. 9423, p. 942312.
[9] M. C. Smayling, "Lithography alternatives meet design style reality: How do they 'line' up?," in *Proc. of SPIE*, 2016, vol. 9777, p. 977702.
[10] J. Nam, E. S. Kim, D. Kang, H. Yu, K. Kim, S. Yi, C.-H. Shin, and H.-K. Kang,

"Patterning process for semiconductor using directed self assembly," *Proc. SPIE*, vol. 8680, pp. 868011-868011–6, 2013.

[11] H. Pathangi, M. Stokhof, W. Knaepen, V. Vaid, A. Mallik, B. T. Chan, N. Vandenbroeck, J. W. Maes, and R. Gronheid, "Improved cost-effectiveness of the block co-polymer anneal process for DSA," in *Proc. of SPIE*, 2016, vol. 9777, p. 97771Z.

[12] Y.-H. Ting, S.-M. Park, C.-C. Liu, X. Liu, F. J. Himpsel, P. F. Nealey, and A. E. Wendt, "Plasma etch removal of poly(methyl methacrylate) in block copolymer lithography," *J. Vac. Sci. Technol. B Microelectron. Nanom. Struct.*, vol. 26, no. 5, p. 1684, 2008.

[13] T. P. Russell, R. P. Hjelm, and P. A. Seeger, "Temperature dependence of the interaction parameter of polystyrene and poly(methyl methacrylate)," *Macromolecules*, vol. 23, no. 3, pp. 890–893, May 1990.

[14] ITRS, "International technology roadmap for semiconductors: emerging research materials summary," 2013.

[15] C. Tang, E. M. Lennon, G. H. Fredrickson, E. J. Kramer, and C. J. Hawker, "Evolution of Block Copolymer Square Arrays," *Science (80-.).*, vol. 322, no. October, pp. 429–432, 2008.

[16] R. Gronheid, P. Rincon Delgadillo, H. Pathangi, D. Van den Heuvel, D. Parnell, B. T. Chan, Y.-T. Lee, L. Van Look, Y. Cao, Y. Her, G. Lin, R. Harukawa, V. Nagaswami, L. D'Urzo, M. Somervell, and P. Nealey, "Defect reduction and defect stability in IMEC's 14nm half-pitch chemo-epitaxy DSA flow," *Proc. SPIE*, vol. 9049, no. Figure 1, p. 904905, 2014.

[17] A. J. Peters, R. A. Lawson, B. D. Nation, P. J. Ludovice, and C. L. Henderson, "Understanding defects in DSA: calculation of free energies of block copolymer DSA systems via thermodynamic integration of a mesoscale block-copolymer model," in *Proc. of SPIE*, 2014, vol. 9049, no. Md, p. 90492E.

[18] A. Vora, G. Alva, A. Chunder, K. Schmidt, T. Magbitang, E. Lofano, N. Arellano, J. Cheng, and D. P. Sanders, "Synthesis and Thin-film Self-assembly of Cylinder-Forming High-χ Block Copolymers," *J. Photopolym. Sci. Technol.*, vol. 29, no. 5, pp. 685–688, 2016.

[19] C. Sinturel, F. S. Bates, and M. A. Hillmyer, "High χ–Low *N* Block Polymers: How Far Can We Go?," *ACS Macro Lett.*, vol. 4, no. 9, pp. 1044–1050, 2015.

[20] H. Tsai, H. Miyazoe, A. Vora, T. Magbitang, N. Arellano, C.-C. Liu, M. J. Maher, W. J. Durand, S. J. Dawes, J. J. Bucchignano, L. Gignac, D. P. Sanders, E. A. Joseph, M. E. Colburn, C. G. Willson, C. J. Ellison, and M. A. Guillorn, "High chi block copolymer DSA to improve pattern quality for FinFET device fabrication," *Proc. SPIE*, vol. 9779, p. 977910, 2016.

[21] X. Chevalier, P. Coupillaud, G. Lombard, C. Nicolet, J. Beausoleil, G. Fleury, M. Zelsmann, P. Bezard, G. Cunge, J. Berron, K. Sakavuyi, A. Gharbi, R. Tiron, G. Hadziioannou, C. Navarro, and I. Cayrefourcq, "Design of new block copolymer systems to achieve thick films with defect-free structures for applications of DSA into lithographic large nodes," in *Proc. of SPIE*, 2016, vol. 9779, p. 977913.

[22] S. Böhme, C. Girardot, J. Garnier, J. Arias-Zapata, S. Arnaud, R. Tiron, O. Marconot, D. Buttard, and M. Zelsmann, "A route for industry compatible directed self-assembly of high-chi PS-PDMS block copolymers," in *Proc. of SPIE*, 2016, vol. 9777, p. 97771W.

[23] C. Simão, D. Tuchapsky, W. Khunsin, A. Amann, M. A. Morris, and C. M. S.

Torres, “Dimensional and defectivity nanometrology of directed self-assembly patterns,” *Phys. status solidi*, vol. 12, no. 3, pp. 267–270, Mar. 2015.

[24] R. Lundy, S. P. Flynn, C. Cummins, S. M. Kelleher, M. N. Collins, E. Dalton, S. Daniels, M. A. Morris, and R. Enright, “Controlled solvent vapor annealing of a high χ block copolymer thin film,” *Phys. Chem. Chem. Phys.*, vol. 19, no. 4, pp. 2805–2815, 2017.

[25] J. Cheng, R. A. Lawson, W.-M. Yeh, N. D. Jarnagin, L. M. Tolbert, and C. L. Henderson, “PS-b-PHEMA: synthesis, characterization, and processing of a high χ polymer for directed self-assembly lithography,” in *Proc. of SPIE*, 2013, vol. 8680, p. 86801W.

[26] B. A. Garetz, N. P. Balsara, H. J. Dai, Z. Wang, M. C. Newstein, and B. Majumdar, “Orientation Correlations in Lamellar Block Copolymers,” *Macromolecules*, vol. 29, no. 13, pp. 4675–4679, Jan. 1996.

[27] C. Harrison, D. H. Adamson, Z. Cheng, J. M. Sebastian, S. Sethuraman, D. A. Huse, R. A. Register, and P. M. Chaikin, “Mechanisms of Ordering in Striped Patterns,” *Science (80-.).*, vol. 290, no. 5496, pp. 1558–1560, Nov. 2000.

[28] R. A. Segalman, A. Hexemer, R. C. Hayward, and E. J. Kramer, “Ordering and melting block copolymer spherical domains in 2 and 3 dimensions,” *Macromolecules*, vol. 36, no. 9, pp. 3272–3288, 2003.

[29] C. Simão, W. Khunsin, N. Kehagias, M. Salaun, M. Zelsmann, M. a Morris, and C. M. Sotomayor Torres, “Order quantification of hexagonal periodic arrays fabricated by in situ solvent-assisted nanoimprint lithography of block copolymers.,” *Nanotechnology*, vol. 25, no. 17, p. 175703, 2014.

[30] X. Zhang, K. D. Harris, N. L. Y. Wu, J. N. Murphy, and J. M. Buriak, “Fast Assembly of Ordered Block Copolymer Nanostructures through Microwave Annealing,” *ACS Nano*, vol. 4, no. 11, pp. 7021–7029, Nov. 2010.

[31] J. N. Murphy, K. D. Harris, and J. M. Buriak, “Automated defect and correlation length analysis of block copolymer thin film nanopatterns,” *PLoS One*, vol. 10, no. 7, pp. 1–32, 2015.

[32] R. Harukawa, M. Aoki, A. Cross, V. Nagaswami, S. Kawakami, T. Yamauchi, T. Tomita, S. Nagahara, M. Muramatsu, and T. Kitano, “Defect analysis methodology for contact hole grapho epitaxy DSA,” in *Proc. of SPIE*, 2014, vol. 9050, p. 905027.

[33] C. Ito, S. Durant, S. Lange, R. Harukawa, T. Miyagi, V. Nagaswami, P. Rincon Delgadillo, R. Gronheid, and P. Nealey, “Inspection of directed self-assembly defects,” in *Proc. of SPIE*, 2014, vol. 9049, no. Cd, p. 90492D.

[34] P. A. R. Delgadillo, R. Gronheid, C. J. Thode, H. Wu, Y. Cao, M. Somervell, K. Nafus, and P. F. Nealey, “All track directed self-assembly of block copolymers: process flow and origin of defects,” *Altern. Lithogr. Technol. IV*, vol. 8323, p. 83230D (9 pp.), 2012.

[35] R. A. Farrell, E. R. Hosler, G. M. Schmid, J. Xu, M. E. Preil, V. Rastogi, N. Mohanty, K. Kumar, M. J. Cicoria, D. R. Hetzer, and A. DeVilliers, “Manufacturability considerations for DSA,” in *Proc. of SPIE*, 2014, vol. 9051, p. 90510Z.

[36] A. Gharbi, R. Tiron, P. Pimenta Barros, M. Argoud, I. Servin, X. Chevalier, C. Nicolet, and C. Navarro, “PMMA removal options by wet development in PS-b-PMMA block copolymer for nanolithographic mask fabrication,” *J. Vac. Sci. Technol. B, Nanotechnol. Microelectron. Mater. Process. Meas. Phenom.*, vol. 33, no. 5, p. 51602, 2015.

[37] D. Borah, M. T. Shaw, S. Rasappa, R. A. Farrell, C. O'Mahony, C. M. Faulkner, M. Bosea, P. Gleeson, J. D. Holmes, and M. A. Morris, "Plasma etch technologies for the development of ultra-small feature size transistor devices," *J. Phys. D. Appl. Phys.*, vol. 44, no. 17, p. 174012, May 2011.

[38] C. Fang, A. Vaglio Pret, M. D. Smith, J. J. Biafore, S. A. Robertson, and J. Bekaert, "Understanding the impact of CD-SEM artifacts on metrology via experiments and simulations," vol. 9424, p. 94242A, 2015.

[39] S. D. O'Connor, R. C. Gamble, R. K. Eby, and J. D. Baldeschwieler, "Noise reduction in atomic force microscopy: Resonance contact mode," *Rev. Sci. Instrum.*, vol. 67, no. 2, pp. 393–396, 1996.

[40] I. Guillamón, R. Córdoba, J. Sesé, J. M. De Teresa, M. R. Ibarra, S. Vieira, and H. Suderow, "Enhancement of long-range correlations in a 2D vortex lattice by an incommensurate 1D disorder potential," *Nat. Phys.*, vol. 10, no. 11, pp. 851–856, 2014.

[41] S. Collins, I. W. Hamley, and T. Mykhaylyk, "An atomic force microscopy study of ozone etching of a polystyrene/polyisoprene block copolymer," *Polymer (Guildf).*, vol. 44, no. 8, pp. 2403–2410, 2003.

[42] E. Arias-Castro and D. L. Donoho, "Does median filtering truly preserve edges better than linear filtering?," *Ann. Stat.*, vol. 37, no. 3, pp. 1172–1206, Jun. 2009.

[43] C. Tomasi and R. Manduchi, "Bilateral filtering for gray and color images," in *IEEE International Conference on Computer Vision*, 1998, pp. 839–846.

[44] D. Lanman, "Bilateral Filtering," 2006. [Online]. Available: https://uk.mathworks.com/matlabcentral/fileexchange/12191-bilateral-filtering. [Accessed: 12-Feb-2014].

[45] H. Winnemöller, S. C. Olsen, and B. Gooch, "Real-time video abstraction," in *Proceedings of ACM SIGGRAPH*, 2006, vol. 25, no. 3, pp. 1221–1226.

[46] M. R. Hammond, S. W. Sides, G. H. Fredrickson, E. J. Kramer, J. Ruokolainen, and S. F. Hahn, "Adjustment of block copolymer nanodomain sizes at lattice defect sites," *Macromolecules*, vol. 36, no. 23, pp. 8712–8716, 2003.

[47] C.-C. Liu, G. S. W. Craig, H. Kang, R. Ruiz, P. F. Nealey, and N. J. Ferrier, "Practical implementation of order parameter calculation for directed assembly of block copolymer thin films," *J. Polym. Sci. Part B Polym. Phys.*, vol. 48, no. 24, pp. 2589–2603, Dec. 2010.

[48] T. J. Atherton and D. J. Kerbyson, "Size invariant circle detection," *Image Vis. Comput.*, vol. 17, no. 11, pp. 795–803, 1999.

[49] H. K. Yuen, J. Princen, J. Dlingworth, and J. Kittler, "A Comparative Study of Hough Transform Methods for Circle Finding," in *Procedings of the Alvey Vision Conference 1989*, 1989, vol. 8, no. 1, pp. 169–174.

[50] C. Harrison, D. E. Angelescu, M. Trawick, Z. Cheng, D. A. Huse, P. M. Chaikin, D. A. Vega, J. M. Sebastian, R. A. Register, and D. H. Adamson, "Pattern coarsening in a 2D hexagonal system," *Europhys. Lett.*, vol. 67, no. 5, pp. 800–806, Sep. 2004.

[51] S. Ji, C. C. Liu, W. Liao, A. L. Fenske, G. S. W. Craig, and P. F. Nealey, "Domain orientation and grain coarsening in cylinder-forming poly(styrene-b-methyl methacrylate) films," *Macromolecules*, vol. 44, no. 11, pp. 4291–4300, 2011.

[52] H. O. Thomas and P. Marchand, *Graphics and GUIs with MATLAB*, 3rd ed. Chapman and Hall/CRC, 2002.

[53] P. W. Majewski and K. G. Yager, "Millisecond Ordering of Block Copolymer Films via Photothermal Gradients," *ACS Nano*, vol. 9, no. 4, pp. 3896–3906, Apr. 2015.
[54] B. C. Berry, A. W. Bosse, J. F. Douglas, R. L. Jones, and A. Karim, "Orientational order in block copolymer films zone annealed below the order-disorder transition temperature," *Nano Lett.*, vol. 7, no. 9, pp. 2789–2794, 2007.
[55] A. P. Marencic, M. W. Wu, R. A. Register, and P. M. Chaikin, "Orientational order in sphere-forming block copolymer thin films aligned under shear," *Macromolecules*, vol. 40, no. 20, pp. 7299–7305, 2007.
[56] V. Zwetkoff, "No Title," *Acta Physicoch*, vol. 10, no. 557. 1939.
[57] C. Zannoni, "Quantitative Description of Orientational Order: Rigid Molecules," in *Nuclear Magnetic Resonance of Liquid Crystals*, J. W. Emsley, Ed. Dordrecht: Springer Netherlands, 1985, pp. 1–34.
[58] P. W. Majewski and K. G. Yager, "Rapid ordering of block copolymer thin films.," *J. Phys. Condens. Matter*, vol. 28, no. 40, p. 403002, 2016.
[59] K. W. Guarini, C. T. Black, and S. H. I. Yeung, "Optimization of diblock copolymer thin film self assembly," *Adv. Mater.*, vol. 14, no. 18, pp. 1290–1294, 2002.
[60] R. Guo, E. Kim, J. Gong, S. Choi, S. Ham, and D. Y. Ryu, "Perpendicular orientation of microdomains in PS-b-PMMA thin films on the PS brushed substrates," *Soft Matter*, vol. 7, no. 15, p. 6920, 2011.
[61] G. Claveau, P. Quemere, M. Argoud, J. Hazart, P. P. Barros, A. Sarrazin, N. Posseme, R. Tiron, X. Chevalier, C. Nicolet, and C. Navarro, "Surface affinity role in graphoepitaxy of lamellar block copolymers," *J. Micro/Nanolithography, MEMS, MOEMS*, vol. 15, no. 3, p. 31604, Aug. 2016.
[62] D. Antonioli, K. Sparnacci, M. Laus, F. F. Lupi, T. J. Giammaria, G. Seguini, M. Ceresoli, M. Perego, and V. Gianotti, "Neutral wetting brush layers for block copolymer thin films using homopolymer blends," in *AIP Conference Proceedings*, 2016, vol. 1736, p. 20169.
[63] D. Borah, M. Ozmen, S. Rasappa, M. T. Shaw, J. D. Holmes, and M. A. Morris, "Molecularly functionalized silicon substrates for orientation control of the microphase separation of PS-b-PMMA and PS-b-PDMS block copolymer systems," *Langmuir*, vol. 29, no. 9, pp. 2809–2820, 2013.
[64] A. P. Fitz and R. J. Green, "Fingerprint classification using a Hexagonal Fast Fourier Transform," *Pattern Recognit.*, vol. 29, no. 10, pp. 1587–1597, 1996.
[65] N. Otsu, "A Threshold Selection Method from Gray-Level Histograms," *IEEE Trans. Syst. Man. Cybern.*, vol. 9, no. 1, pp. 62–66, Jan. 1979.
[66] D. Bradley and G. Roth, "Adaptive Thresholding using the Integral Image," *J. Graph. Tools*, vol. 12, no. 2, pp. 13–21, Jan. 2007.
[67] C. Harrison, Z. Cheng, S. Sethuraman, D. A. Huse, P. M. Chaikin, D. A. Vega, J. M. Sebastian, R. A. Register, and D. H. Adamson, "Dynamics of pattern coarsening in a two-dimensional smectic system," *Phys. Rev. E - Stat. Nonlinear, Soft Matter Phys.*, vol. 66, no. 1, pp. 1–27, 2002.
[68] I. P. Campbell, S. Hirokawa, and M. P. Stoykovich, "Processing approaches for the defect engineering of lamellar-forming block copolymers in thin films," *Macromolecules*, vol. 46, no. 24, pp. 9599–9608, 2013.
[69] M. Salaün, M. Le Gallic, E. Picard, and M. Zelsmann, "In-situ visualization and order quantification of symmetric diblock copolymer directed self-assembly," *Thin Solid Films*, vol. 543, pp. 148–152, 2013.

[70] R. C. Gonzalez, R. E. Woods, and S. L. Eddins, *Digital Image Processing Using Matlab*, 1st ed. Upper Saddle River, NJ: Prentice-Hall, Inc., 2003.
[71] N. Howe, "Better Skeletonization," 2007. [Online]. Available: http://uk.mathworks.com/matlabcentral/fileexchange/11123-better-skeletonization. [Accessed: 14-May-2014].
[72] M. Rumpf and A. Telea, "A Continuous Skeletonization Method Based on Level Sets," *Jt. EUROGRAPHICS-IEEE TCVG Symp. Vis.*, pp. 151–157, 2002.
[73] K. G. Yager, E. Lai, and C. T. Black, "Self-assembled phases of block copolymer blend thin films," *ACS Nano*, vol. 8, no. 10, pp. 10582–10588, 2014.
[74] I. Arganda-Carreras, R. Fernández-González, A. Muñoz-Barrutia, and C. Ortiz-De-Solorzano, "3D reconstruction of histological sections: Application to mammary gland tissue," *Microsc. Res. Tech.*, vol. 73, no. 11, pp. 1019–1029, Oct. 2010.
[75] C. Simão, D. Tuchapsky, W. Khunsin, A. Amann, M. A. Morris, and C. M. Sotomayor Torres, "Defect analysis and alignment quantification of line arrays prepared by directed self-assembly of a block copolymer," *Proc. SPIE*, vol. 9050, p. 905028, 2014.
[76] C. R. Maurer, Rensheng Qi, and V. Raghavan, "A linear time algorithm for computing exact Euclidean distance transforms of binary images in arbitrary dimensions," *IEEE Trans. Pattern Anal. Mach. Intell.*, vol. 25, no. 2, pp. 265–270, Feb. 2003.
[77] D. B. Millward, G. S. Lugani, R. Khurana, S. L. Light, A. Niroomand, P. D. Hustad, P. Trefonas, S. Chang, C. N. Lee, and D. Quach, "A comparison of the pattern transfer of line-space patterns from graphoepitaxial and chemoepitaxial block co-polymer directed self-assembly," in *Proc. of SPIE*, 2014, vol. 9054, p. 90540M.
[78] G. F. Lorusso, H. Yang, A. Azordegan, T. Dibiase, and K. Corporation, "Automating Investigation of Line Width Roughness," *Yield Management Solutions*, vol. 8, no. 1, pp. 49–55, 2006.
[79] ITRS, "International Technology Roadmap for Semiconductors: Metrology Summary," 2015.
[80] T. Y. Ma, P. Xie, L. Godet, P. M. Martin, C. S. Campbell, J. Xue, L. Miao, Y. Chen, H. Dai, C. Bencher, and C. S. Ngai, "Post-litho line edge/width roughness smoothing by ion implantations," in *Proc. of SPIE*, 2013, vol. 8682, p. 868206.
[81] J. Jussot, E. Pargon, B. Icard, J. Bustos, and L. Pain, "Line width roughness reduction strategies for patterns exposed via electron beam lithography," in *Proceedings of SPIE*, 2014, vol. 9, no. 1, p. 905405.
[82] D. B. Millward, G. S. Lugani, S. L. Light, A. Niroomand, P. D. Hustad, P. Trefonas, D. Quach, and V. V. Ginzburg, "Graphoepitaxial and chemoepitaxial methods for creating line-space patterns at 33nm pitch: comparison to a HVM process," vol. 9423, p. 942304, 2015.
[83] C. Navarro, C. Nicolet, F. Ariura, X. Chevalier, K. Xu, M. A. Hockey, M. Mumtaz, G. Fleury, G. Hadziioannou, A. Legrain, M. Zelsmann, A. Gharbi, R. Tiron, L. Pain, L. Evangelio, M. Fernandez-Regulez, F. Perez-Murano, and I. Cayrefourcq, "Recent Achievements in Sub-10 nm DSA Lithography for Line/Space Patterning," *J. Photopolym. Sci. Technol.*, vol. 30, no. 1, pp. 69–75, 2017.
[84] M. Somervell, T. Yamauchi, S. Okada, T. Tomita, T. Nishi, S. Kawakami, M. Muramatsu, E. Iijima, V. Rastogi, T. Nakano, F. Iwao, S. Nagahara, H. Iwaki,

M. Dojun, K. Yatsuda, T. Tobana, A. Romo Negreira, D. Parnell, B. Rathsack, K. Nafus, J. Peyre, and T. Kitano, "Driving DSA into volume manufacturing," in *proc*, 2015, vol. 9425, p. 94250Q.

[85] M. Isawa, K. Sakai, P. A. Rincon Delgadillo, R. Gronheid, and H. Yoshida, "Line edge roughness measurement technique for fingerprint pattern in block copolymer thin film," in *27th Conference on Metrology, Inspection, and Process Control for Microlithography*, 2013, vol. 8681, p. 868114.

[86] P. Kovesi, "MATLAB and Octave Functions for Computer Vision and Image Processing." [Online]. Available: http://www.peterkovesi.com/matlabfns. [Accessed: 12-Feb-2014].

[87] X. Chevalier, C. Nicolet, A. Gharbi, P. Pimenta-Barros, R. Tiron, G. Fleury, G. Hadziioannou, I. Iliopoulos, and C. Navarro, "Blending approaches to enhance structural order in block-copolymer's self-assemblies," in *Proc. of SPIE*, 2015, vol. 9425, p. 94251N.

[88] T. Matsumiya, T. Kurosawa, M. Yahagi, H. Yamano, K. Miyagi, T. Maehashi, I. Suzuki, A. Kawaue, Y. Komuro, T. Hirayama, and K. Ohmori, "Block co-polymer approach for CD uniformity and placement error improvement in DSA hole grapho-epitaxy process," in *Proc. of SPIE*, 2015, vol. 9425, p. 942517.

[89] P. Mokarian-Tabari, R. Senthamaraikannan, C. Glynn, T. W. Collins, C. Cummins, D. Nugent, C. O'Dwyer, and M. A. Morris, "Large Block Copolymer Self-Assembly for Fabrication of Subwavelength Nanostructures for Applications in Optics," *Nano Lett.*, vol. 17, no. 5, pp. 2973–2978, May 2017.

Chapter 5

Large Block Copolymer Self-Assembly for Fabrication of Subwavelength Nanostructures for Applications in Optics

5.1 Abstract

Nanostructured surfaces are common in nature and exhibit properties such as antireflectivity (moth eyes), self-cleaning (lotus leaf), iridescent colours (butterfly wings) and water harvesting (desert beetles). We now understand these properties and can mimic some of these natural structures in the laboratory. However, these synthetic structures are limited since they are not easily mass produced over large areas due to the limited scalability of current technologies such as UV-lithography, the high cost of infrastructure and the inability to pattern non-planar surfaces. Here, we report a solution process based on block copolymer self-assembly to fabricate sub-wavelength structures on large areas of optical and curved surfaces with feature size and spacing designed to efficiently scatter visible light. SiNPs with diameters of ~115 ± 19 nm, periodicity of 180 ± 18 nm and aspect ratio of 2-15 show a reduction in reflectivity by a factor of 100, < 0.16% between 400-900 nm at AOI 30°. Significantly, the reflectivity remains below 1.75% up to incident angles of 75°. Modelling the efficiency of a SiNP PV suggests a 24.6% increase in efficiency - representing a 3.52% (absolute) or 16.7% (relative) increase in electrical energy output from the PV system compared to the AR-coated device.

5.2 Introduction

BCP self-assembly is a potential solution based process that could offer an alternative route to produce highly ordered photonic crystal structures. However, BCP efforts have been limited to sub-100 nm spacing/feature sizes limiting their application in optics industry. BCPs generally form nanodomains of 5-100 nm due to microphase separation of the incompatible constituent blocks. The size and structural arrangement of the domains can be customized by the molecular weight and volume fraction of the blocks. These BCP derived nanostructures have been employed for the fabrication of

1D photonic crystals [1], [2] based on lamellar systems, to 2D [3] and 3D structures based on bicontinuous gyroid structures [4], photonic gels [5], [6], moth-eye structures [7], higher luminescent LEDs [8], antireflective coatings [9] some with improved self-cleaning properties [10] and metamaterials [11], [12]. However, advancing the technology beyond 1D and 2D photonic crystals for manipulation of visible light has been challenging [13]. In order to modulate photons in the visible and near-infrared light range (400-1500 nm), lateral pattern feature/domain sizes must ensure a periodicity, graded index and aspect ratio that minimizes broadband reflectivity, and ideally maintain reflectivity suppression so the effect is omnidirectional. The diameter of the features being subwavelength strongly affect reflectivity (close to quarter wavelength, but not prescriptively so). The smaller features do not supress the reflectivity as much as the larger features do. See Figure S5.7.1. There is thought to be an 'inherent size limitation' in BCP self-assembly due to significant kinetic penalties that arise from higher molecular entanglement in ultra-high molecular weight polymers (>500 kg/mol), requiring a very long annealing time [14], [15]. Furthermore, synthesising ultra-high molecular weight BCPs above 500,000 kg/mol of the required monodispersity remains very challenging [15], [16]. Alternative strategies to increase domain dimensions such as adding homopolymers [17] and swelling the domains with ionic liquid [18] have been explored, but they introduce defects, segregation or simply do not go beyond 100 nm limit. This work addresses the critical element of the work extending the size limitations of BCPs from the sub-20 nm range (as developed for semiconductor fabrication) to 100 nm [16] and toward dimension ranges expected for techniques applicable to the optics industry. Here, we exploit commercially available block copolymers to generate periodic hexagonal domain structures with average cylinder diameter of 115 nm and the inter cylinder spacing (L0) of greater than 160

nm, and use these masks to make nanopillars of high aspect ratio for fabrication of omnidirectional broadband antireflective surfaces. We show our 870 nm tall SiNPs with a tapered structure and height: width aspect ratio >10, supress reflectivity more than 2 orders of magnitude, and from 34% to 0.16% in the range of visible light. To date, we believe this is the minimum reflectance of nanotextured Si made by BCPs [19], [20] and comparable with other methods rivalling black silicon [21]. Also as we show here, this method has the potential to be used for patterning curved surfaces.

5.3 Experimental

5.3.1 Film preparation.

The polymer was dissolved in a toluene: tetrahydrofuran (THF) (80:20) mixture to yield from 0.5 wt. % to 3.0 wt. % solutions and left stirring for 2 h to ensure complete dissolution. BCP films were prepared by spin coating the polymer solution onto the substrates at 4500 rpm for 30 s. Following deposition, the PS-*b*-P2VP films were exposed to solvent mixtures of THF: $CHCl_3$ with volume ratio of 2:1, for an hour at room temperature. Solvent annealing was carried out in the conventional manner with two small vials containing 2 mL THF and 1 mL $CHCl_3$ placed inside a glass jar with volume of approximately 150 mL, along with the BCP sample. Phase separated BCP thin film were reconstructed by exposing the film to ethanol vapour at 40 °C for 45 minutes. A 0.8 wt. % of iron nitrate ethanolic solution was spin cast on silicon substrate as reported previously [22]. For glass and GaN substrates, and to achieve superior etch contrast, a 2 wt. % of nickel nitrate ethanolic solution was deposited on the film. UV/Ozone treatment (Novascan PSD series) was used to oxidize the precursor and remove the matrix polymer.

5.3.2 Pattern transfer.

Iron oxide nanodots fabricated on substrate surface from BCP template were used as an etch mask for pattern transfer. The silicon etch was performed using C_4F_8 (90 sccm) and SF6 (30 sccm) gases for various duration of time with an inductively coupled plasma (ICP) and reactive ion etching (RIE) powers of 600 W and 15 W, respectively, at 2.0 Pa with a helium backside cooling pressure of 1.3 kPa to transfer the patterns into the underlying substrate. The GaN etch was performed using CH_4 (5 sccm), H_2 (15 sccm) and Ar (25 sccm) gases for desired time with ICP and RIE powers of 500 W and 45 W. The glass etch was performed using Ar (45 sccm) and SF_6 (5 sccm) gasses for 2 min etch time with ICP and RIE powers of 900 W and 100 W, respectively. The etching process was accomplished in an OIPT Plasmalab System100 ICP180 etch tool. Figure S5.7.4 shows the schematic of the steps for the fabrication of nanopillars.

5.3.3 Optical analysis.

Angle-resolved optical characterization was conducted using an in-house constructed cage-mounted optical reflectance/transmission spectroscopy setup. The reflectivity was obtained at variable AOI using a rotating sample stage and collection arm with constant path length. Samples were illuminated with a white Halogen bulb collimated to a beam diameter of ~ 1 - 2 mm. UV-Vis-NIR spectra of the reflected light was collected using collimation and focusing optics to two Oceanoptics spectrometers, a USB2000+ and a NIRQuest256-2.5, with optical resolutions of 1.5 nm and 9.5 nm respectively. Reference spectra were acquired using an Au mirror (ThorLabs gold mirror PF10-03-M01) at each AOI investigated prior to sample data collection under identical conditions.

5.3.4 Dimensional analysis.

The analysis of the patterns was performed using an in-house algorithm based on the circular Hough transform and Delaunay triangulation. The extracted dimensions were fitted to a Gaussian plot to record the mean and deviation. This methodology allows us to finely measure dimensional information such as cylinder diameter and centre to centre distance (L_0) to monitor the block copolymer patterns. More information is provided in Figure S5.7.6.

5.3.5 3D model.

Representative 3D models were created in "Rhinoceros 5" modelling software. The profile from cross-sectional STEM images was combined with position and outlines from AFM images to form three dimensional polysurfaces. The model was then colourised to show the layers of materials.

5.3.6 Microscopy.

Atomic Force Microscope (SPM, Park systems, XE-100) was operated in AC (tapping) mode under ambient conditions using silicon microcantilever probe tips with a force constant of 42 N m^{-1}. Topographic and phase images were recorded simultaneously. SEM images were obtained by a high resolution (<1 nm) Field Emission Zeiss Ultra Plus-SEM with a Gemini column operating at an accelerating voltage of 5 kV. The scanning transmission electron microscope (STEM) lamella specimen were prepared by the Zeiss Auriga-FIB (Carl Zeiss Microscopy Ltd.) with a Cobra ion column having a unique 2.5 nm resolution and were analysed by FEI Titan-TEM operating at an accelerating voltage of 200 kV.

5.3.7 Simulation.

Optical reflectivities are simulated using the "Grating Diffraction Calculator" (GD-Calc®), an electromagnetic simulation program that computes diffraction efficiencies of optical grating structures, including biperiodic gratings. The program's capabilities include a general and flexible grating modelling facility, structure parameterization (with any number of parameters), and unrestricted control over diffraction order selection. Periodic gratings are "block-structured" (or must be defined approximately in terms of a block structured representation), meaning that the grating comprises optically homogeneous regions whose bounding surfaces are planes parallel to a set of primary coordinate planes. Moth eye-type structures are simulated as truncated cones with upper and lower diameters based on the measured structures.

5.4 Results and Discussion

5.4.1 Nanopattern Formation and BCP Characterization.

A highly periodic BCP pattern was made using commercially available polystyrene-*block*-poly(2-vinylpyridine) (PS-*b*-P2VP) with molecular weight of about 800 kg/mol, phase separating into cylinders with diameter of 115±19 nm, and periodicity of 180±18 nm on Si, GaN and glass (Figure 5.1(a-c)). Figures 5.1(d-f) show the top-down SEM images of various nanopillars with an excellent coverage over large substrate areas after pattern transfer. The expected very slow kinetics for ordered microphase separation of high molecular weight BCPs were not observed, and solvent annealing for an hour (THF/$CHCl_3$ at room temperature) led to the formation of highly ordered hexagonally packed domain patterns of feature size > 100 nm. Due to slow reptation of the ultra-high molecular BCP chain (Mw>500 kg/mol), this is a highly unexpected observation. To the best of our knowledge, to achieve a highly ordered pattern in the range of molecular weight used here (i.e. 800 kg/mol) either requires

hours [14], [15] and weeks [1], [13] of annealing at higher temperatures or involves special polymerization methods [23]. Most probably, the system seems likely to have been trapped in a kinetically metastable phase within the thin film. We suggest that a meta-stable hexagonally perforated lamellar (HPL) phase is formed in these thin films due to a confinement effect as seen also in other systems [24]. Longer annealing durations (2-24 hours) do result in either a reduction or complete loss of order in the pattern (see Figure S5.7.2), while the film remains intact on the substrate (i.e. no dewetting is observed). This suggests the original phase separated pattern was possibly a non-equilibrium phase rather than an equilibrium state. However, this might be an overly simplistic view as recent papers have shown that solvent annealing is a complex process with kinetic and thermodynamic limitations that might enable more rapid ordered microphase separation than expected [25]–[27]. To obtain more insight about the internal structure of the film, FIB-lamella cross section TEM and STEM was performed on the polymer film after solvent annealing. Substrates were stained with RuO_4 for PS (Figure 5.2b), and iodine (Figure 5.2c) for P2VP to enhance the contrast between PS and P2VP domains for imaging. Figure 5.2a shows a STEM-EDX elemental map of the features in the iodine stained film. Figure 5.2c shows a perforated structure suggesting the formation of a HPL phase with stacking layers of the ABC type (since the centre of the cylinders in the first layer is offset against the lower layer (Figure 5.2d). A 3D modelling of the structure for visualisation is presented in Figure 5.2e. A video of the modelled structure is available (Figure S5.7.3). We have studied a wide range of film thickness from 25 to 500 nm with solvent annealing time of 1-24 h (see Figure S5.7.2). The best result is mostly achieved at a narrow window of thickness close to the pitch of 165 nm and within an hour of exposure to THF and $CHCl_3$ with ratio of (2:1).

5.4.2 Optical Characterization.

The BCP template in (Figure 5.1a) was used as a mask to make SiNPs with aspect ratio of 2-15 and with heights up to 1150 nm. As a proof of concept a BK7 convex lens with diameter of 3.2 cm was also patterned by BCPs (Figure S5.7.4). The subwavelength patterns made by BCP self-assembly were transferred to a number of electronic, industrial and optoelectronic substrates such as Si, glass and GaN after metal oxide inclusion [22] and by plasma etch. Figure 5.3 shows the average reflectivity of our "super tall" SiNPs with apex and base diameter of 70 and 130 nm respectively and height of 870 nm within the angle of incidence range of 30-75°.

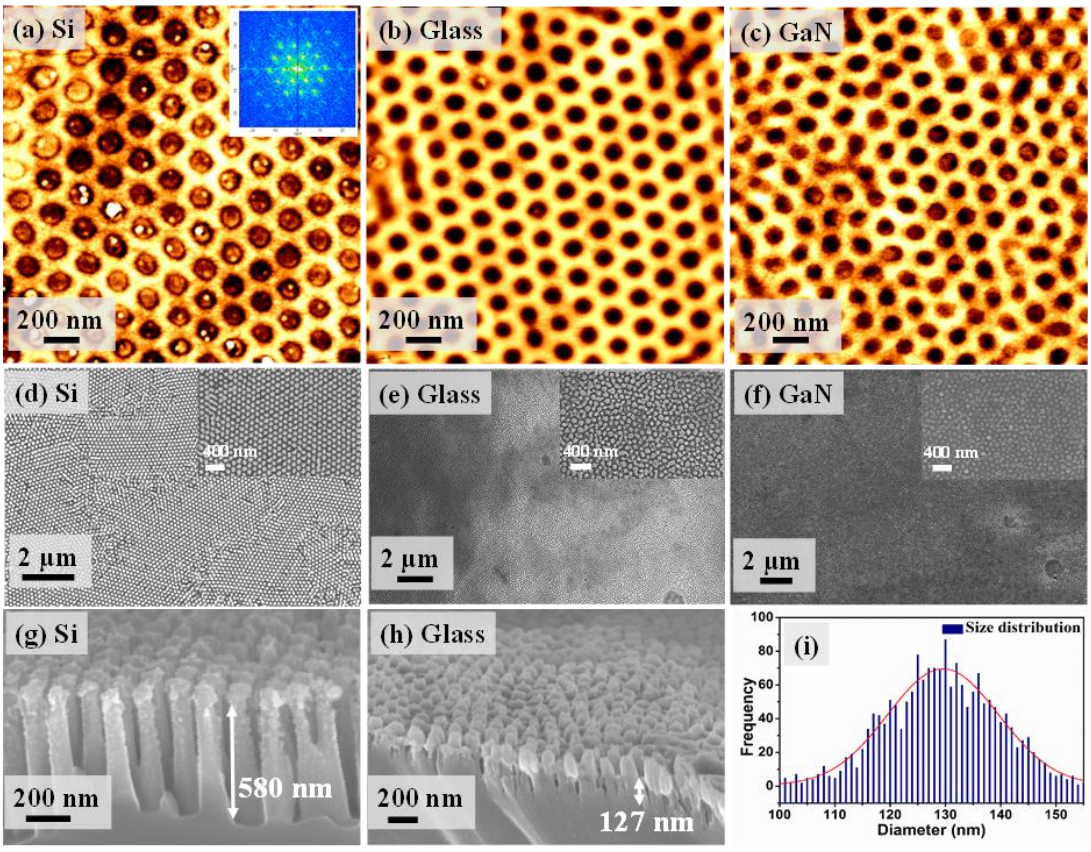


Figure 5.1. Large domain (diameter >100 nm) of (PS-*b*-P2VP) on optical surfaces. AFM topography of the phase separated block copolymer film on (a) Si with the FFT profile on inset, (b) BK7 glass, and (c) GaN. SEM top-down images of (d) Si nanopillars (e) glass and (f) GaN nanopillars after etch and pattern transfer. Cross section SEM image of (g) Si, and (h) glass nanopillars. (i) Size distribution of the domains (diameter of the cylinders) of the polymer pattern on Si.

The significance of the result shown in (Figure 5.3) is the reduction in reflectivity by a factor of >100 achieved by overcoming the 100 nm size limit in block copolymers, which are typically hindered due to the kinetics at such large chain lengths.

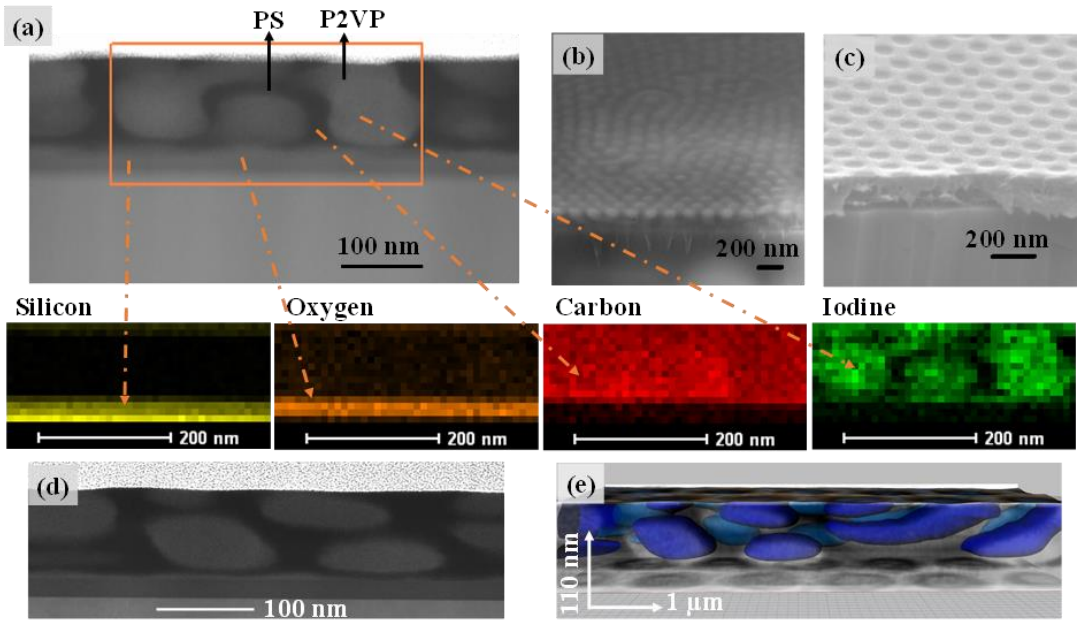


Figure 5.2. Internal structure of the perforated lamellae in 800k g/mol PS-*b*-P2VP. (a) FIB- lamella STEM cross section of the film after annealing and staining with iodine, and the relevant EDX map, (b) after staining the film with iodine, and (c) after staining with RuO4. (d) FIB-STEM image of polymer film after annealing and staining with iodine showing the perforated lamellar and ABC stacking order, (e) visualization of the 3D reconstructed structure based on STEM-LAM cross section and AFM images. For clarity P2VP domains are colored in purple in the front plane and blue at the back plane, while PS domains are transparent.

To date, the SOA antireflective properties of sub-wavelength structures derived from BCPs has an average reflectivity of about 1% at best [19] and often above 1%. In comparison, we achieved a broadband antireflection less than 0.16%, over the entire spectrum of 400-900 nm at AOI of 30° with our 870 nm high SiNPs (Figure 5.3a). The advance in the SOA can be shown by reference to recent work by Rahman *et al* [19], for smaller domain size (sub 50 nm) and shorter nanopillars (made by BCPs), the average value of reflectivity is 20% at higher AOIs [19], while for our samples the average reflectivity remains as low as 1.74% at AOI as high as 75°, across the Vis-

NIR (visible- near infrared) range (Figure 5.3). The marked reduction in visible light reflectivity from the BCP periodically patterned textured Si surface results from scattering in the Vis-NIR range, as Fresnel reflection from step-changes in refractive index are significantly reduced. Fresnel reflection represents the portion of incident light reflected at discrete interfaces between media of different refractive indices, in this case air and silicon. By "blurring" the interface through the use of nanopillars, the reflected light is significantly reduced. It should be mentioned although the formation of giant lamella pattern with L0 ~ 200 nm has been demonstrated [14], they do not provide the graded refractive index and index matching with the ambient air (cause by SiNP tapering) to provide an effective medium, needed for enhanced suppression of light reflectivity.

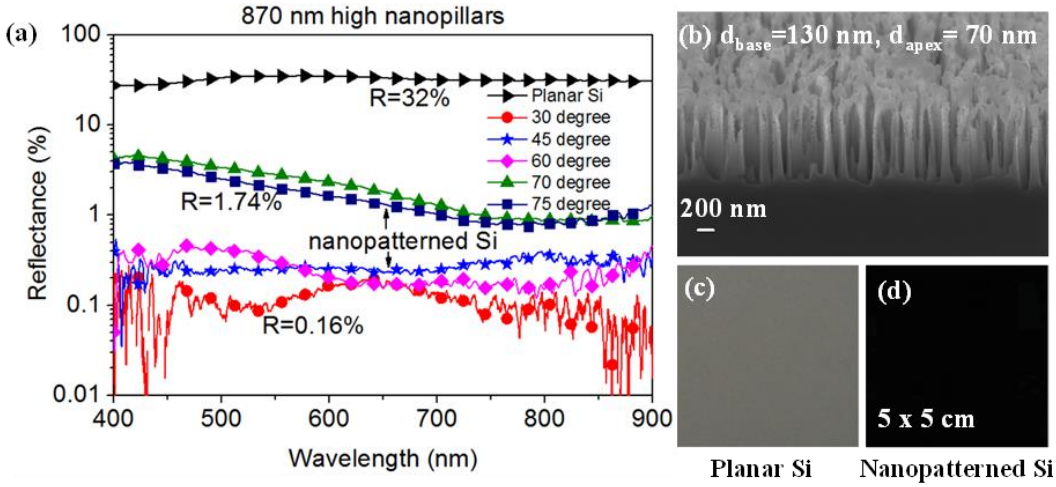


Figure 5.3. Broadband antireflection properties of silicon nanopillars by block copolymer self-assembly 30-75º. (a) reflectivity of planar Si (black triangles) and 870 nm SiNPs for different values of AOI: 30º (red circle), 45º (blue star), 60º (pink diamond), 70º (green triangle), 75º (navy square) , (b) the SEM cross section image of SiNPs with a height of 870 nm, base diameter of 130 nm and apex diameter of 70 nm. (c) Highly reflective planar Si and (d) photographs of nanopatterned Si that appears uniformly black by elimination of visible light reflection compared to Si (100) substrate.

5.4.3 Omnidirectional broadband antireflective SiNPs.

The height and angle dependent optical reflectance of the Si nanopillars was probed in the 400 – 900 nm wavelength for AOIs from near-normal incidence to 75º. Geometric features of the SiNPs are characterised and shown in (Figure 5.4a-f). While the periodicity of the nanopatterns remains the same for all samples, the height of the pillars is varied by BCP processing and etching from 180 to 1150 nm. Tuning the height with high fidelity through the metal oxide inclusion [22] is not achievable through the wet etch process or polymer masks only. The nanopillars' sidewall are consistently in the range 12-15º for the period array. The general trend in reflectivity is maintained for all AOIs (Figure 5.4g-j), and by tuning the height of the nanopillars from 180 to 870 nm, we can supresses the reflectivity more efficiently, as expected due to graded refractive index effect in tall nanopillars with a reducing volume fraction further from the substrate. Increasing the aspect ratio of the SiNPs increase the optical length of the incident light, which can lead to multiple reflection and scattering, which subsequently can leads to more absorption. However, there appears to be a threshold height (~870 nm) above which there is no significant change in reflectivity (compare data for 870 nm nanopillars and 1150 nm nanopillars in Figure 5.4; see also Figure 5.3a). A similar effect has been reported by Teng *et al*. [28], in which increasing the height of the pillars leads to an increase in reflectivity, while the opposite effect is expected. Due to their large surface area, the nanopillars are susceptible to deformation due to surface forces, such as adhesive and capillary force. During the dry etch process, greater capillary force for the high aspect ratio nanopillars, overcomes the supportive force [28], leading SiNPs to bend and aggregate at the top, which acts as a reflective surface.

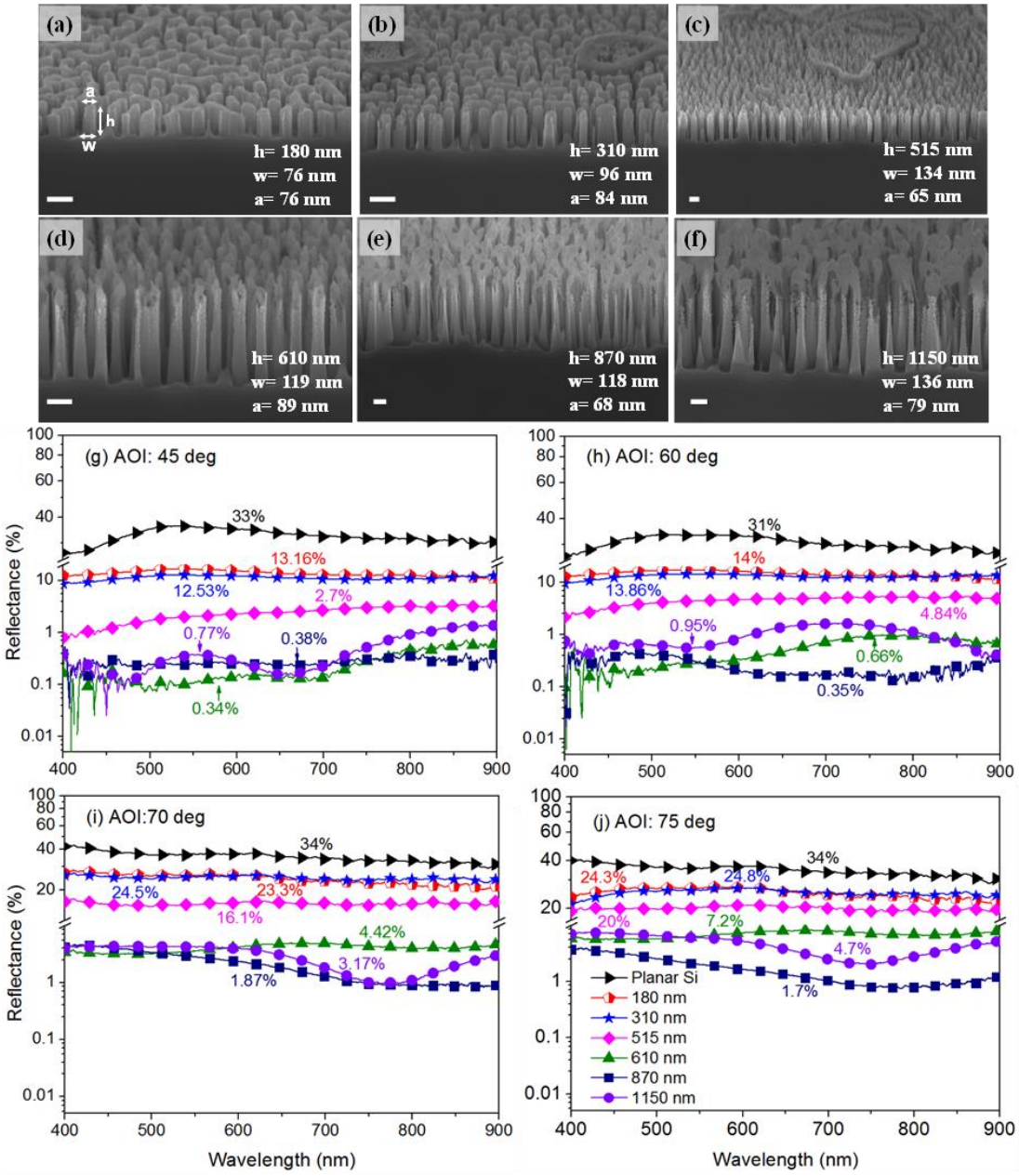


Figure 5.4. Omnidirectional broadband antireflective SiNPs with aspect ratio of 2-15. Geometry configuration of highly tuneable SiNPs made by large BCPs with relevant heights at (a) 180 nm, (b) 310 nm, (c) 515 nm, (d) 610 nm, (e) 870 nm and (f) 1150 nm. The scale bars are 200 nm. Angular dependence of SiNPs with various height at different angle of incidence: (g) 45°, (h) 60°, (i) 70° and (j) 75°. Note that the y-axis is logarithmic scale for the nanopatterned Si data (up to the break point) and linear scale for planar Si. The legend in (g-j) demonstrate average SiNP's height.

The SEM image (Figure 5.4f) confirms the aggregation of SiNPs on top for the tallest SiNP (1150 nm), explaining the reason for lower reflectivity in comparison to 870 nm

SiNPs, which exhibits the strongest reduction in reflectivity (0.16-1.74%) at all angles of incidences (Figure 5.4).The minimum angular dependency demonstrated here could have a significant impact on photovoltaics efficiency as it would reduce the need for an integrated mechanised tracking system that keeps the solar cells aligned to the sun throughout the day. Angle-resolved reflectance data in (Figure 5.5) demonstrate that BCP-nanopatterned silicon surfaces are very effective in reducing silicon transparency at IR wavelengths, in particular for common data transmission wavelengths of 1310 and 1550 nm (Figure 5a and 5b) from Si/SiGe-based MQW LEDs [29] or InGaAs/GaAs lasers [30]. The patterned tapered SiNP structures with a periodicity of ~ 180 nm (~$\lambda/2n$), comprising a graded index effective medium with a height $h \sim \lambda/2$ (i.e. 610 nm pillars at λ= 1310 nm), reduces NIR reflectivity down to 7.5-15% from 44% in non-patterned Si within the AOI range of 30-75° (Figure 5a) consistent with a very effective subwavelength broadband omnidirectional antireflection coating. In the visible range, at the He-Ne emission energy at λ = 632.8 nm (Figure 5.5d), resonant scattering is considerably enhanced for 610 nm, with maximum antireflection (down to a value as low as 0.15 - 8%) up to 75° away from normal incidence. In the visible range (at 514.5 nm and 632. 8 nm) NPs with heights from 870 - 1150 nm exhibit the best broadband omnidirectional antireflection properties, and in both cases exhibit aspect ratios from 10-15. The minimum reflectivity of 0.16-1.74% at λ = 632.8 nm is achieved for 870 nm high SiNPs (aspect ratio > 10). In the NIR range, shorter NPs (lower aspect ratio, for similar periodicity and diameters, are effect antireflection coatings when $h \sim \lambda/2$.

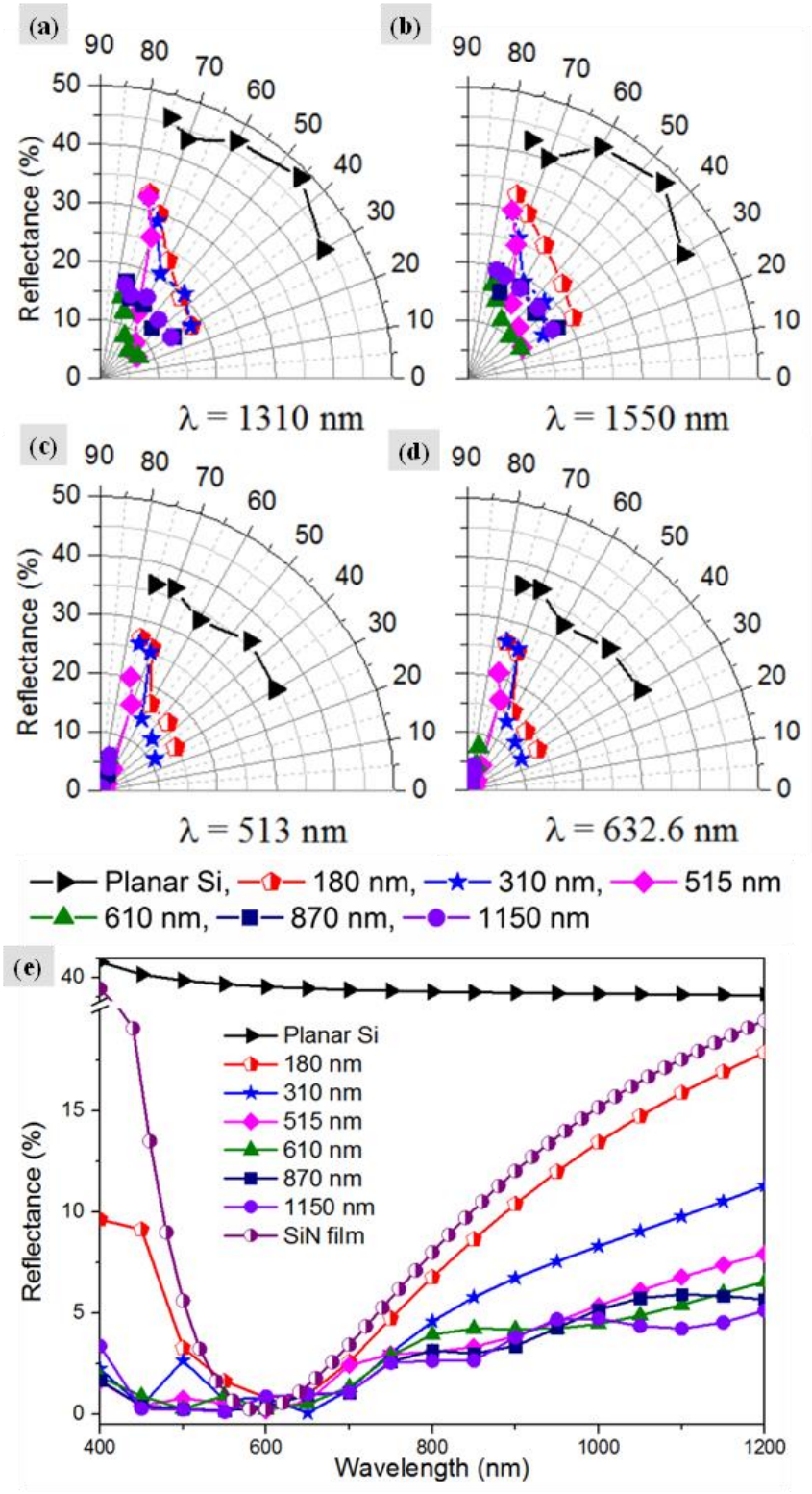


Figure 5.5. Angular reflectivity plot (0-90°) of SiNPs with different heights. At (a) λ = 1310 nm, (b) λ = 1550, (c) λ = 513 nm and (d) λ = 632.6 nm. The legends and colours demonstrate SiNP's height. (e) Simulated reflectance spectra of unpolarised light from nanopillars with different pillar heights compared to planar Si and SiN coated (75-nm layer) silicon.

5.4.4 Simulation.

We have simulated the normal reflectance of unpolarised light from the SiNP layers across the solar emission spectrum (400 to 1200 nm) using GD-Calc, which computes diffraction efficiencies of optical grating structures, including bi-periodic gratings. For more information see the section 5.3.7 and Figure S5.7.7. These results are compared with the Fresnel reflectance from uncoated silicon and SiN-coated silicon in Figure 5.5e. Applying simulated reflectance results to the AM1 (overhead midday) solar spectrum and standard model for photon absorption in monocrystalline silicon (fill factor = 0.55, i.e. the fraction of the grating period which contains the grating material; in this case the ratio of the nanopillar diameter compared to its period), the predicted conversion efficiency of a PV panel would increase from 17.33% for untreated silicon, to 22.09% for 870 nm SiNPs. Reflectance values for an AR coating (75 nm SiN film) are also calculated and imply an efficiency of 21.08%. Hence, the SiNPs presented in this paper would improve the electrical output of a silicon PV system by 1.01% (absolute) or 4.79% (relative) compared to an AR-coated device. As noted previously, however, measured reflectance values are considerably lower than simulated results. The most likely cause of this anomaly is the presence of a thin silicon oxide layer coating over the silicon nanopillars. Formed during the plasma etch process, this layer reduces reflections at the high-RI silicon interface. Assuming a uniform thickness along the length of the nanopillar, the SiO_2 layer will have a greater influence on the localised refractive index at the top of the pillar than at the bottom. The net effect is an additional gradation in the refractive index experienced by light diffracting through the structure and thereby a reduced reflectivity. Applying measured reflectance values to the PV model suggests a PV efficiency of 24.6% - representing a 3.52% (absolute) or 16.7% (relative) increase in electrical energy compared to the AR-coated device.

5.5 Conclusions

In conclusion, the BCP patterning capabilities described here make exceptional coatings for improved transparency, light focusing, antireflection and for tuning photon absorption for a variety of applications on a wide range of surfaces, materials and non-planar substrates. BCP patterning that avoid previous 'inherent' size limitations, that facilitate a high density ordered array of nanopillars with tuneable height, are easily scalable and can be formed at low temperature. Compared to nanocones and other 'black' silicon layers, broadband antireflection coatings may now be possible for flexible PVs, solar cell technologies, and for broadband elimination of reflection of high quality glass optics.

5.6 References

[1] A. M. Urbas, M. Maldovan, P. DeRege, and E. L. Thomas, "Bicontinuous Cubic Block Copolymer Photonic Crystals," *Adv. Mater.*, vol. 14, no. 24, pp. 1850–1853, Dec. 2002.

[2] B. R. Sveinbjornsson, R. a Weitekamp, G. M. Miyake, Y. Xia, H. a Atwater, and R. H. Grubbs, "Rapid self-assembly of brush block copolymers to photonic crystals," *Proc. Natl. Acad. Sci.*, vol. 109, no. 36, pp. 14332–14336, Sep. 2012.

[3] T. Deng, C. Chen, C. Honeker, and E. L. Thomas, "Two-dimensional block copolymer photonic crystals," *Polymer (Guildf).*, vol. 44, no. 21, pp. 6549–6553, Oct. 2003.

[4] D. A. Hajduk, P. E. Harper, S. M. Gruner, C. C. Honeker, G. Kim, E. L. Thomas, and L. J. Fetters, "The Gyroid: A New Equilibrium Morphology in Weakly Segregated Diblock Copolymers," *Macromolecules*, vol. 27, no. 15, pp. 4063–4075, Jul. 1994.

[5] S. Valkama, H. Kosonen, J. Ruokolainen, T. Haatainen, M. Torkkeli, R. Serimaa, G. ten Brinke, and O. Ikkala, "Self-assembled polymeric solid films with temperature-induced large and reversible photonic-bandgap switching," *Nat. Mater.*, vol. 3, no. 12, pp. 872–876, Dec. 2004.

[6] Y.-W. Chiang, C.-Y. Chou, C.-S. Wu, E.-L. Lin, J. Yoon, and E. L. Thomas, "Large-Area Block Copolymer Photonic Gel Films with Solvent-Evaporation-Induced Red- and Blue-Shift Reflective Bands," *Macromolecules*, vol. 48, no. 12, pp. 4004–4011, Jun. 2015.

[7] T. Lohmüller, M. Helgert, M. Sundermann, R. Brunner, and J. P. Spatz, "Biomimetic Interfaces for High-Performance Optics in the Deep-UV Light Range," *Nano Lett.*, vol. 8, no. 5, pp. 1429–1433, May 2008.

[8] A. Fujimoto and K. Asakawa, "Nano-structured Surface Fabrication for Higher Luminescent LED by Self-assembled Block Copolymer Lithography," *J. Photopolym. Sci. Technol.*, vol. 20, no. 4, pp. 499–503, 2007.

[9] X. Zhang, A. B. Sushkov, C. J. Metting, S. Fackler, H. D. Drew, and R. M. Briber, "Silicon Patterning Using Self-assembled PS- b -PAA Diblock Copolymer Masks for Black Silicon Fabrication via Plasma Etching," *Plasma Process. Polym.*, vol. 9, no. 10, pp. 968–974, Oct. 2012.

[10] S. Guldin, P. Kohn, M. Stefik, J. Song, G. Divitini, F. Ecarla, C. Ducati, U. Wiesner, and U. Steiner, "Self-Cleaning Antireflective Optical Coatings," *Nano Lett.*, vol. 13, no. 11, pp. 5329–5335, Nov. 2013.

[11] K. Hur, Y. Francescato, V. Giannini, S. A. Maier, R. G. Hennig, and U. Wiesner, "Three-Dimensionally Isotropic Negative Refractive Index Materials from Block Copolymer Self-Assembled Chiral Gyroid Networks," *Angew. Chemie Int. Ed.*, vol. 50, no. 50, pp. 11985–11989, Dec. 2011.

[12] S. Vignolini, N. A. Yufa, P. S. Cunha, S. Guldin, I. Rushkin, M. Stefik, K. Hur, U. Wiesner, J. J. Baumberg, and U. Steiner, "A 3D Optical Metamaterial Made by Self-Assembly," *Adv. Mater.*, vol. 24, no. 10, p. OP23-OP27, Mar. 2012.

[13] M. Stefik, S. Guldin, S. Vignolini, U. Wiesner, and U. Steiner, "Block copolymer self-assembly for nanophotonics," *Chem. Soc. Rev.*, vol. 44, no. 15, pp. 5076–5091, 2015.

[14] E. Kim, H. Ahn, S. Park, H. Lee, M. Lee, S. Lee, T. Kim, E.-A. Kwak, J. H. Lee, X. Lei, J. Huh, J. Bang, B. Lee, and D. Y. Ryu, "Directed Assembly of High Molecular Weight Block Copolymers: Highly Ordered Line Patterns of Perpendicularly Oriented Lamellae with Large Periods," *ACS Nano*, vol. 7, no. 3, pp. 1952–1960, Mar. 2013.

[15] J. K. D. Mapas, T. Thomay, A. N. Cartwright, J. Ilavsky, and J. Rzayev, "Ultrahigh Molecular Weight Linear Block Copolymers: Rapid Access by Reversible-Deactivation Radical Polymerization and Self-Assembly into Large Domain Nanostructures," *Macromolecules*, vol. 49, no. 10, pp. 3733–3738, May 2016.

[16] M. B. Runge and N. B. Bowden, "Synthesis of High Molecular Weight Comb Block Copolymers and Their Assembly into Ordered Morphologies in the Solid State," *J. Am. Chem. Soc.*, vol. 129, no. 34, pp. 10551–10560, Aug. 2007.

[17] A. Urbas, R. Sharp, Y. Fink, E. L. Thomas, M. Xenidou, and L. J. Fetters, "Tunable Block Copolymer/Homopolymer Photonic Crystals," *Adv. Mater.*, vol. 12, no. 11, pp.

812–814, Jun. 2000.

[18] A. Noro, Y. Tomita, Y. Shinohara, Y. Sageshima, J. J. Walish, Y. Matsushita, and E. L. Thomas, "Photonic Block Copolymer Films Swollen with an Ionic Liquid," *Macromolecules*, vol. 47, no. 12, pp. 4103–4109, Jun. 2014.

[19] A. Rahman, A. Ashraf, H. Xin, X. Tong, P. Sutter, M. D. Eisaman, and C. T. Black, "Sub-50-nm self-assembled nanotextures for enhanced broadband antireflection in silicon solar cells," *Nat. Commun.*, vol. 6, p. 5963, Jan. 2015.

[20] B. Päivänranta, P. K. Sahoo, E. Tocce, V. Auzelyte, Y. Ekinci, H. H. Solak, C. Liu, K. O. Stuen, P. F. Nealey, and C. David, "Nanofabrication of Broad-Band Antireflective Surfaces Using Self-Assembly of Block Copolymers," *ACS Nano*, vol. 5, no. 3, pp. 1860–1864, Mar. 2011.

[21] H. K. Raut, V. A. Ganesh, A. S. Nair, and S. Ramakrishna, "Anti-reflective coatings: A critical, in-depth review," *Energy Environ. Sci.*, vol. 4, no. 10, p. 3779, 2011.

[22] T. Ghoshal, T. Maity, J. F. Godsell, S. Roy, and M. A. Morris, "Large scale monodisperse hexagonal arrays of superparamagnetic iron oxides nanodots: A facile block copolymer inclusion method," *Adv. Mater.*, vol. 24, no. 18, pp. 2390–2397, 2012.

[23] J. Yoon, R. T. Mathers, G. W. Coates, and E. L. Thomas, "Optically Transparent and High Molecular Weight Polyolefin Block Copolymers toward Self-Assembled Photonic Band Gap Materials," *Macromolecules*, vol. 39, no. 5, pp. 1913–1919, Mar. 2006.

[24] C. W. Pester, K. Schmidt, M. Ruppel, H. G. Schoberth, and A. Böker, "Electric-Field-Induced Order–Order Transition from Hexagonally Perforated Lamellae to Lamellae," *Macromolecules*, vol. 48, no. 17, pp. 6206–6213, Sep. 2015.

[25] P. Mokarian-Tabari, C. Cummins, S. Rasappa, C. Simao, C. M. Sotomayor Torres, J. D. Holmes, and M. A. Morris, "Study of the Kinetics and Mechanism of Rapid Self-Assembly in Block Copolymer Thin Films during Solvo-Microwave Annealing," *Langmuir*, vol. 30, no. 35, pp. 10728–10739, Sep. 2014.

[26] A. Baruth, M. Seo, C. H. Lin, K. Walster, A. Shankar, M. A. Hillmyer, and C. Leighton, "Optimization of Long-Range Order in Solvent Vapor Annealed Poly(styrene)- block -poly(lactide) Thin Films for Nanolithography," *ACS Appl. Mater. Interfaces*, vol. 6, no. 16, pp. 13770–13781, Aug. 2014.

[27] R. Lundy, S. P. Flynn, C. Cummins, S. M. Kelleher, M. N. Collins, E. Dalton, S. Daniels, M. A. Morris, and R. Enright, "Controlled solvent vapor annealing of a high χ block copolymer thin film," *Phys. Chem. Chem. Phys.*, vol. 19, no. 4, pp. 2805–2815, 2017.

[28] F. Teng, N. Li, L. Liu, D. Xu, D. Xiao, and N. Lu, "Fabrication of ordered Si

nanopillar arrays for ultralow reflectivity," *RSC Adv.*, vol. 6, no. 19, pp. 15803–15807, 2016.

[29] C. O'Dwyer, M. Szachowicz, G. Visimberga, V. Lavayen, S. B. Newcomb, and C. M. S. Torres, "Bottom-up growth of fully transparent contact layers of indium tin oxide nanowires for light-emitting devices," *Nat. Nanotechnol.*, vol. 4, no. 4, pp. 239–244, Apr. 2009.

[30] D. Bimberg, N. Kirstaedter, N. N. Ledentsov, Z. I. Alferov, P. S. Kop'ev, and V. M. Ustinov, "InGaAs-GaAs quantum-dot lasers," *IEEE J. Sel. Top. Quantum Electron.*, vol. 3, no. 2, pp. 196–205, Apr. 1997.

5.7 Appendix – Chapter 5

The diameter of the features being subwavelength strongly affect reflectivity (close to quarter wavelength, but not prescriptively so). The smaller features do not supress the reflectivity as much as the larger features do. See Figure S5.7.1.

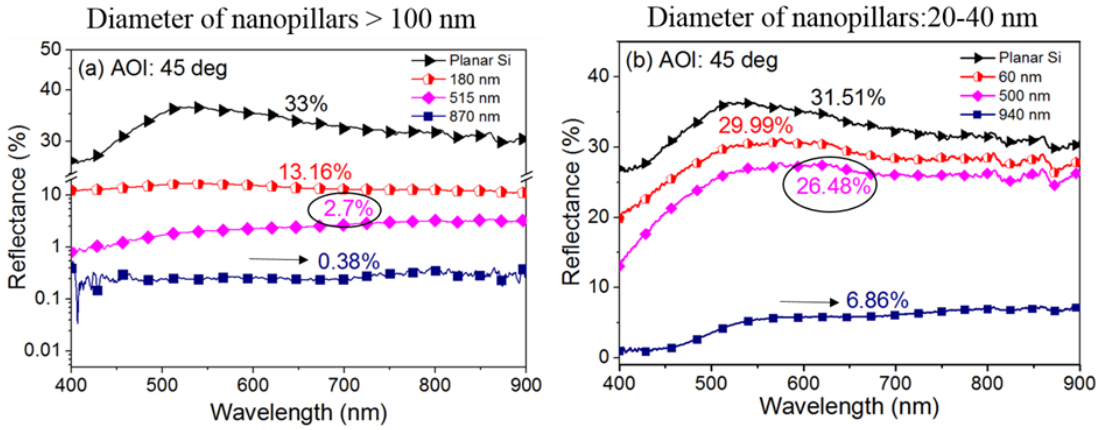


Figure S5.7.1. Comparing the reflectivity of (a) small nanopillars (diameter of 20-40 nm) with (b) large nanopillars (d>100 nm). Colours are indicative of nanopillars height. The large dimensions nanopillars clearly supress light reflection much more effectively. The colours are indicative of nanopillar height.

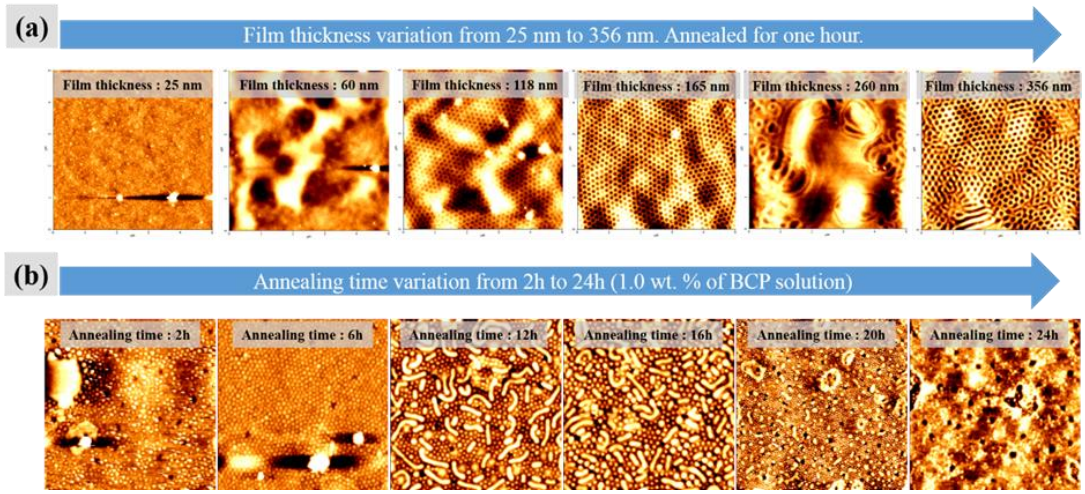


Figure S5.7.2. Film thickness and solvent annealing time variation. AFM topographic images of BCP films after solvent annealing. (a) Phase separation after an hour solvent annealing of films with a different thicknesses (b) annealing time from 2 h to 24 h for 1 wt. % BCP solution.

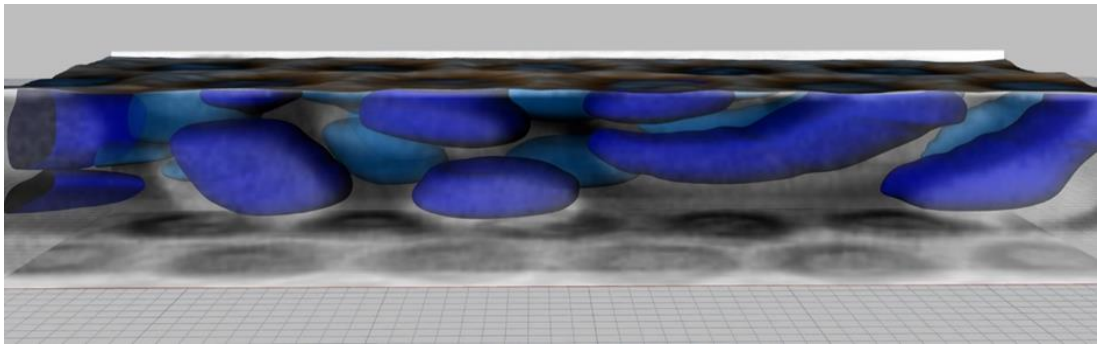


Figure S5.7.3. Visualization of the 3D modelled structure based on STEM-LAM cross section and AFM images. 3D modelled structure is constructed using the profile from STEM images and AFM images. The domains are colourised to show the layers of material. Link for the 3D video of the modelled structure: https://www.youtube.com/watch?v=sztZ9XYzU1U

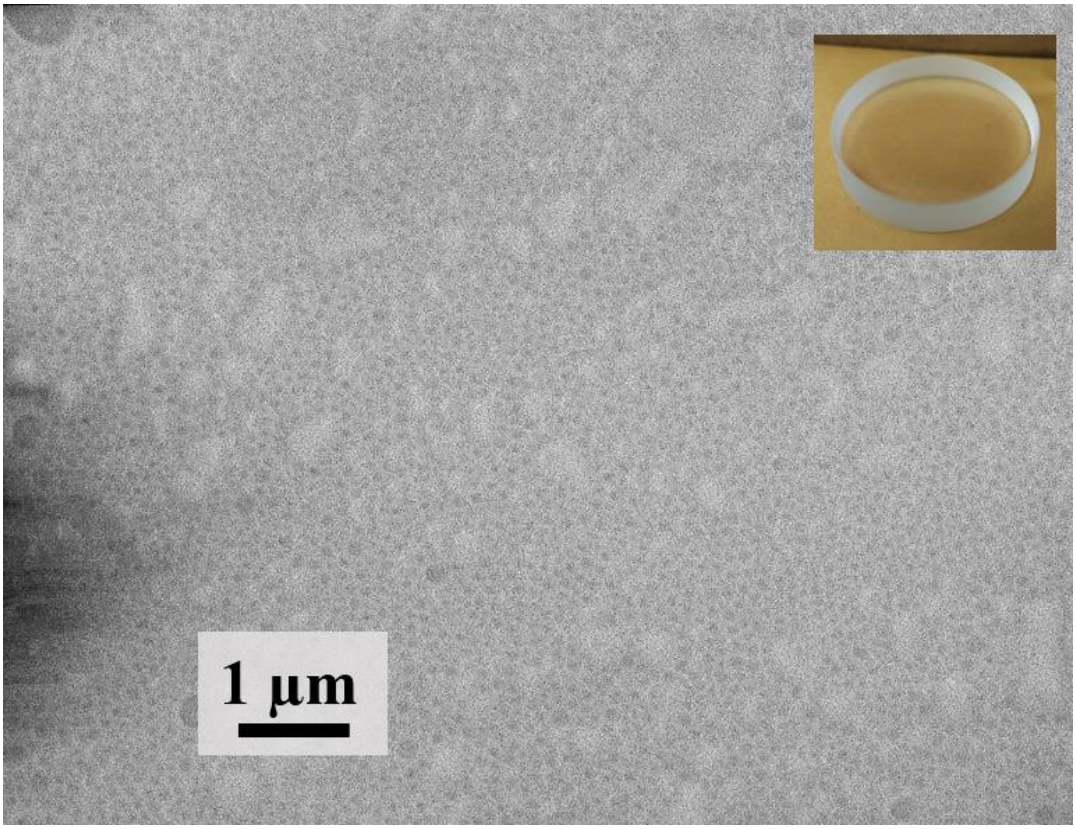


Figure S5.7.4. Patterned BK7 convex lens. SEM image of PS-*b*-P2VP after phase separation on BK7 convex lens. 2.0 wt. % of PS-*b*-P2VP polymer solution was spin coated on convex lens and exposed to mixed solvent of THF:$CHCl_3$ with volume ratio of 2:1, for an hour at room temperature. Phase separated BCP thin film were stained in iodine for 6 hours to enhance the contrast difference between PS and P2VP block and image them in SEM. The inset is the optical micrograph of the lens.

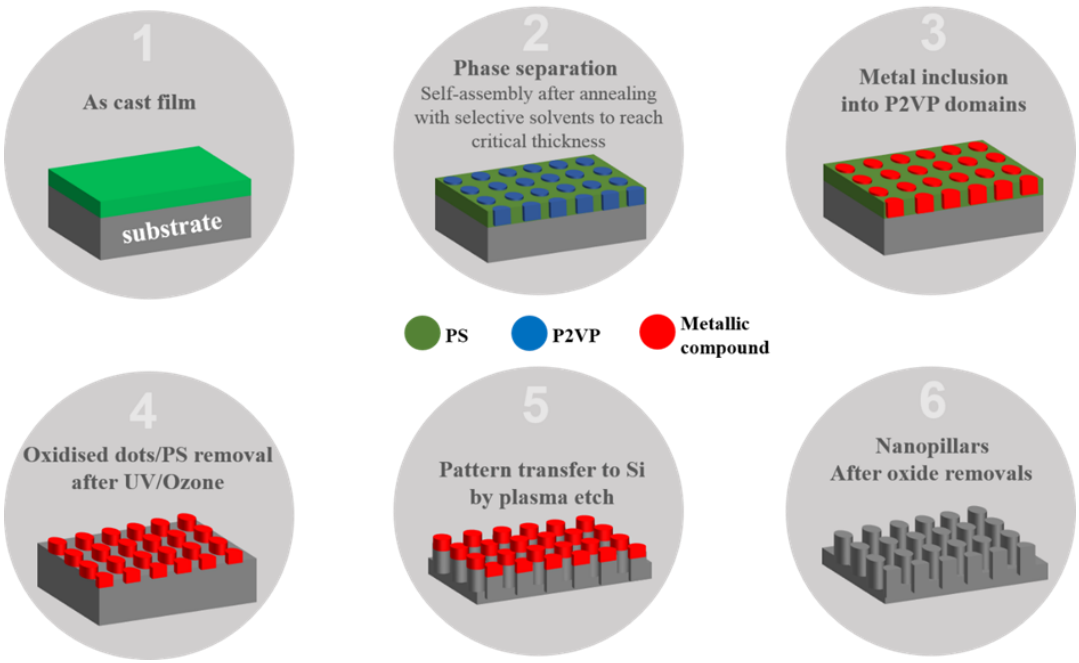


Figure S5.7.5. Schematic representation of fabrication of nanopatterned Si.

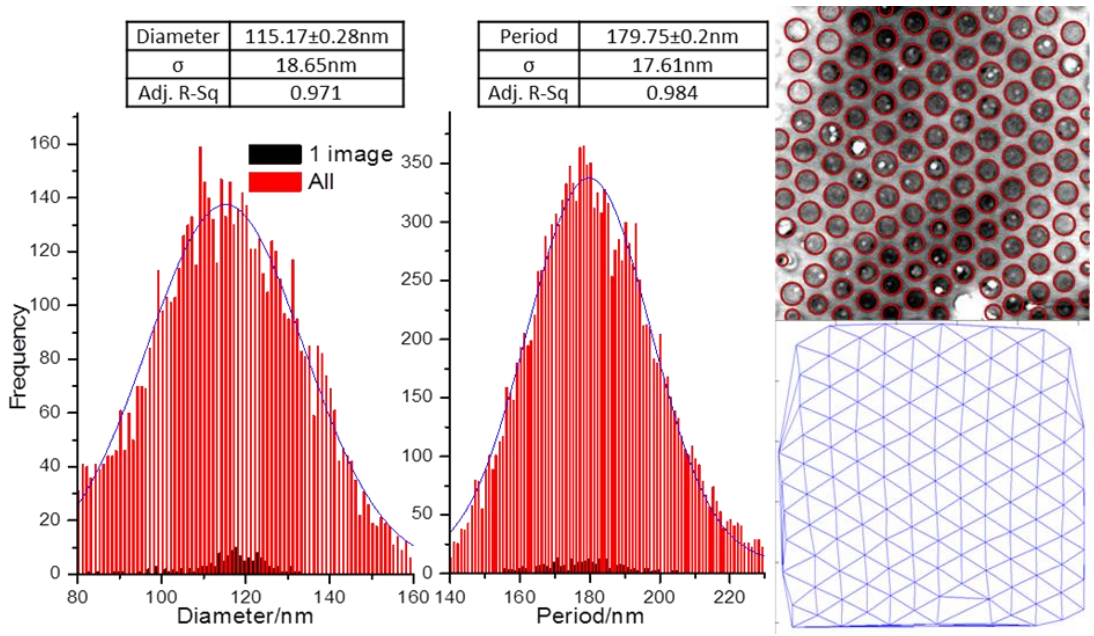


Figure S5.7.6. Size distribution for cylinder diameter (CD) (left) and period (L0) (right) of the BCP films made on Si. Data was collected from 17 images of 10 individual samples. An example of the output detected features and Delaunay triangulation are also shown.

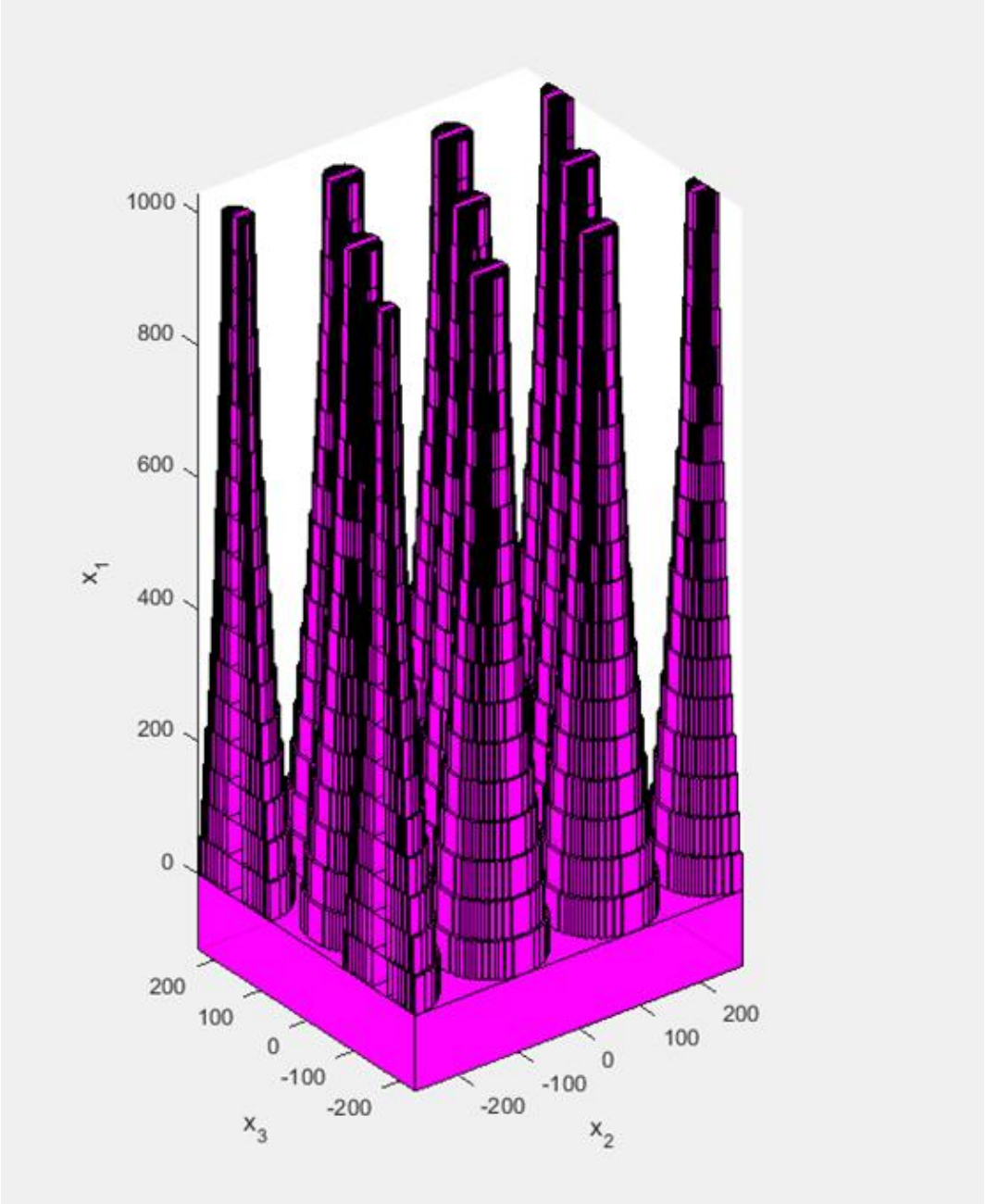


Figure S5.7.7. The simulated SiNPs

Chapter 6

Conclusions and Future Work

6.1 Conclusions and Future Work

Block copolymers have a wide range of potential applications in nanoscale fabrication due to their tuneable feature size, well-ordered patterns and scalability. Of particular interest is their use in the production of the next-generation of electronic devices. In order to continue producing more efficient devices with higher densities, new lithographic tools must be developed and leading the integration of "bottom-up" processes is the directed self-assembly of block copolymers. The advantages of BCPs are clear; low-cost, high-density and the ability to achieve sub-10 nm features. However, there are still roadblocks to BCP integration in the manufacturing process, namely process conditions, and defect densities. In this thesis, we respond to these challenges with the introduction of a brushless lamellar PS-*b*-PEO and the development of software for pattern analysis.

In chapter 2, the dynamics of solvent diffusion with BCP thin film during solvent annealing was explored, with it indicating the presence of solvent fronts propagating through the film. The cyclical flipping nature of cylindrical PS-*b*-PEO was also noted. Combined, this system may prove useful as a tuneable system, able to function on dot and line patterns in the fabrication of nanoelectronics without necessitating separate processes. It was also noted that within graphoepitaxial patterns, the self-assembly occurred at an accelerated rate, achieving a better order in reduced time.

Chapter 3 introduced the first reported creation of perpendicular orientated lamellar PS-*b*-PEO, without the need for additional surface pre-treatments. Pattern transfer of this system, such as PEO-*b*-PI, was also demonstrated. Through consideration of the annealing conditions, it was possible to create preferential orientation. It is proposed

that this method could be used with other BCP systems, reducing the processing time required for pattern formation.

The change from hexagonal PS-*b*-PEO in Chapter 2 to the symmetrical systems used in Chapter 3 allowed for the creation of more robust etch masks for nanowire fabrication. While microphase separation and ordering in the hexagonal BCP was more readily achieved, the internal structure of the film, that being PEO cylinders submerged in a PS matrix, would require a more complex etching process. An initial PS selective etch would be required to expose the PEO cylinders, followed by a PEO selective etch, before pattern transfer into the substrate. The lamellar system allows for a single PEO selective etch prior to pattern transfer. Additionally, the structure of the cylinders would not have been ideal for pattern transfer as it would have resulted in a "rounding" of the top of the nanowire as more of the cylinder was removed. The hexagonal system is ideal for use as a template for inorganic nanowire and nanodots applications, as well as for fabrication of vertical interconnects between strata of microchips. The use of two symmetrical PS-*b*-PEO systems demonstrated the scalability of the system, going from CD of 24 nm to 17 nm, showing promise as a system that can achieve the sub-10 nm features required for the next generation of microelectronics.

Chapter 4 detailed the application developed for analysis of BCP patterns. It was shown that it was capable of deriving important details within BCP patterns that may have been overlooked through visual inspection. Whilst similar programs exist within high end pilot line processes [1], [2], it is hoped that a possible future release of this system will facilitate improved optimisation of novel BCP systems within research groups, yielding better patterns and clearing the way for integration into industrial

applications. It may become a critical tool as the specifications for roughness and position tolerances steadily decrease with feature size [3], as there is presently no centrally defined series of metrics, but rather multiple in-house methods with little-to-no discussion available in the literature. This has been a major impedance in the advancement of BCPs.

Chapter 5 demonstrated the types of functional surface the BCPs are capable of creating. Through the use of PS-*b*-P2VP as a template, silicon nanopillars were created over large areas of substrates, demonstrating BCPs properties of high coverage and density, allowing a highly anti-reflective surface to be created for optical applications. Further expansion of BCPs nanoscale fabrication ability outside of the nanoelectronics will allow the system to achieve its full potential as a low-cost tool for nanotechnology [4], [5].

Whilst this thesis has dealt with the creation of sub-20 nm features through more established BCP systems, many challenges must yet be overcome as new high-χ system are synthesised and introduced [6], [7]. Additionally, new metrology techniques will need to be developed to inspect systems once they have fully entered the sub-10 nm range, as current microscopy techniques will not have sufficient resolution to characterise systems at this scale [8], [9].

6.2 References

[1] S. Levi, Y. Weinberg, O. Adan, M. Klinov, M. Argoud, G. Claveau, and R. Tiron, "Free surface BCP self-assembly process characterization with CDSEM," vol. 9778, p. 977815, 2016.

[2] G. Claveau, P. Quemere, M. Argoud, J. Hazart, P. P. Barros, A. Sarrazin, N. Posseme, R. Tiron, X. Chevalier, C. Nicolet, and C. Navarro, "Surface affinity role in graphoepitaxy of lamellar block copolymers," *J. Micro/Nanolithography, MEMS, MOEMS*, vol. 15, no. 3, p. 31604, Aug. 2016.

[3] H. Pathangi, V. Vaid, B. T. Chan, N. Vandenbroeck, J. Li, S. E. Hong, Y. Cao, B. Durairaj, G. Lin, M. Somervell, T. Kitano, R. Harukawa, K. Sah, A. Cross,

H. Bayana, L. D'Urzo, and R. Gronheid, "DSA materials contributions to the defectivity performance of 14nm half-pitch LiNe flow at IMEC," in *Proc. of SPIE*, 2016, vol. 9777, no. Figure 1, p. 97770G.

[4] G. W. Lee, S. Lee, J. H. Kim, S.-G. Yim, J. Ryu, E. Lee, J. Lee, S. Il Yoo, and S. Y. Yang, "Density-Controlled Freestanding Biodegradable Nanopillar Arrays Patterned via Block Copolymer Micelle Lithography," *Macromol. Mater. Eng.*, vol. 1600361, pp. 1–8, 2016.

[5] Y. Mai and A. Eisenberg, "Self-assembly of block copolymers," *Chem. Soc. Rev.*, vol. 41, no. 18, p. 5969, 2012.

[6] C. Sinturel, F. S. Bates, and M. A. Hillmyer, "High χ–Low N Block Polymers: How Far Can We Go?," *ACS Macro Lett.*, vol. 4, no. 9, pp. 1044–1050, 2015.

[7] T. Ghoshal, C. Ntaras, M. T. Shaw, J. D. Holmes, A. Avgeropoulos, and M. A. Morris, "A vertical lamellae arrangement of sub-16 nm pitch (domain spacing) in a microphase separated PS-b-PEO thin film by salt addition," *J. Mater. Chem. C*, vol. 3, no. 27, pp. 7216–7227, 2015.

[8] A. P. Bell, R. Senthamaraikannan, T. Ghoshal, A. Chaudhari, M. Leeson, and M. A. Morris, "The development and advantages of helium ion microscopy for the study of block copolymer nanopatterns," in *Proc. of SPIE*, 2015, vol. 9424, p. 94241R.

[9] M. Fouchier, E. Pargon, and B. Bardet, "A new method based on AFM for the study of photoresist sidewall smoothening and LER transfer during gate patterning," in *Proc. of SPIE*, 2013, vol. 8685, p. 86850B.